



Universidad de Navarra

Facultad de Ciencias

Colloidal crystal formation through interfacial mechanisms

Maximiliano Andrés Giuliani

Servicio de Publicaciones de la Universidad de Navarra

ISBN 84-8081-088-2



Universidad de Navarra
School of Science

Colloidal crystal formation through interfacial mechanisms

Submitted by **Maximiliano Andrés Giuliani** in partial fulfillment of the requirements
for the Doctoral Degree of the University of Navarra

This dissertation has been written under my supervision at the Department of Physics
and Applied Mathematics, and I approve its submission to the Defense Committee.

Signed on September 24, 2010

Dr. Wenceslao González-Viñas

Declaración:

Por la presente yo, **D. Maximiliano Andrés Giuliani**, declaro que esta tesis es fruto de mi propio trabajo y que en mi conocimiento, no contiene ni material previamente publicado o escrito por otra persona, ni material que sustancialmente haya formado parte de los requerimientos para obtener cualquier otro título en cualquier centro de educación superior, excepto en los lugares del texto en los que se ha hecho referencia explícita a la fuente de la información.

(I hereby declare that this submission is my own work and that, to the best of my knowledge and belief, it contains no material previously published or written by another person nor material which to a substantial extent has been accepted for the award of any other degree of the university or other institute of higher learning, except where due acknowledgment has been made in the text.)

De igual manera, autorizo al Departamento de Física y Matemática Aplicada de la Universidad de Navarra, la distribución de esta tesis y, si procede, de la "fe de erratas" correspondiente por cualquier medio, sin perjuicio de los derechos de propiedad intelectual que me corresponden.

Signed on September 24, 2010

Maximiliano Andrés Giuliani

© Maximiliano Andrés Giuliani

Derechos de edición, divulgación y publicación:

© Departamento de Física y Matemática Aplicada, Universidad de Navarra

To my family that has
always been present
despite the distance.

Acknowledgements

In this lines, I would like to acknowledge to the many people and institutions involved in this project, their collaboration and friendship played a fundamental role in my growth at a professional and personal level. I would like to thank my family that, despite the distance, have been the main support that allowed me to arrive at this point.

In first place, I would like to thank to my advisor Dr. Wenceslao González-Viñas for his patience and support along this period. His efforts on challenging me allowed me to improve my capabilities and overcome the difficulties that arose along this study. Also, my thanks to the group of professors of the Department of Physics and Applied Mathematics, that made the teaching at the university a pleasant task. I'm specially grateful to the my fellow PhD. students who made of my stay in Pamplona a second home: Ana Šimić, Cristian Mancok, Alberto de la Torre Monguió, Álvaro Janda, Monserrat Miranda Galcerán, Roberto Arévalo, María Yoldi, Cristina Arcos, Moorthi Pichumani, Manuel Acevedo, Iván Efrain Martínez, Gerard Vidal, José De la Cruz, Tomás González, José Guadarrama, Miguel López. Also, I thank to Rafael Sirera Bejarano from the Department of Chemistry and Soil Science for his collaboration, particularly at the beginning of my research.

During my stage in Canada, I had the opportunity of meet an amazing group of people for whom I have a special appreciation: Dr. Kristin Poduska, Dr. Erika Merschrod, Dr. Marek Bomberek, Hugh Newman, Suliman Barhoum, Ahmad Almudallal, Andrew Bartlett, Amit Agarwal, Corey Kelly, Alanna Wicks, Ania Polomska, Louise Dawe, Mark McDonald and Jason Mercer, I thank to them and, specially, to Anand Yethiraj for an amazing stay in Memorial University, and the opportunity to know a truly unique recommendable portion of the world: Newfoundland is one of the most beautiful places that I had the pleasure to seen.

I have a special esteem for Dr. Martín Pastor and Dr. Ángel Garcimartín Montero, who showed the beauties of a Navarra and the surroundings from the point of view of a mountain bike.

Finally, to the University of Navarra and the Asociación de Amigos for the scholarship that allow me to carry out this work; and to the Departamento de Educación (Gobierno de Navarra) and to the Spanish Government (FIS2007-66004-C02-01 and FIS2008-01126) for partial funding support.

"Quisiera dejar el pequeño
lugar en que vivo más limpio,
más sano, más bello,
más justo y más libre"

René Favaloro, (1923-2000)

Contents

Preface	xiii
I Vertical deposition of water based colloidal suspensions	1
1. Introduction	3
1.1. Colloidal suspensions	4
1.1.1. Dispersive media	5
1.1.2. Electrical double layer	5
1.2. Transport phenomena	8
1.2.1. Electrokinetic phenomena	9
1.2.2. Other phenomena	12
1.3. Models of evaporation induced self-assembly	17
2. Experimental Setup	21
2.1. Measurements of velocities	28
2.2. Evolution of velocities	32
2.3. Scaling factors	33
3. Results	35
3.1. Deposited structures	35
3.2. Characteristic velocities	40
3.3. Evolution of the velocity of the contact line	41
3.4. Bulk flows	42
4. Discussion	45
II Spin-coating of rapidly dried colloidal suspensions	57
5. Introduction	59
5.1. Emslie model for spin-coating of a viscous fluid	60
5.2. Colloidal suspensions under shearing	64

6. Experimental Setup	67
6.1. Characterisation of the dynamics	68
6.2. Characterisation of the dried structures	71
7. Results	75
7.1. Thickness of the dried polycrystalline structures	75
7.2. Dynamics of thinning	76
7.3. Dynamics of long range orientational order	78
7.4. Dynamics of the drying front	80
7.5. Arms definition in the dried substrate	81
8. Discussion	83
8.1. Model for spin-coating of evaporative fluids	83
8.2. Evaporation rate during final drying	86
8.3. Order in the fluid phase	87
8.4. Order in the dried structure	89
Conclusions and Outlook	95
Bibliography	99
Summary	107
Resumen	108

Preface

Nature is riddled with examples of colourful surfaces, from butterflies to rocks, including fossils (see Figure 1 (a) - (f)). The origin of these visually attractive colours is common to all these cases: the surfaces show a sub-micrometre periodic structure that give constructive interference around particular wavelengths in the visible spectrum. With time, it was possible to reproduce this natural phenomena using sub-micrometre spheres. The structures obtained were named artificial opals in contrast to natural opals that inspire them (see Figure 1 (d) and (g)).

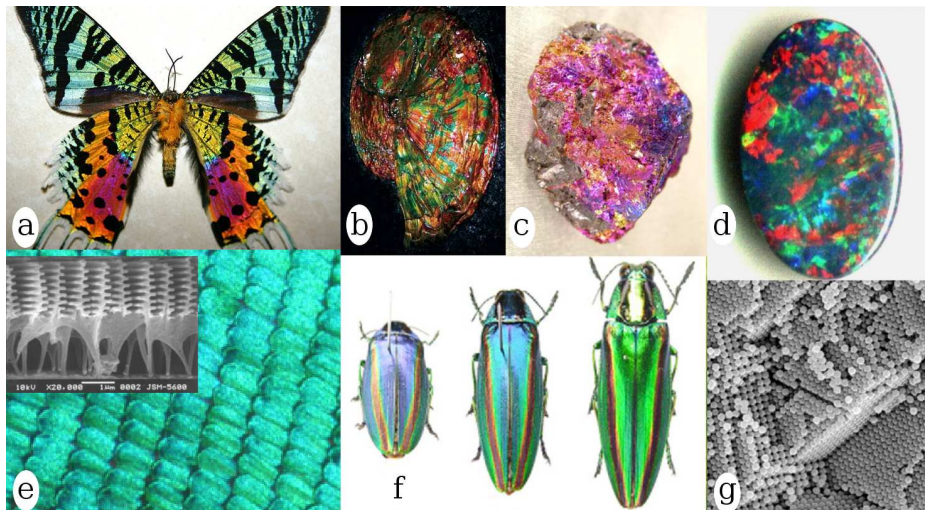


Figure 1: Some examples of colourful surfaces emerging from complex periodicity at nanometre scale. (a) colourful butterfly wings; (b) petrified ammonite (ammolite - nacreous layer of the aragonite fossil shells); (c) peacock ore (bomite - copper iron sulfide); (d) natural opal; (e) macroscopic image of the blue morpho butterfly wing (*Morpho menelaus*), inset: SEM image of the sub-micrometre structure; (f) variety of jewel beetles; (g) artificial opal. Images (a) to (d) taken from multiple sources available from the world wide web. Images (e) (SEM inset and macroscopic photograph) and (f) taken from [1]. Image (g) reprinted from [2].

To construct artificial opals particles are synthesised through careful controlled chemical processes. After the synthesis, the particles are usually in the form of a suspension, either in water or other fluid. The artificial opal is obtained by bringing the particles together to form a dried solid structure. This can be done in several ways, from a simple gravitational sedimentation to manipulation individual colloids by nanorobots. The structuring of the particles in the bulk of the suspension was known since the 1970s [3]. However, it was in 1990s that the research in

colloidal suspensions and their crystallisation in dried structures intensified. This field of research attracted many groups from the scientific and technological community due to the promise of new interesting materials, particularly as optoelectronic materials. Although bandgaps in periodic dielectric media were known since the end of the 19th century [4], it was not until 1987 that Yablonovitch [5] proposed the existence of complete photonic bandgap in a three dimensional periodic structure that is known as photonic crystal. The interest on these structures increased notably, mainly due to the promise of founding a rapid method to build optoelectronic devices. In addition to the attractive applications, colloidal systems remain of large interest from a basic point of view, where they are an excellent experimental framework to test theoretical models for hard spheres systems, defects formation and their dynamics in atomic-like systems, among others.

Over the years, research provided many different techniques to structure colloidal particles. Nevertheless, despite the advances achieved in the field, there is not yet a suitable technique to obtain the desired structures. The difficulty arises in two different areas. On one side, there are specific requirements for the structure: large area of high quality crystals and, often, controlled defects. On the other side, there is the transition from a fluid suspension to the dried structure. This transition is ultimately governed by a balance between the capillary forces and the interaction forces between the particles and the surrounding surfaces (either of the substrate or of the already deposited structure).

The most popular methods to transfer the particles to the solid substrate are those inspired in Langmuir-Blodgett technique [6, 7]. They usually rely on evaporation-induced flows and capillary forces to transfer and consolidate the colloidal particles located near the contact line to a solid structure [8].

We believe that the understanding of the mechanisms involved in the dynamics of the transition from a fluid suspension to the dried structure is a key element to attempt the control over the process of structure formation. This control is fundamental to open new lines towards the construction of the technologically relevant structures.

In this work, we concentrate on the dynamical process that give rise to the structure in two experimental setups: vertical deposition and spin-coating. In the first case, the system is allowed to develop naturally. A weak DC electric field is applied to evaluate its effect on the dynamics. In the second case, a rotating substrate imposes an axisymmetric geometry that allows to study the dynamics of the particle structuring in relatively thin films ($< 10 \mu\text{m}$). Here, we used highly volatile fluids that give a fast crystal formation process ($\sim 1 \text{ s}$). This report is composed of two parts each of which encompasses one of the experimental systems studied.

The first part starts with an introductory chapter on the main characteristic of colloidal systems, we briefly review the principal electrokinetic phenomena that can occur in an electrostatically stabilised colloidal system. Then, we focus on the models that had been developed to predict the behaviour in convective self-assembly experiments in vertical deposition configurations. The following two chapters are dedicated to the detailed description of the experimental setup and results, with a special focus in the calculation process and the difficulties that arose from the discretisation of the data. We present the different structures and velocities observed at the conditions studied. This part finishes with a discussion on the relation between the contact line velocities and the deposited structure. We finish this section with a detailed discussion on the different parameters that affect the deposition process (previously deposited structure, local concentration near the contact line and interaction between particles and substrate) which give

rise to the observed dynamics.

In the spin-coating part, we first present a basic model developed by Emslie in 1958 for non-volatile viscous fluids [9] and its extension to volatile fluids made by Meyerhofer in 1978 [10]. Then, we briefly introduce the results obtained by several groups regarding the order that emerges in sheared colloidal suspensions. Then, we present the experimental setup and the image analysis used to characterise the thinning and drying dynamics. We finally describe the characterisation performed over the dried structure: *via* Atomic Force Microscopy (AFM) and Scanning Electron Microscopy (SEM). The results chapter summarises the thickness measured at the different conditions for the fluid stage and the dried structure. We also present the evolution of the dynamics of the long range orientational order, the dynamical regimes in the transition from the fluid suspension to the dried structure, and the difference in the morphology of the final deposit observed in the dried structure. The discussion chapter begins with an extension of the Emslie model to incorporate the evaporation rate effect on the dynamics. Then, we estimate the evaporation rate during the final dried stage using the different experimental data compiled. Finally, we discuss on the long range orientational order emerging in the fluid and dried structure.

This report finalises presenting the concluding remarks and outlooks for each experimental system.

Part I

Vertical deposition of water based colloidal suspensions

Chapter 1

Introduction

The formation of periodic ordered structures in colloidal systems has been of great interest for the scientific community for more than three decades. Early research focused on the structures emerging in the bulk of the suspensions or in the interface between two fluids [11–20]. When the possibility of obtaining a complete 3D photonic bandgap (PBG) was proposed in 1987 [5], the research groups started to focus on colloidal crystallisation as a process to obtain such structures [21–24]. The technological community foresaw the possibility of using these materials to develop a highly promising optoelectronic technology [25]. At this point, several techniques were developed [26–39], mainly directed to transfer the structures formed in the fluid phase to a solid form, more appropriate for technological manipulations. Most of those approaches were based on self-assembly that promised an easy and rapid process to obtain the desired structures [23]. The simplest self-assembly mechanisms rely on capillary forces to structure the particles during the transition between the fluid suspension and the dried structure. Despite these efforts, a process to efficiently structure colloidal particles in a 3D photonic crystal, or to properly control the structuring, has not yet been found. In the search, nevertheless, most studies concentrated more on the final structure characterisation than on the dynamics of the structure growth.

In this part, we concentrate in the characterisation of the dynamics and the deposits formed to identify the processes that control the growth of the deposits. In this part we focus on a method that has been used for several years, is the vertical deposition technique [26]. Here, the substrate is placed vertically while the fluid phase of the suspension is slowly evaporated. In this system, we applied DC electric fields to characterise their effect on the deposition process and evaluate its potential to control it.

The colloids used in this work lay in the upper limit of the colloidal region. In this experiments we used $1.3\ \mu\text{m}$ polystyrene spheres. These colloids arrange over the substrates surface in quasi 2D structures. The thickness is of the order of a few micrometres while the structure expands over larger areas of a few square millimetres. We did not have access to the precise rheology of the suspensions but we estimate that the viscosity, the density and the surface energy are of the same order of magnitude as those in water.

The structure formation is due mainly to the interaction between flows in the fluid phase and the particles in suspension. The main forces that govern the dynamics of this process are: capillary, viscous and inertial forces. The relative importance of these forces can be estimated from different dimensionless numbers.

The balance between inertial and viscous forces is considered by the Reynolds number:

$$\text{Re} \sim \frac{\rho V L}{\mu} \quad (1.1)$$

where ρ and μ are the density and shear viscosity of the fluid. V and L are the characteristic velocity and lenghtscales involved in the considered dynamics. For Re smaller than 10^{-2} the flow around the particle can be considered as laminar. In this limit, the Stokes law is valid and the forces acting on a particle are balanced by the viscous forces, so the particle moves following, approximately, the flow lines.

Another relevant dimensionless number is the Capillary number that compares capillary to viscous forces. The capillary forces are characterised by the surface tension γ :

$$\text{Ca} \sim \frac{\mu V}{\gamma} \quad (1.2)$$

Capillary forces dominate over viscous ones when Ca is smaller than 10^{-4} [43].

Finally, the comparison between the advection of particles following the flows and their natural diffusion is summarised by the Péclet number:

$$\text{Pe} \sim \frac{V L}{D} \quad (1.3)$$

where, D is the diffusion coefficient of the particles. We will take this coefficient to be of the order of $k_B T$. Here k_B is the Boltzmann constant and T is the absolute temperature. This number tells us how efficient are the flows at dragging particles with respect to their movement due to thermal fluctuations.

Typical values of these numbers for the vertical deposition configuration are much less than 1.

In this introductory chapter, we will present the concepts related to colloidal suspensions, the convective self-assembly process. We will also introduce a short description of the different models used for studying the colloidal crystallisation [26, 44–46].

1.1. Colloidal suspensions

Particles that can form a colloidal suspension cover a large range of sizes and shapes. Nevertheless, they are typically spherical particles of the order of 10 nm to 10 μm . The most commonly used materials are silica (SiO_2) or polymers. Both usually have larger densities than the fluid in which they are suspended (water, ethanol, ethylene glycol, among others). Thus, the particles tend to sediment due to gravity. Similarly, the interaction between particles is mostly dominated by electrostatic London-Van der Waals interaction that tends to agglomerate them [47], hence they form clusters that sediment faster than individual particles.

In most cases, agglomeration and sedimentation are undesired effects. The typical approach to counteract this effects is to prepare particles (or suspensions) such that there is a repelling force between particles. This force stabilises the suspension for times longer than the experimental timescale. The most common mechanisms to achieve this stabilisation are: electrostatic, steric or electro-steric repulsion. For silica spheres, the most used technique, is the electrostatic repulsion achieved by fixing charges on the surface of the particles (see Figure 1.1 (a)). For polymeric

particles, the three methods are widely applied. A steric repulsion is achieved by fixation of polymeric chains on the surface of particle. The chains act as a short range barrier that repel the particles when they are close to each other (see Figure 1.1 (b)). The combination of electrostatic and steric repulsion is achieved by placing charged groups on the exposed ends or along the steric chains (see Figure 1.1 (c)).

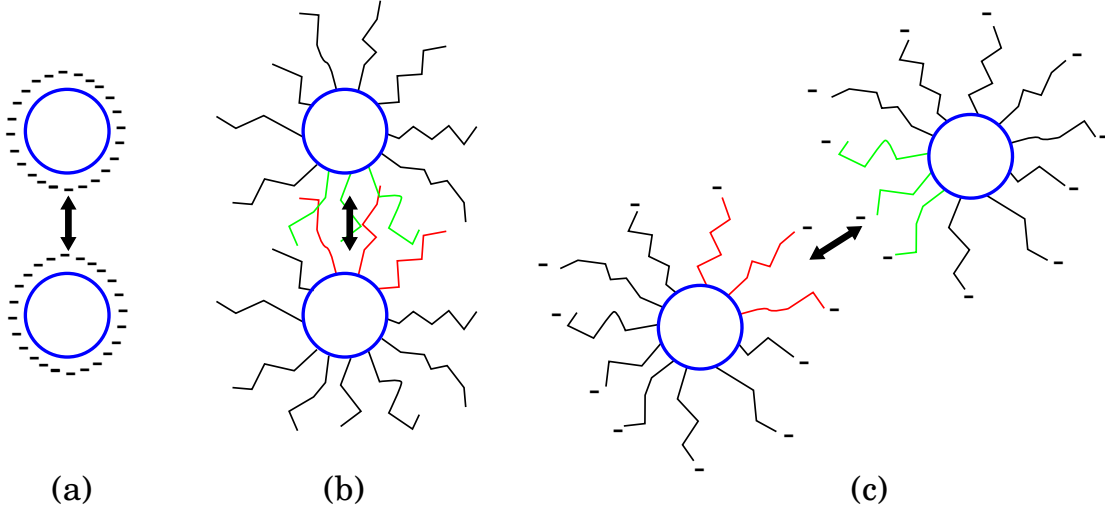


Figure 1.1: Stabilisation of colloids. Schematic representation of typical methods to incorporate repulsion forces that stabilise colloidal particles in suspension: (a) electrostatic repulsion, (b) steric repulsion, (c) electro-steric repulsion

In the vertical deposition experiments we used electrostatically stabilised polystyrene spheres of $1.3\ \mu\text{m}$ in diameter. For spin-coating experiments we used SiO_2 spheres that according to the provider (Fiber Optic Center inc.), they have large amounts of Silanol (Si-OH) on their surface that, in contact with polar fluids, generate negative charges that ease their redispersion.

1.1.1. Dispersive media

The fluid phase of a suspension can be composed of a pure fluid or of a mixture of miscible fluids. The main interest, for using different fluids, is to ease visualisation through the suspension (refractive index matching), to avoid sedimentation (density matching) or to control the temporal lengthscale of the dynamics (when colloidal crystallisation is obtained through the drying of the suspension). In this work, we choose to use simple fluids to avoid additional complexity on the dynamics, that could be originated by an unbalance in the proportion of the mixture during the experiments. We dispersed polystyrene particles in ultrapure water, in the vertical deposition experiments, and silica particles in acetone or methyl-ethyl ketone, in the spin-coating experiments.

1.1.2. Electrical double layer

The problem of a charged surface in contact with a fluid with charged species (either polar molecules or electrolytes) has been studied for many years since it is encountered in many situations, from electrolyte solutions to plasma physics [47]. The general problem is very complex and

depends on the precise nature of the charged species and on the type of surface. There are many different models to represent the potential each of which adequate to a particular experimental situation. Which is more appropriate to a particular situation depends on many parameters. Even the largely accepted double layer model is a current matter of discussion [48]. However, most used models have the common feature of distinguishing two charged regions: one inner, near the surface, where the charged species had been adsorbed by the surface; and one outer, where ions and counterions form a mobile diffuse layer. A more precise consideration separate the inner region in two areas one free of charge (in contact with the surface), and one with the adsorbed charge (at a distance of $0.1\sim0.5$ nm, depending on the charge nature [47]). Nevertheless, if we are only interested on the amount of charge present in each region and the approximated size of the outer charged area, most models can be used indistinctly. Hence, we will introduce one of the simplest models, proposed by Stern in 1924. It is commonly known as Gouy-Chapman-Stern double layer model. Here, the charge of the surface is compensated by ions, adsorbed in the charged surface, and by a diffuse cloud, of mixed ions and counterions. In this diffuse layer Brownian motion maintain ions and counterions in movement. On the contrary, the adsorbed ions move with the particle. In figure 1.2 (left) we show a schematic representation of this distribution.

The adsorbed ions form a monolayer over the surface (Stern layer). The diffuse layer, on the other hand, is a mobile cloud susceptible to external fields. This distinction in the mobility of each layer leads to the definition of a slipping or shear plane. In general, the slipping plane is defined in the transition between these two regions [49]. Although rigorously the slipping plane does not coincide with the end of the Stern layer, for the system that we consider the slipping plane and the Stern layer can be assumed to coincide (see Figure 1.2 right).

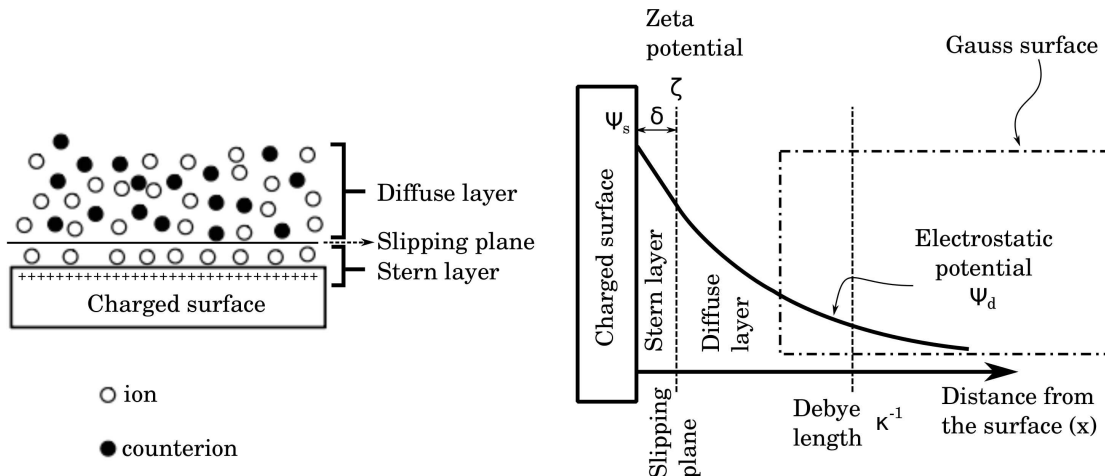


Figure 1.2: Schematic representation of the Stern double layer model. Left: Ions and counterions distribute according to the competition between the attractive electrostatic force and the dispersive Brownian motion. Right: Electrostatic potential given by the electrolytes distribution around the surface. Sketches are not at scale.

The electrostatic potential near a charged surface is the potential Ψ_d schematised on Figure 1.2 (right). For the derivation of this potential, we start with the Gauss law applied to a rectangular

box that compares the potential far from the surface to the one in an arbitrary point in the diffuse layer (see Figure 1.2 right):

$$\nabla \cdot \vec{D} = \nabla \cdot \epsilon \vec{E} \rightarrow \Delta\phi = -\frac{\rho}{\epsilon_0 \epsilon_m} \quad (1.4)$$

here, we used $\vec{E} = -\nabla\phi$ and assumed that the permittivity of the fluid ϵ_m is constant. The ions will be distributed by the competition between the attractive electrical potential and the randomising effect of the Brownian motion. Therefore, the distribution can be expressed by the Boltzmann equation [50]:

$$n_i = n_i^0 e^{-w_i/k_B T} \quad (1.5)$$

where, w_i is the work performed to bring the ion i from the bulk solution (where the potential is ϕ_s) to the arbitrary point in the diffuse layer (at a potential ϕ); n_i^0 is the concentration of ion type i in the bulk solution; k_B is the Boltzmann constant and T the absolute temperature. As a first approximation, it is assumed that the ions are point charges, thus w_i :

$$w_i = z_i e(\phi - \phi_s) = z_i e\psi \quad (1.6)$$

where z_i is the valence of the ions, e is the electric charge of the electron, and $\psi \equiv \phi - \phi_s$ is the potential of the arbitrary point of the diffuse layer with respect to the potential in the bulk solution. Then, the total charge included in the Gauss surface is

$$\rho = \sum_i n_i z_i e \quad (1.7)$$

Replacing equation 1.5 in 1.7, and using the resulting expression for ρ in 1.4, the potential in the diffuse layer will be given by:

$$\Delta\psi = \frac{-1}{\epsilon_0 \epsilon_m} \sum_i n_i^0 z_i e e^{-z_i e\psi / k_B T} \quad (1.8)$$

Here, we assumed that ϕ_s is constant. When the electrostatic energy in the diffuse layer is small with respect to the thermal energy (i.e. $|z_i e\psi| \ll k_B T$), the exponential can be expanded ($e^{-x} = 1 - x + \mathcal{O}(x^2)$) and keeping the first two terms we get:

$$\Delta\psi \approx \frac{-1}{\epsilon_0 \epsilon_m} \left(\sum_i n_i^0 z_i e - \sum_i n_i^0 z_i^2 e^2 \psi / k_B T \right) \quad (1.9)$$

the first sum should be zero to maintain the electroneutrality of the bulk solution. Thus, in this approximation, the potential would be given by:

$$\Delta\psi \approx \left(\frac{\sum_i n_i^0 z_i^2 e^2}{\epsilon_0 \epsilon_m k_B T} \right) \psi = \kappa^2 \psi \quad (1.10)$$

This approximation is known as the Debye-Hückel approximation and κ is the Debye-Hückel parameter. The inverse of this parameter measures the extent of the diffuse layer and is known as the Debye length κ^{-1} .

The solution to the equation 1.10 is of the form $\psi = \psi_0 e^{-\kappa x}$. Since the particles are spherical we change our origin of the coordinate system to the centre of the particle. Thus, the potential will be given by:

$$\psi(r) = \psi_0 e^{-\kappa(r-R^s)} \quad (1.11)$$

where $R^s = R + \delta$ the radius of the sphere plus the Stern layer thickness (see Figure 1.2 right), ψ_0 is the Zeta potential, and r is the distance measured from the centre of the sphere.

Although this equation was derived in Cartesian coordinates κ^{-1} is, typically, of the order of 10 nm. As our particles radius (0.65~0.25 μm) are much larger than the Debye length, equation 1.11 can be applied to them.

Under the same approximation ($|z_i e \psi| \ll k_B T$) the Zeta potential for a spherical particle, of radius R , with a total charge Q , can be estimated from [51] as:

$$\zeta = \frac{Q}{4\pi\epsilon_m\epsilon_0 R(1 + \kappa R)} \quad (1.12)$$

The interaction potential between two charged surfaces (particle-particle and particle-substrate) is the superposition of the potential of each surface. The interaction potential includes two contributions, one repulsive (given by superposition of two potentials of the form 1.11, U_R) and one attractive (known as Van der Waals potential, U_A). The Van der Waals forces, in general, include three different types of atomic and molecular interactions. They originate from permanent dipoles, induced polar actions, or quantum mechanical forces. The last type of forces are called London dispersion forces and are usually the most important ones. When they are seen at a macroscopic level, the Van der Waals forces can be represented by a potential energy that is inversely proportional to the separation between particles centres d [51]:

$$U_A \sim \frac{H}{d^2} \quad (1.13)$$

Here, H is the Hamaker constant that can be related to the material properties: density ρ , molecular weight M and a particle-particle pair interaction coefficient C :

$$H = \left(\frac{\rho\pi N_A}{M} \right)^2 C \quad (1.14)$$

where N_A is the Avogadro number.

The repulsive potential energy is well represented by the DLVO (after Derjaguin and Landau, Verwey and Overbeek) approximation [52] given by:

$$U_R(d) = \frac{Q_{eff}^2 e^2}{\epsilon_0 \epsilon_m} \left[\frac{e^{2\kappa a}}{(1 + \kappa a)^2} \right] \frac{e^{-\kappa d}}{d} \quad (1.15)$$

Here, Q_{eff} the effective surface charge that includes the Stern layer.

In Figure 1.3, we show a schematic representation of the typical form of each potential and their superposition (U_T). The total interaction potential has two minima: the primary minimum, is a non reversible position, at which particles will remain despite sonication. The secondary minimum is a reversible position, where sonication allows to recover a homogeneous suspension.

1.2. Transport phenomena

The formation of a colloidal structure involves a transition from a fluid suspension to the dried deposit. During the formation of these deposits there is a transport of colloidal particles from

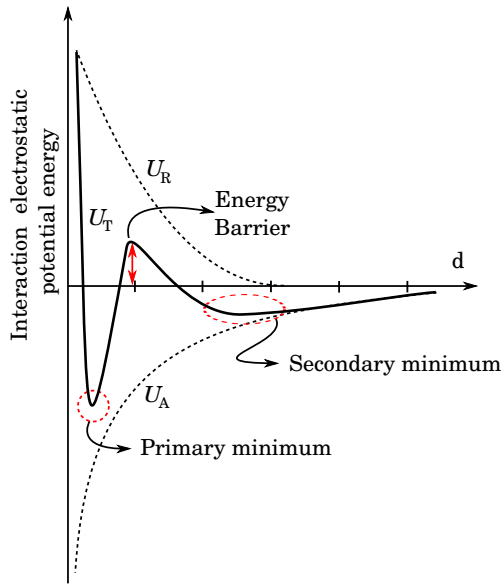


Figure 1.3: Interaction potential between charged surfaces. The total potential (U_T) is the result of the superposition of an attractive potential (U_A , corresponding to a London-Van der Waals interaction) and repulsive potential (U_R , corresponding to an electrostatic interaction). The two minima are separated by an energy barrier. The main intention of the stabilisation of a suspension (see Figure 1.1) is to have a barrier large enough, to avoid particles to cross it in storage conditions.

the bulk of the suspension to the meniscus where the particles deposit. The stabilisation charge, present on the colloids surface, and the diffuse layer of ions that this charge induces, makes the particles susceptible to external electric fields. Additionally, since the mobile diffuse layer and the particle charge have opposite signs, there are several transport processes that can occur and, in some situations, compete. The electrokinetic phenomena are those in which the particle superficial charge, and its induced cloud, interacts with an external field. These phenomena include fields arising from a large variety of natures: from gravitational or mechanical fields to chemical gradients or ultrasonic fields. In the following, we will define and present the origin of those that could be present in our system. Later in this section, we will introduce other transport mechanisms and phenomena that are not related to electrokinetic phenomena but can be relevant for our study.

1.2.1. Electrokinetic phenomena

In our experimental configuration, we applied a constant potential between parallel plates in order to evaluate the effect of an electric field on the dynamics of the colloidal self-assembly process. Hence, from the different electrokinetic phenomena, we will focus on those arising from the interaction with external DC-fields. We will also introduce the gravitational and pressure effects since flows play a fundamental role on the formation process. Therefore, the main electrokinetic processes that could have an affect in our system are:

1. *Electrophoresis:* Since the particle is surrounded by an electrical double layer, in the presence of an external electric field several forces will be induced. There will be a net force applied

over the colloidal particle due to its charged surface (including the Stern layer), this is the driving electrostatic force \mathbf{F}_1 . As the particle is immersed in a fluid, its viscosity will limit the velocity of the particles *via* a viscous force \mathbf{F}_2 . The electric field will act, also, on the surrounding diffuse layer that, as the charge in this layer is opposite to the one of the particle, will apply a braking force \mathbf{F}_3 (electrophoretic retardation force). Finally, the displacement of the diffuse layer with respect to the particle will generate a net dipole moment that also will reduce the final velocity of the particle (polarisation force \mathbf{F}_4).

2. *Dielectrophoresis*: This effect is the response of colloidal particles to a spatially heterogeneous electric field. This effect does not rely on the charge of the particle but on its polarisability. Thus, its effects are evident even in electrically neutral particles.
3. *Electro-osmosis*: In the presence of an external electric field the diffuse layer experiences an electrostatic force which displace the cloud with respect to the charged surface. This movement induces a flow around the particle that, depending on the direction of the field and the sign of the charges, can induce attraction or repulsion between the particles near a charged surface [53].
4. *Streaming potential*: if the diffuse layer is subjected to a pressure difference the ions present on it will move with the surrounding fluid. This movement is, in essence, an electrical current. The electric potential drop due to this current is the *streaming potential* [54].
5. *Sedimentation potential - Dorn effect*. Under the action of gravity the colloidal particles tend to sediment. In their movement, the particle moves ahead from the cloud, thus an inhomogeneous charge distribution appears in the system. If we assume that the particles are negatively charged there will be a net balance of positive charges on the top that gives rise to a dipole moment through which the particle interact with the external field.

1. Electrophoresis. In general, the electrophoretic effect is the result of the balance between four forces: \mathbf{F}_1 , \mathbf{F}_2 , \mathbf{F}_3 and \mathbf{F}_4 . The last two forces depend on the precise characteristics of the diffuse layer, what is more, usually they depend on each other and on the ionic species involved [54]. Hence, as a first approximation we will neglect their contribution and consider a balance between the driving electrostatic force and the viscous force. For spherical particles, Stokes' flow approximation can be applied. Thus, in steady state the two forces will be balanced giving a zero external force over the colloidal particle:

$$\begin{aligned} \sum \vec{F}_{ext} &= m\vec{a} = 0 = \vec{F}_E + \vec{F}_{vis} \\ \vec{F}_E &= -\vec{F}_{vis} \\ Q\vec{E} &= -6\pi\mu R\vec{u} \\ |u| &= \frac{|Q\vec{E}|}{6\pi\mu R} \end{aligned} \tag{1.16}$$

Where, R is the radius of the particle, Q the surface charge (including the Stern layer charge), μ is the viscosity of the fluid, \vec{E} is the external electric field and u is the velocity of the particle. Then, as a first approximation the steady state velocity of a particle will be given by equation 1.16.

2. Dielectrophoresis. First reported by H. A. Pohl in 1951 [55], this effect arises when a particle is in the presence of a spatially heterogeneous electric field. Although this effect is mostly studied under AC electric field, in principle it is also present on DC experiments. The effect of this force will depend on the electrical permittivity of the particles ϵ_p with respect to the one of the medium ϵ_m . On one hand, if $\epsilon_p > \epsilon_m$ the particles are attracted to the regions of stronger fields. On the other hand, if $\epsilon_p < \epsilon_m$ the particles are repelled from the strong field regions. The dielectrophoretic force applied over a particle of radius R will be given by [55]:

$$\vec{F} = 2\pi\epsilon_m R^3 K \nabla E_0^2 \quad (1.17)$$

where E_0 is the module of the applied electric field and K is known as Clausius-Mossotti function:

$$K = \frac{\epsilon_p - \epsilon_m}{\epsilon_p + \epsilon_m}$$

From this expression we see that \vec{F} has the following properties:

- it is proportional to the particle volume,
- it is parallel to the gradient of the electric field intensity.
- it depends on the magnitude and sign of the Clausius-Mossotti function.

3. Electro-osmosis. This phenomena can be considered in someway as the counterpart of the electrophoresis. Electro-osmotic flows are the result of an electric field interacting with the diffuse double layer, generated by the surface charge. It differs from electrophoretic in that the surface is assumed at rest with respect to the fluid. If we consider a particle close to the substrate, its movement will be restricted by the surface. Then, the interaction between the particle and the electric field can be studied in terms of electro-osmotic flows. The diffuse layer is composed of a mixture of oppositely charged species, but with a net charge that neutralises the surface charge (together with the charges in the Stern layer). Hence, electro-osmotic flows and electrophoretic forces will act in opposite direction. In the electro-osmotic effect only the electric field parallel to the charged particle surface is taken into account. At the lengthscale of electro-osmotic flows (that is, in the order of κ^{-1}), the particle surface can be considered as a plane. Then, considering the axis defined in Figure 1.4, the velocity of the ions located in the diffuse layer will be given by [56]:

$$v_x(y) = \frac{\epsilon}{4\pi\mu} [\Psi(y) - \zeta] E^s \quad (1.18)$$

where, v_x is the velocity profile of the counterions in the diffuse layer, ϵ and η are the permittivity and viscosity of the fluid, $\Psi(y)$ is the electrostatic potential as a function of the y -coordinate. This potential equals the Zeta potential at $y=0$, hence, a no slip condition ($v_x(0) = 0$) was imposed in the derivation of equation 1.18. E^s is the electric field at a distance κ^{-1} from the particle surface.

4. Streaming potential. An estimation for this effect can be obtained from the expression deduced for a capillary tube of radius a on which a flow is imposed by a pressure difference Δp (see Figure 4.1(a)). The surface of the capillary, in contact with the fluid, is negatively charged. Thus, the flow drag the positively charged diffuse layer generating an electrostatic potential. Assuming that

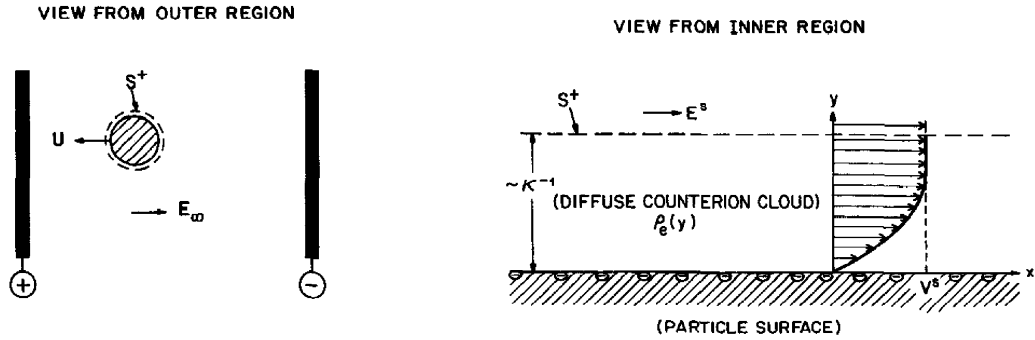


Figure 1.4: Schematic representation of a colloidal particle subjected to an external homogeneous electric field. Left: Electrophoresis - Under the action of an external electric field E_∞ the colloidal particle acquire a velocity U towards the oppositely charged surface. Right: Electro-osmosis - the charges ρ_e in the diffuse layer (diffuse counterion cloud) will present a velocity profile $v_x(y)$ as sketched; $v_x = 0$ at $y=0$ (no slip condition at the slipping plane, see Figure 1.2) and a limit velocity V^s at the Debye length κ^{-1} . E^s is the electric field at the outer edge of the double layer S^+ . Recall that κ^{-1} is on the order of 10 nm, thus the rectangular axis approximation presented here is valid. Images extracted from [56].

$\kappa a \gg 1$, where a is the diameter of the capillary tube, the streaming potential is observed to be independent of the capillary diameter and it can be expressed as [54]:

$$V_{str} = \frac{\epsilon_0 \epsilon \zeta \Delta p}{\eta K} \quad (1.19)$$

where K is the bulk conductivity.

5. Sedimentation potential. In this case, the sedimentation of particles induce a displacement of the diffuse layer with respect to the particle core (see Figure 4.1(b)). This displacement generates a electric dipole moment \vec{p} which give rise to the potential drop in the direction of gravity. The radius of our particles R satisfy that $\kappa R \gg 1$. Hence, the limit formulation derived by Smoluchowski is applicable and the sedimentation velocity V_{sed} will be given by [54]:

$$V_{sed} = -\frac{\epsilon_0 \epsilon \zeta \Delta \delta g \phi}{\eta K} \quad (1.20)$$

where, $\Delta \delta$ is the density difference between the particle and the fluid and ϕ is the volume fraction of the suspension.

1.2.2. Other phenomena

In addition to the electrokinetic effects, there are a series of phenomena that affect the transport of particles, specially near the contact line. We will consider three phenomena: electrowetting, electrostatic, and capillary forces.

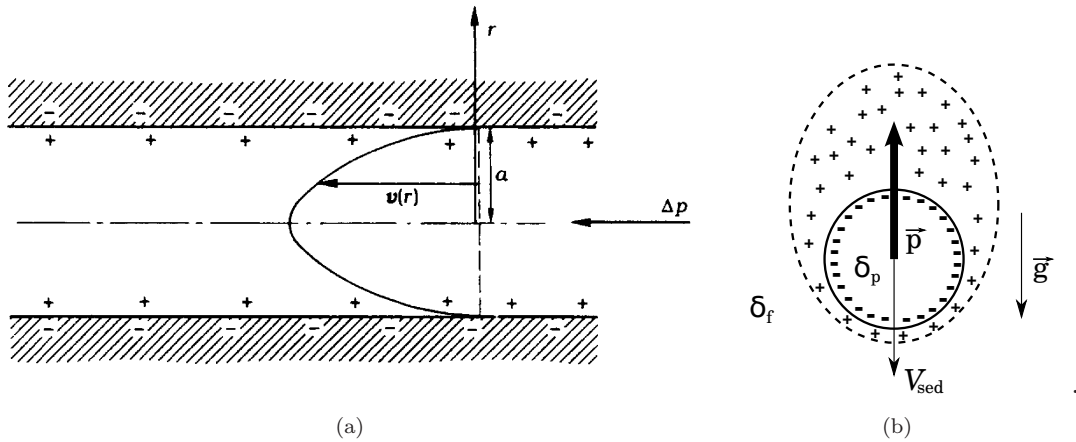


Figure 1.5: (a) Schematic representation of a cylindrical capillary tube of radius a where a difference of pressure Δp impose a Poiseuille-type flow. The surface of the capillary has a negative surface charge that generates a diffuse layer oppositely charged (represented by the plus signs in the figure). Image extracted from [54]. (b) Microscopic representation of the origin of the sedimentation potential. Under the effect of the gravity the movement of the particle perturb the diffuse layer (represented by the plus signs), δ_f and δ_p are the density of the fluid and the particle, V_{sed} is the velocity of sedimentation, and \vec{p} is the induced electric dipole.

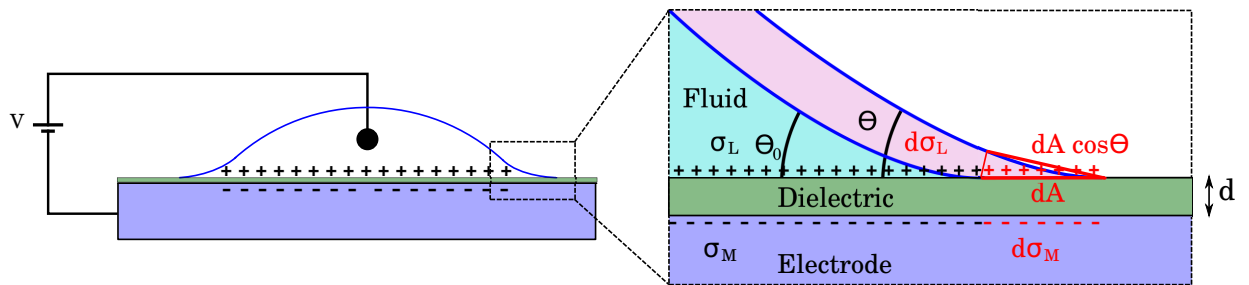


Figure 1.6: Schematic design of an electrowetting experiment. When voltage is applied the contact angle modifies from the Young angle θ_0 to a new equilibrium position θ . This is accompanied with an increase of the wetting area dA ($dA \cos\theta$ is the projection over the fluid free surface). The initial charge density σ_L and σ_M (in the liquid and electrode, respectively) increases by a magnitude $d\sigma_L$ and $d\sigma_M$. The system as a whole behaves as a parallel capacitor with a dielectric layer (thickness d)

1. Electrowetting. The standard setup in an electrowetting experiment is composed of two electrodes, an insulating layer and the conducting fluid (see Figure 1.6).

Following Verheijen and Prins [57], consider that, due to the applied voltage, the drop wets an area dA larger than when the voltage is zero. Then, the change in free energy is given by:

$$dF = \gamma_{SL} dA - \gamma_{SV} dA + \gamma_{LV} dA \cos\Theta + dU - dW_B \quad (1.21)$$

where, γ_{SL} , γ_{SV} and γ_{LV} are, respectively, the free energies between the solid/liquid, solid/vapour and liquid/vapour interfaces without electric field. The energy used to create the electric field

between the liquid and the counter electrode is denoted as dU , the contact angle without field is Θ_0 (in Figure 1.6). The term dW_B represents the work made by the power source to supply the extra charge. If we consider the fluid as a conductive media, the ensemble behaves as a parallel capacitor where the electrostatic energy is stored in the field inside the dielectric media. The stored energy can be calculated as usual:

$$\frac{U}{A} = \int_0^d \frac{1}{2} \vec{E} \cdot \vec{D} dz = \frac{1}{2} dED \quad (1.22)$$

where z is the direction perpendicular to the substrate, and d is the thickness of the dielectric layer. \vec{E} is the electric field and \vec{D} the displacement charge. Thus, the change in F due to the redistribution of charges (due to an infinitesimal change on the droplet wetting area dA) will be:

$$\frac{dU}{dA} = \frac{1}{2} dED = \frac{1}{2} d \frac{V}{d} \sigma_L = \frac{1}{2} V \sigma_L \quad (1.23)$$

where σ_L is the surface charge density in the area of the droplet that is in contact with the dielectric. Finally, the work made by the power supply can be expressed as:

$$\frac{dW_B}{dA} = V \sigma_L \quad (1.24)$$

Replacing equations 1.23 and 1.24 in 1.21, and minimising F (i.e. $dF/dA = 0$), we obtain the expression for the traditional Young equation corrected with the electrowetting contribution:

$$\begin{aligned} \frac{dF}{dA} &= \gamma_{SL} - \gamma_{SV} + \gamma_{LV} \cos \Theta + \frac{1}{2} V \sigma_L - V \sigma_L = 0 \\ \gamma_{LV} \cos \Theta &= \gamma_{SV} - \gamma_{SL} - \frac{1}{2} V \sigma_L + V \sigma_L = \gamma_{SV} - \gamma_{SL} + \frac{1}{2} \frac{d}{\epsilon_0 \epsilon_r} \sigma_L^2 \\ &= \gamma_{SV} - \gamma_{SL} + \gamma_{EW} \end{aligned} \quad (1.25)$$

where, we used Gauss law ($\sigma_L = \epsilon_0 \epsilon_r V/d$, ϵ_r and ϵ_0 are the relative permittivity of the dielectric layer and the permittivity of vacuum, respectively). In equation 1.25, the surface tension associated to the electrowetting was labelled as: $\gamma_{EW} = \frac{1}{2} \frac{d}{\epsilon_0 \epsilon_r} \sigma_L^2$. Additionally, this equation can be reformulated by incorporating the Young expression for the contact angle. To do this, we consider equation 1.21 without electric field ($dU = 0$ and $dW_B = 0$) and replace the terms common to equation 1.25:

$$\begin{aligned} \frac{dF}{dA} &= \gamma_{SL} - \gamma_{SV} + \gamma_{LV} \cos \Theta_0 = 0 \\ \gamma_{SV} - \gamma_{SL} &= \gamma_{LV} \cos \Theta_0 \\ \gamma_{LV} (\cos \Theta - \cos \Theta_0) &= \frac{1}{2} \frac{d}{\epsilon_0 \epsilon_r} \sigma_L^2 \end{aligned} \quad (1.26)$$

2. Electrostatics. Early in this chapter, we mentioned that the interaction between charged surfaces is mainly governed by the superposition of two potentials: one attractive and the other repulsive. The electrostatic effect of the DC electric field can be understood as an increment of the potential represented in equation 1.15 [58]. In our experimental geometry, the parallel plate configuration will tend to give an homogeneous field. Nevertheless, perturbations are unavoidable,

in particular in the contact line where the material changes (from water to humid air). Despite this, when a particle approaches the substrate, the interaction between particle and substrate takes place solely through water, hence, we will assume that the medium is homogeneous and the change in the electric potential consists only in a larger U_A (in figure 1.3). In our results we focus in the positive electrode, thus, we will only consider the interaction of the particles with the positive electrode. As the particles are negatively charged, the interaction potential will be represented by the superposition of two attractive potentials. In Figure 1.7 we sketched what would be the effect contribution of an increasing DC field over the general potential.

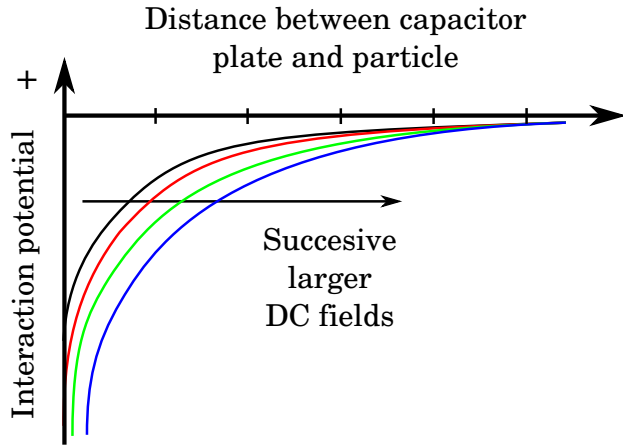


Figure 1.7: Schematic representation of the effect of superimposing a homogeneous field to the London-Van der Waals interaction potential (Figure 1.3) between charged surfaces.

3. Capillary forces. If particles in suspension behave as hard spheres, an increase of the concentration drives the system through a first-order transition to a crystal order [11, 59]. Different structures can be formed by coupling the interaction potential with external fields [60–63]. Nevertheless, when the suspension dries, the capillary forces play a major role in the interaction between particles. During the drying process the capillary processes overcome the effect of the electrostatic interaction and they govern the colloidal crystal formation process [44, 45]. In the following, we will introduce the basic concepts related to the capillary effect over particles on an interface.

Vertical deposition crystallisation has been used extensively in several configurations [26, 45, 64–67]. Nevertheless, the phenomena that give rise to the crystal was firstly studied on drying horizontal drops [8, 68] and remained largely unchanged on the vertical deposition scheme. This is due to that suspensions are stabilised such that gravitational forces are negligible. Additionally, in vertical deposition experiments we used polystyrene spheres, the density of which is close to the one of water (the dispersive medium). Thus, gravitational effects are minimised.

The process through which the dried crystal is built was first named as convective self-assembly by Adachi *et al.* [8] referring to the formation of striped deposits at the contact line of an horizontal drop (coffee ring problem). Conceptually, there are two processes taking place which are responsible of the crystal formation. On one hand, the evaporation brings particles to the contact line where they start to deposit on the substrate. On the other hand, when particles

are close enough, the capillary forces pull them together. Once a structure is being formed, the evaporation of the fluid through its pores induces new hydrodynamic flows that favour the growth of the structure.

To be more precise, consider the Figure 1.8(a). The evaporation through the deposited structure can be characterised by a flow (J_e). This depends on the exposed area which, in turn, depends on the structure deposited and on the height of the fluid wetting this structure (l , in Figure 1.8(a)). The continuity equation requires this flow to be balanced by one coming from the bulk of the suspension. This flow can be separated in two terms: the flow of particles (J_p) and the flow of the fluid phase (J_w). As the flow gets to the previously deposited structure, the fluid filters through the structure pores, while the particles become part of the structure. In Figure 1.8, we label the velocity at which the structure grows as v_c . In this process, there is not a well defined mesoscopic contact line. While the structure is wet, each deposited particle has a contact line (see Figure 1.8 (b)). Additionally, the point where the deposited structure finish and the meniscus starts could be difficult to establish, in particular when different structures are formed simultaneously [69, 70]. Therefore, in this work, when we mention the contact line, we refer to the position at which the structure is growing. Then, the velocity of the contact line is actually the velocity of the growing front, or in other words, the velocity at which the structure is formed. This is the velocity denoted as v_c in Figure 1.8 (a).

Capillary forces become relevant once the particles are close together. If the particles have the same wetting properties the force is always attractive [71]. Thus, capillary forces bring the particles together contributing to form a compact structure. Nevertheless, in a situation like the one showed in Figure 1.8 (right) the attractive capillary force will compete with the interaction between the particle and the substrate in which it rests. The interaction (not shown in the Figure) can be interpreted as a disjoining pressure that push particles over the substrate surface. This pressure is usually represented by an interaction potential, like the one sketched on Figure 1.3, that only depends on the charges of each surface. Hence, if the charges in the surfaces remain constant, the interaction only depends on the distance between surfaces. Capillary forces, on the contrary, become stronger as evaporation takes place. This can be understood from the dependence of the capillary force upon the geometric parameters of the contact line [71]. In Figure 1.8(b) (taken from Kralchevsky and Nagayama's book), we show two spheres interacting by immersion capillary forces, from [71] the direction and magnitude of those forces can be determined from:

$$F_{Ca} \sim \sum_{k=1,2} R_k (h_k - h_{k\inf}) \cos \alpha_k \quad (1.27)$$

where R_k is the radius of the sphere, $h_{k\inf}$ is the height of the fluid layer far from the spheres and h_k is the position of contact line over the sphere respect to $h_{k\inf}$, α_k is the contact angle, and the k -index refers to each sphere.

In a dynamical situation, evaporation tends to decrease the level of the wetting fluid. If we consider the situation sketched in Figure 1.8(b), after certain time, evaporation could produce a change in the angles or heights at which the fluid phase wets the particles. Dynamically, the contact angle is stable over a range defined by the advance and receding contact angle [72]. Thus, as the level of fluid decrease, the contact angle α_k decreases, as long as it is larger than the receding contact angle. While, the wetting height h_k remains constant. Then, from equation 1.27 we see that the capillary force increases.

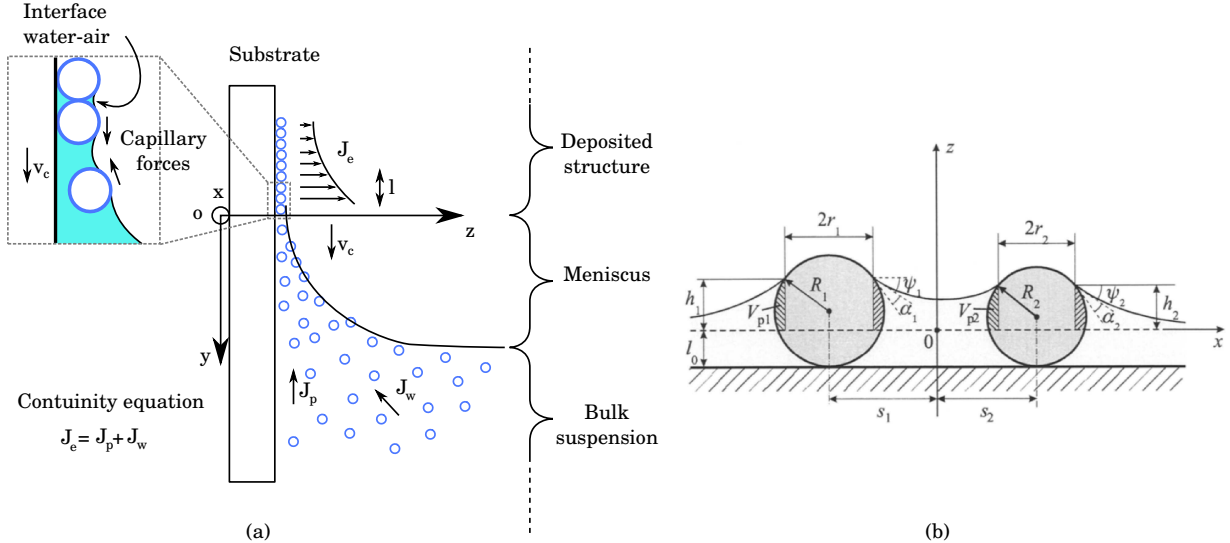


Figure 1.8: Convective assembly. (a) Schematic representation of a convective assembly process: evaporation on structure (J_e) induce flows from the bulk suspension (through the continuity equation). Once the particles are close enough capillary forces bring them together to form the structure. v_c is the velocity at which the structure grows. (b) Schematic representation of capillary interaction between two spheres (extracted from [71]). The dimensions marked are: l_0 , the height of the fluid layer far from the spheres; h_1 h_2 , the position of contact line over the sphere respect to l_0 ; α_1 , α_2 , Ψ_1 and Ψ_2 , the contact angles and meniscus slope of the fluid phase with each sphere; s_1 and s_2 , the distance to the centre of each sphere with respect to the middle point; $2r_1$ and $2r_2$, the diameter of the non-wetted area of the sphere; V_{p1} and V_{p2} , volume of the particle that displace fluid (outside $2r_1$ and $2r_2$). This volume is used to correct the gravitational potential energy (see [71] for further detail).

Once the contact angle reaches the dynamical receding contact angle, the contact line moves downwards. Now, the capillary force depends upon $h_k - h_{k\inf}$ while $\cos\alpha_k$ remains constant.

As a corollary, given a set of particles in a determined spatial configuration, if the interaction force between the substrate and the particles deposited on it, associated to the disjoining pressure, is larger than the capillary forces when the contact line start to recede, the configuration will remain unchanged. If, on the other hand, the capillary force overcome the particle-substrate interaction, the particles are pulled together to form a compact structure.

1.3. Models of evaporation induced self-assembly

Several models had been developed to predict the deposit that will result from a colloidal crystallisation process. One of the first models was developed by Dimitrov and Nagayama [44] for a dip-coating experimental setup. There, the substrate is softly lift as the structure grows, i.e. the substrate has a velocity v_w that equals v_c in Figure 1.8(a). Under this conditions, they developed a model to predict the withdrawal velocity v_w necessary to deposit a structure of k layers, given by the expression:

$$v_w = v_c^{(k)} = \frac{\beta l}{0.605} \frac{J_e \phi}{kd(1 - \phi)} \quad (1.28)$$

here, ϕ is the particle volume fraction of the suspension (thus, $1 - \phi$ is the water volume fraction), k is the number of deposited layers, d is the diameter of the particles, J_e is the water evaporation flux per unit length (in the vertical direction, it has velocity units), β is a proportionality factor that relates the macroscopic mean velocity of the particles and water molecules (thus, close to 1 for inertial particles). In this model, 1 is used as a fitting parameter, it can be interpreted as the height that the fluid wets over the deposited structure (see Figure 1.8 (a)). The constant 0.605 is the sphere volume fraction for a perfect hexagonal monolayer, that is the volume of spheres over the total volume of structure.

This early model is not directly applied to vertical deposition since it considers that the substrate is in movement. To overcome this difference, Jiang *et al.* [26] considered that the substrate is motionless ($v_w = 0$) and that $J_e = v_c$, hence simplifying the equation to:

$$k = \frac{\beta l}{0.605d} \frac{\phi}{1 - \phi} \quad (1.29)$$

This model implicitly assumes that the concentration of particles is constant along the whole experiment, i.e. ϕ does not change. Thus the model is limited to situations where the change in fluid phase (due to evaporation) and solid phase (due to deposition) is balanced. Shimmin *et al.* [45] consider a slow vertical deposition process and they assume that the structure forms near the surface and, then, is transported towards the substrate (as in a Langmuir-Blodgett process [6, 7]). On these premises, they derived a similar equation:

$$h(t) = \frac{\phi_0 v_e}{(1 - \epsilon)} \left(\frac{\beta l}{v_c(1 - \phi)} + t(1 - \frac{v_s}{v_e}) \right) \quad (1.30)$$

where ϕ_0 is the initial concentration of the suspension, t the elapsed time, v_e evaporation velocity and v_s the sedimentation velocity of the particles. The first term of Equation 1.30 is the original Dimitrov model (equation 1.28), where the withdrawal velocity was taken as the growth velocity of the structure. The second term corresponds to a linear increase associated to a local increment of the concentration of particles near the meniscus. To justify the latter term, the authors of [45] considered a situation where the surface of the suspension recedes as the fluid evaporates. Considering that, initially, the structure is not deposited on the substrate, the particle concentration, near the surface, increases. This was confirmed by them through numerically solving the equation for the sedimentation of particles [50]:

$$\frac{\partial \phi}{\partial \tau} = \frac{\partial \phi}{\partial \chi} - \frac{v_s}{v_e} \frac{\partial (\phi K(\phi))}{\partial \chi} + \frac{D_0}{hv_e} \frac{\partial \left(K(\phi) \frac{d}{d\phi} (\phi Z(\phi)) \frac{\partial \phi}{\partial \chi} \right)}{\partial \chi} \quad (1.31)$$

here, h is the position of the free surface (measured from some arbitrary origin), D_0 is the Stokes-Einstein diffusion coefficient, $K(\phi)$ is the sedimentation coefficient and $Z(\phi)$ the compressibility factor for the particular colloidal system, $\tau = tv_e/h$ y $\chi = x/h$ are the dimensionless time and distance. Shimmin *et al.* [45] observed that for polystyrene particles (1 μm diameter), at an initial concentration of 0.008%, the concentration of particles near the free surface increased with time. This result is presented on Figure 1.9 (extracted from [45]). The coordinate Depth in the

figure is measured with respect to the free surface, i.e. the reference frame moves solidary to the receding free surface.

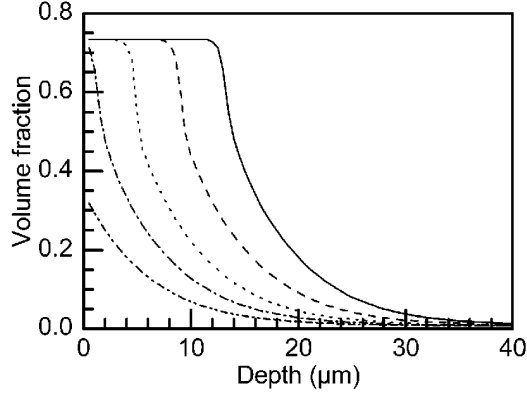


Figure 1.9: Solutions for equation 1.31 for an initial concentration of 0.008%. Different lines correspond to distinct times (measured in terms of distance that the free surface moves respect to its position at time $t=0$): 0.3 mm (dash-dot-dot), 0.6 mm (dash-dot), 1.0 mm (dotted line), 1.5 mm (dashed line) and 2 mm (solid line).

This was the first model that included a local change of concentration near the free surface. Nevertheless, it assumed that the rate at which the structure is deposited is small enough to neglect the number of particle deposited respect to the number of particles that are been incorporated to the accumulation zone below the free surface.

Finally, Lozano and Miguez [46] derived an expression for the number of layers h as a function of time for a situation with faster deposition rate, thus, considering also the possibility of a decrease in the number of layers (situation that is not possible to predict with Shimmin's model). Lozano's model reproduced oscillatory and steplike deposits obtained through different procedures:

$$h(t) = \frac{\phi v_e \beta l}{(1 - \epsilon)(1 - \phi)V_s} \left[1 + e^{-\lambda t} \left(\frac{\lambda}{\nu} \sin(\mu t) - \cos(\mu t) \right) \right]^{-1} + \frac{\phi}{(1 - \epsilon)} (v_e - v_s)t \quad (1.32)$$

Here, $(1 - \epsilon)$ is the deposit density. The model includes five free parameters to be extracted from the fitting to experimental data: initial time t_0 , initial position of the meniscus R_0 , the sedimentation velocity at large times V_s and, the coefficient for the extinction and period of fluctuations, λ and μ respectively. From the fitting of this model, to experimental data, they conclude that thicker deposits grow at lower velocities. The experiments used for validation of these model where done at a lower temperature and they registered growth velocities two order of magnitude smaller than in our case.

Chapter 2

Experimental Setup

Our approach to the problem of colloidal crystal formation through vertical deposition requires to visually access the contact line (i.e. the region where the transition from the fluid suspension to the solid colloidal structure takes place). Additionally, we look for an easy and robust assembly of the components of the experimental setup. The design should restrict the evaporation to a small region which remains constant during the experiment. Also, it should allow us to apply a homogeneous electric field to the suspension. With these points in consideration we construct the cell shown in Figure 2.1. Its main characteristics are:

1. *geometry*: a reduced size that allows easy accessibility. Most of the volume resides in a main body of inert Teflon® (Figure 2.1, in black) that support the other elements of the cell (Figure 2.1, in colour),
2. *substrates*: rectangular standard glasses ($17 \times 18 \times 1$ mm³, in cyan in Figure 2.1) are kept parallel by three 1 mm thick ceramic spacers located as shown in Figure 2.1 (in orange). They are coated over one face with a 150 nm layer of Indium Tin Oxide (ITO),
3. *leakproof*: two rubber elements in the front and rear part (Figure 2.1 in blue) are compressed by a metallic frame (Figure 2.1 in green) that seals the assembly and makes the ensemble robust.

The conductive side of the substrates faces inward, therefore resembling a parallel plate capacitor. This arrangement posses the following advantages:

1. optimal homogeneity of the applied electric field to the suspension,
2. visual access to the central area of the contact line during the whole process,
3. mass exchange with the environment mainly takes place between the substrates (on an area of about 17 mm²),
4. only a small volume of suspension is required (typically ~ 200 μL),
5. low light intensity needed. The incidence of the light source is done from the rear part of the cell and it is transmitted through the suspension to the central region of the substrates,
6. possibility of accessing different length scales by changing the external optic setup.

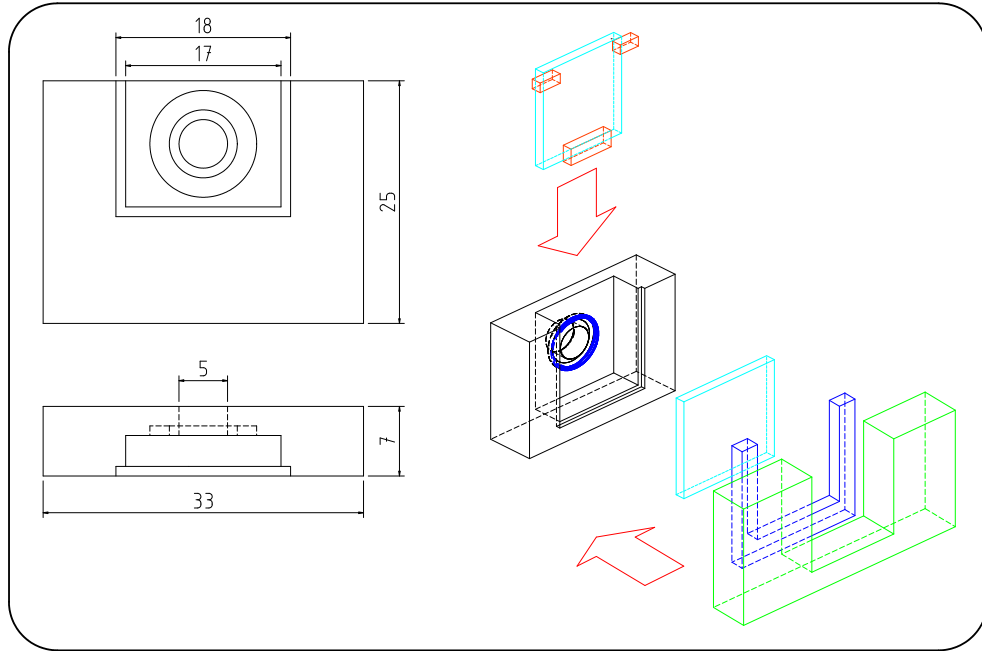


Figure 2.1: Orthogonal projected view of the main body (left) and isometric exploded view of cell setup (right). The different components of the cell and materials are colour coded as follows: main body (Teflon®, black), substrates (ITO and SiO₂, cyan), seals (rubber, blue), spacers (ceramic, orange), compressing frame (aluminium, green)

The setup distribution is shown in Figure 2.2. We project the moving contact line, through two first surface plane mirrors, on a ground glass screen placed outside a chamber where the temperature is controlled. The image is digitised with a monochrome CMOS camera (Pixelink PL-A741, 1.3 Mpx). A bundle of optic fibres incident through the back of the cell, provides illumination, through a cold light source (150 W halogen lamp, MOTIC MLC-150C). A single lens images the area of interest. This area is restricted, by the optical setup, to a circular region of about 5 mm of diameter centred at the front substrate. In each experiment, the cell is moved by a computer controlled linear actuator (resolution 8 μm) to the focal point of the lens.

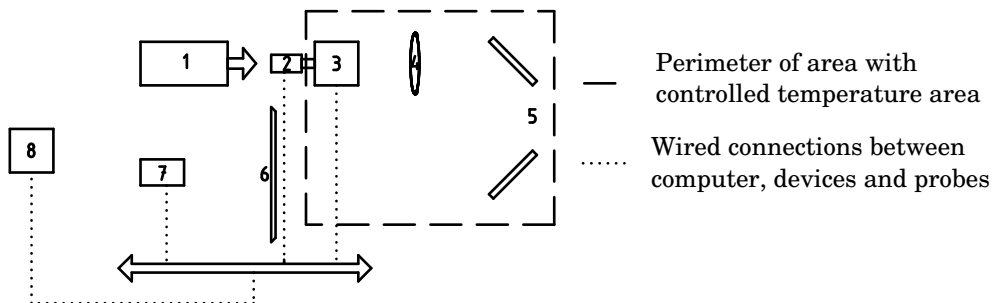


Figure 2.2: Schematic diagram of the vertical deposition experiment, 1- Cold light source, 2- Linear translator, 3- Cell, 4- Lens, 5- Mirrors, 6- Screen, 7-CMOS Camera, 8- Computer.

In Figure 2.3, we show a typical temporal record of the environmental parameters monitored during the experiments. Temperature was controlled at 63 °C. It was independently monitored

by thermocouples inside and outside the suspension. Average humidity was monitored during the experiment with a thermo-hygrometer (lower limit of calibrated region 2 %RH). The recorded steady state of humidity was below the lower limit for all experiments. If an electric field was applied, we additionally monitored the electrical current circulating through the suspension (Figure 2.3, inset).

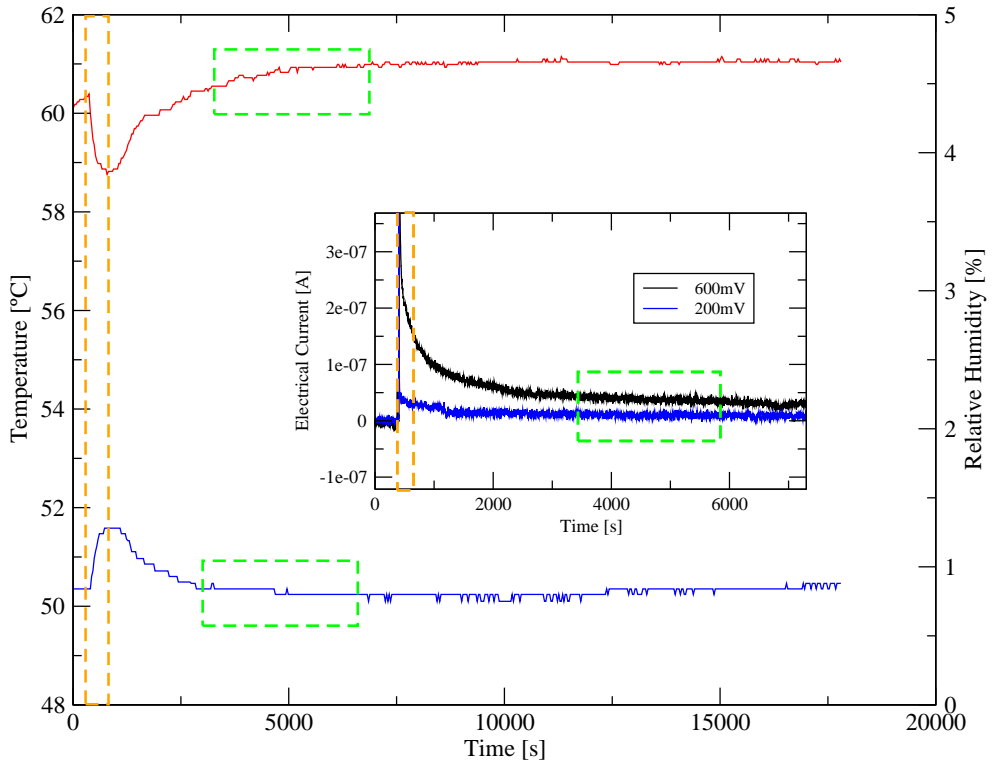


Figure 2.3: Typical evolution of temperature, humidity and electrical current (inset) during transient dynamics until they reach a stationary state. Orange lines mark the time at which the suspension is inserted. Green rectangles show approximately the measuring period for the contact line dynamics.

In orange, Figure 2.3, we mark the approximate time at which the suspension was inserted into the cell. Although while loading the cell, we perturbed the temperature and humidity, a steady state is almost reestablished by the time the measurements are taken (green rectangles).

In all the cases, we used electrostatically stabilised polystyrene spherical particles (diameter $d = 1.3 \mu\text{m}$, polydispersity index $\phi = 0.039$, surface charge $\sigma = -7 \mu\text{C}/\text{cm}^2$). They were obtained from Dr. Paulke (IAP, Germany) dialyzed and suspended in ultra-pure water at a concentration of 7.43% w/w. The suspension used in the experiments was prepared by dilution with ultra-pure water.

We clean the cell following a previously established procedure [92]. The cell components, except substrates, were cleaned prior each experiment with soap and, intense and consecutive rinsing of normal, distilled and ultra-pure water. We used new substrates for each experiment, which were cleaned in two steps: 15' in sonication (in acetone) and 30' in a hot bath (66 °C, in a

basic piranha solution, water:hydrogen peroxide:ammonium hydroxide - 5:1:1). Each component of the cell was dried with N₂ gas, and kept in a clean vial to minimise contamination. After this, we mounted the cell and placed it inside the chamber at 63 °C.

The piranha cleaning procedure activates the ITO surface giving a highly hydrophilic substrate. This is not the equilibrium state for the surface [93, 94], and it evolves increasing the hydrophobic character until equilibrium [95] is achieved. In our case, the contact angle of water drops placed on the substrate increased even two hours after the cleaning. We verified the effect of the wetting properties of the substrates by comparing two experiments, one carried out immediately after cleaning and, another done 24 h after. In the first case, we measured a characteristic speed of $3.1 \pm 0.2 \mu\text{m/s}$, while in the second, it was $0.68 \pm 0.03 \mu\text{m/s}$. Our interest was to have an initial contact angle as reproducible as possible, thus, for the following experiments we kept the substrate into the chamber for 24 h (at 63 °C) before inserting the suspension. This time period reduces heterogeneities in the initial hydrophilic state and, additionally, guarantees that the cell is thermalised at the working temperature.

We store the suspensions in a refrigerated environment (5 °C) to avoid agglomeration. Nevertheless, they still sediment. Therefore, prior their insertion into the cell, suspensions were treated through these steps:

1. sonication (5'): gives a redispersed suspension.
2. hot bath (3', 66 °C): thermalises the suspension at the working temperature.
3. bubbling of N₂ (1'): gas bubbles generated by previous steps are eliminated and N₂ displaces most of the dissolved CO₂ in the fluid phase.

Each experiment consisted on inserting 200 μL of suspension into the thermalised cell. This volume filled the cell up to a few millimetres above the observable area. Generally, the initial shape of the contact line was convex with a maximum in the centre of the substrates, resembling a saddle point (see Figure 2.4(a)). This shape evolves, above the observable area, to an equilibrium flat profile (in the central region of the cell) similar to the sketched in Figure 2.4(b). Thus, the acquired images have a relatively flat contact line. The acquisition rate was of about 3 frames per second at a resolution of 640 px × 480 px. Images were captured as long as the contact angle was visible.

Detection of the contact line position

In all the images obtained from the experiment, three regions can be identified. Figure 2.5 (left) shows the central region for a typical image together with a sketch of the lateral view. From top to bottom the regions are:

1. *Deposited structure.* Mostly a dark area composed of deposited particles. Usually this region of the image presents a heterogeneous distribution of intensity. Near the meniscus, the structure is wet due to the precursor film left by the receding fluid. Far from the meniscus the deposit is completely dried.

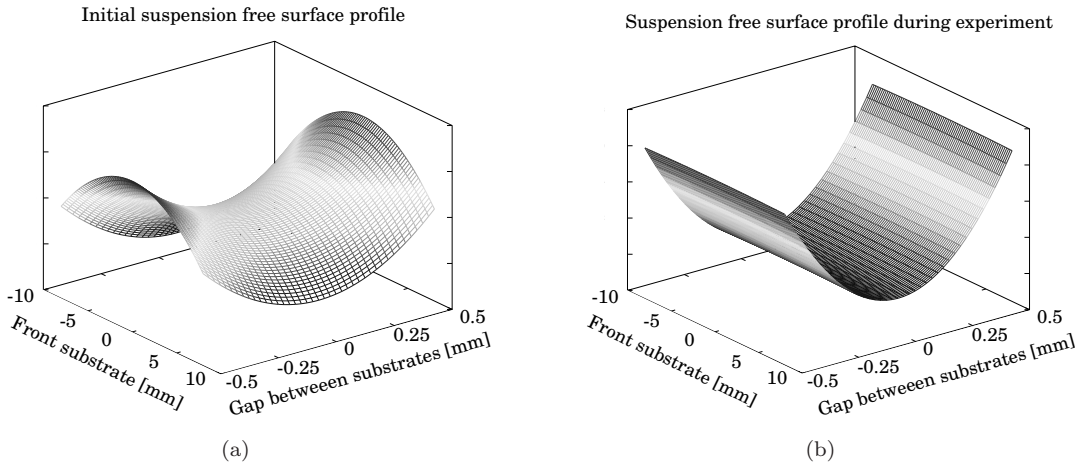


Figure 2.4: Sketch of the suspension free surface. (a) Initial profile after loading the cell. (b) Stable profile during the measurement period. Vertical axis is in arbitrary units.

2. *Meniscus and contact line.* A bright region split the field of view in two areas. The intensity is maximum in the upper part (contact line) and monotonously decreases towards the bottom (widening of the meniscus).
3. *Bulk suspension.* Mostly an area of homogeneous intensity, generally dark. The intensity decreases smoothly towards a minimum at the bottom of the image.

At very low concentrations, 0.04% and below, this generic picture changed. In this case, the darker area of the image locates in the meniscus while the upper and lower regions are lighter. This situation is characterised by leaving nearly no deposit on the substrate. Therefore, further studies were not carried out.

In the following, we will use a coordinate system on which each point of the image is localised by its x (horizontal) and y (vertical) coordinates as shown in Figure 2.5. The position of the contact line will be given by the y component. In the data analysis, we restricted the images used to a subset of around 1 image from every 30 acquired. Thus, we will measured the position of the contact line approximately every 10s. In the image shown in Figure 2.5 left, we found a bright area in the dried structure. This region is more intense than the contact line, as it is confirmed in the grey level plotted in the right. This makes the detection of the desired peak more difficult. It is inappropriate to simply consider the position as the maximum of intensity for each x position on the image. To simplify the discussion, in the following we restrict our analysis to one generic x position on a typical image. Later on, carrying out the same analysis through the complete set of data (all x positions and for all frames) we reconstruct the contact line position along time.

To avoid the detection of a high intensity region in the deposited structure, instead of the contact line, we use the fact that the bulk is always dark and highly homogeneous. We calculate the slopes of the lines that join each point of the grey level with the last point of the profile (as the green and red dashed lines in Figure 2.5 right). This calculation increases the intensity difference between peaks in the dried region, and the contact line (see \mathbf{d} and \mathbf{D} in Figure 2.5 right). In the example presented here, the deposited structure was \mathbf{d} more intense than the contact line, after the calculation, the contact line is \mathbf{D} more intense than the structure. Thus,

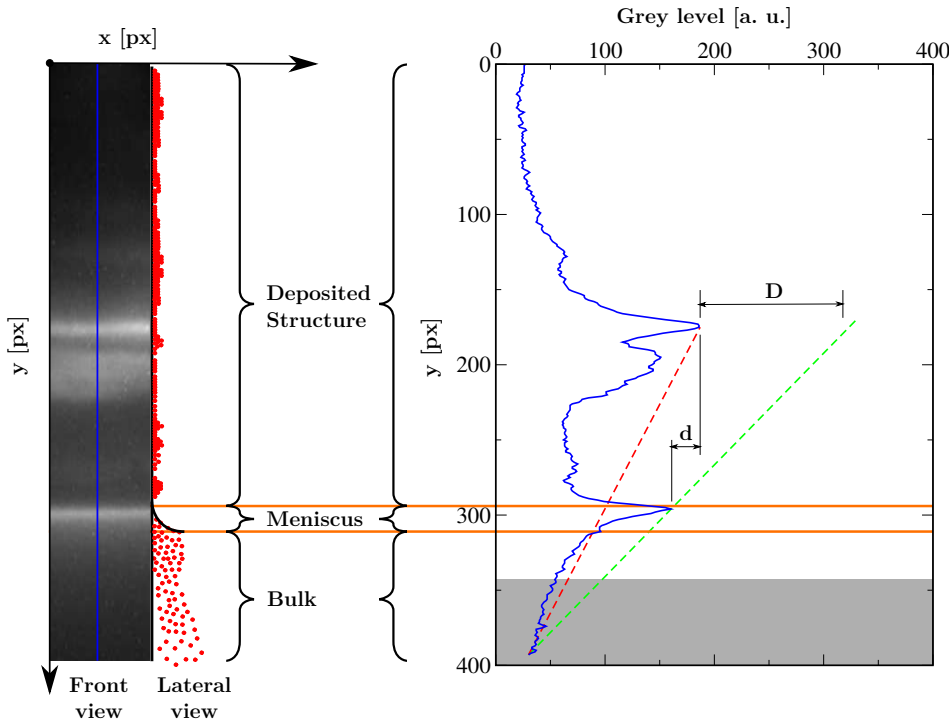


Figure 2.5: Contact line raw data and position identification. Left: Central portion of a typical frame and a sketch of the lateral profile. At the top there is the heterogeneous dried region and at the bottom the bulk suspension. Right: grey level for the horizontal position highlighted in the left image (in blue). Red and green dashed lines denotes examples of the slopes computed to identify the y coordinate of the contact line a that particular x position (d and D are the distance between the two main maxima before and after the calculation). Grey area is a disregarded zone where the maximum was not searched for.

we selected the y -coordinate at which the slope is maximum, as the contact line position. This procedure reduces the probability of error, that will occur, only, if a peak is on the right of the green dashed line (see Figure 2.5 right). This could happen, specially at early times when the contact line is near $y=0$, where the slope is minimum. But, at those times, a small region of deposited structure is visible and, therefore, we have very little heterogeneity on the image. As time evolves, more structure is deposited and heterogeneity increases. Nevertheless, the slope that we compute becomes larger and the program distinguishes the peak in the contact line from the ones in the deposited structure.

A drawback of this calculation is that it increases small heterogeneities near the reference point (at the bottom of Figure 2.5 right). Hence, the program is restricted to images on which one of the sides of the high intensity peak is highly homogeneous. In our case, there is noise in the bulk that is amplified by the calculations. This could interfere with the detection of the contact line, thus we do not search for a maximum in the last 50 pixels of the grey level. This correspond with the grey shaded area in Figure 2.5 right.

Finally, the calculation might give a wrong result if, for any reason, a region of high intensity is close to the contact line (for example, due to the presence of an impurity). This is occasionally observed but, it gives a position that is fixed at the high intensity peak until the contact line

is far enough. Therefore, the detected line appears to be stationary and can be filtered out by considering only non-zero speeds as we do later on.

A typical line obtained from these calculations is drawn in Figure 2.6 (highlighted in blue). It has been overlaid to a portion of the original image to ease comparison. The computed line presents several discontinuities that come from the noise on the image and the discrete nature of the measure. Hence, to obtain a smoother contact line we perform a 6-pixels length running average, after which the line become like the one highlighted in green (Figure 2.6 right). This smooth data is the one used in further analysis.

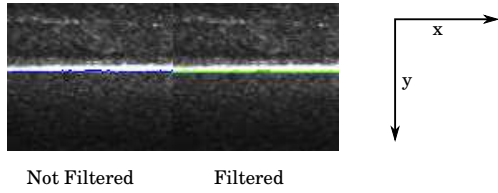


Figure 2.6: Left: Contact line (blue) as detected by the algorithm depicted on figure 2.5. Right: The smoother contact line (green) produced by a running average of 6 pixels.

From this calculation we generate a matrix, each element of which, is the y position of the contact line at each time and for each x position (represented by the rows and columns of the matrix, respectively). In Figure 2.7, we show an example of such matrix which is used in the following to calculate the speed of the contact line.

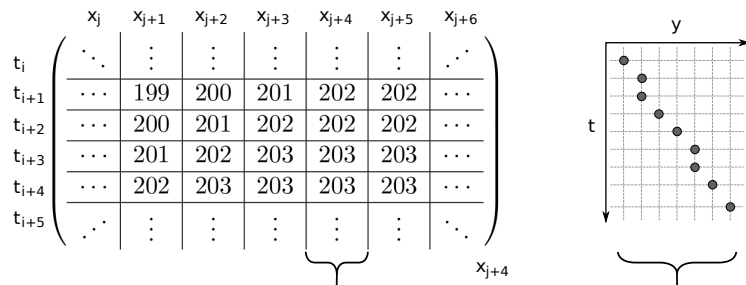


Figure 2.7: Left: Example of a matrix which stores the position of the contact line (y coordinate) for each time (t_i) and horizontal position of the image (x_j) of the image. Right: sketch of the graphical representation of a typical column of the matrix.

Throughout the calculation, our system of coordinates follows the convention for images (origin on top left of the image and positive axis to right and bottom, respectively). Thus, the position of the contact line will increase as the fluid phase evaporates, i.e. as the contact line displaces downward. Figure 2.8 shows the temporal evolution of the contact line for a fixed x position. The discretisation of the measure can be clearly observed in the insets (a, b), i.e., we can detect advancement or receding in no less than one pixel ($\sim 8 \mu m$ in this case). The predominant tendency of the position to increase is occasionally broken by a sudden retreat of the contact line (see inset b). This is a very rapid process that, we think, is related to the relocation of suspension after a pinning-depinning event taking place outside the visible region (either at the back substrate or at the edges of the cell).

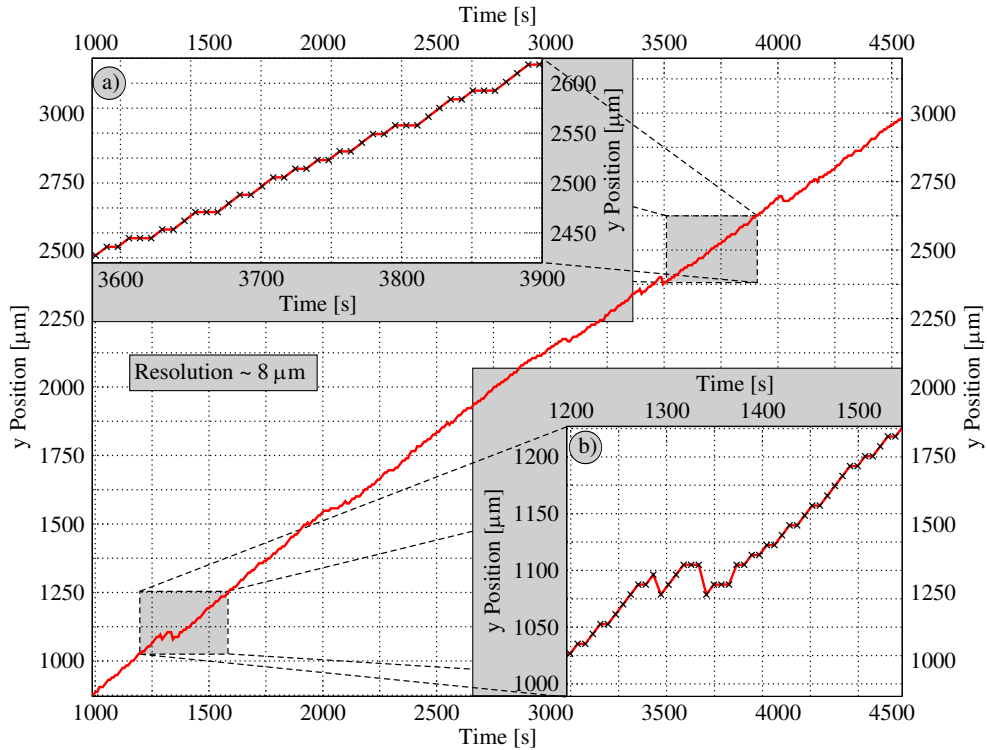


Figure 2.8: Position of the contact line as a function of time for one particular horizontal location (x in figure 2.5). Zoomed regions in the insets show the discretisation of the data (a) and an atypical event of retreat of the contact line (b).

2.1. Measurements of velocities

Our first aim in the study of the velocities of the contact line is to construct histograms to represent their distribution. To do this, first it is necessary to extract the slope of the y position data as plotted in Figure 2.8. We will obtain the velocity by identifying which slope correspond with a particular sequence of points (like in Figure 2.7). In order to do this, we first need to decide the timescale that we want to focus on. This timescale is determined by the number of points considered in the sequence. In order to maximise the retrieved information we want to consider a proper timescale. If it is too short the velocity will be dominated by the discretisation and, if it is too long, we will not resolve the local variations from a global mean velocity.

To explore how much we can extend on the time scale we calculated speeds using 5 and 11 consecutive points. For simplification, we consider points separated, in the vertical direction, a unit or zero distance (in pixels) from each other. Although this may be considered as a limitation, the contact line only moves in more than one unit near a retreat event on which we will not focus. Therefore, the velocities will be constrained to slopes from 0° to 45° that, then, need to be scaled to real units: $\mu\text{m}/\text{s}$. For each temporal scale, we will study their distribution by building a histogram.

The construction of these histograms is not a trivial task due to the discretisation of the data (recall insets in Figure 2.8). This discretisation gives discrete velocities which, additionally, are unevenly distributed in the velocity space. To understand this, consider a continuous line that

has been discretised. We want to obtain for each slope a set of points that represents it. Then, we discretised the line to the closest point on a unit square grid as in Figure 2.7. In Figure 2.9, we show a line which has been discretised according to the grid drawn. We start with an horizontal line and, then, slowly increase the slope. The first sequence is a set of horizontally aligned points. As the slope increases the point sequence remain unchanged until furthest edge of the line displaces 0.5 units in the vertical direction. Hence, for an interval of 0.1 rad ($\Delta y=0.5$, $t=5$) the same sequence is obtained.

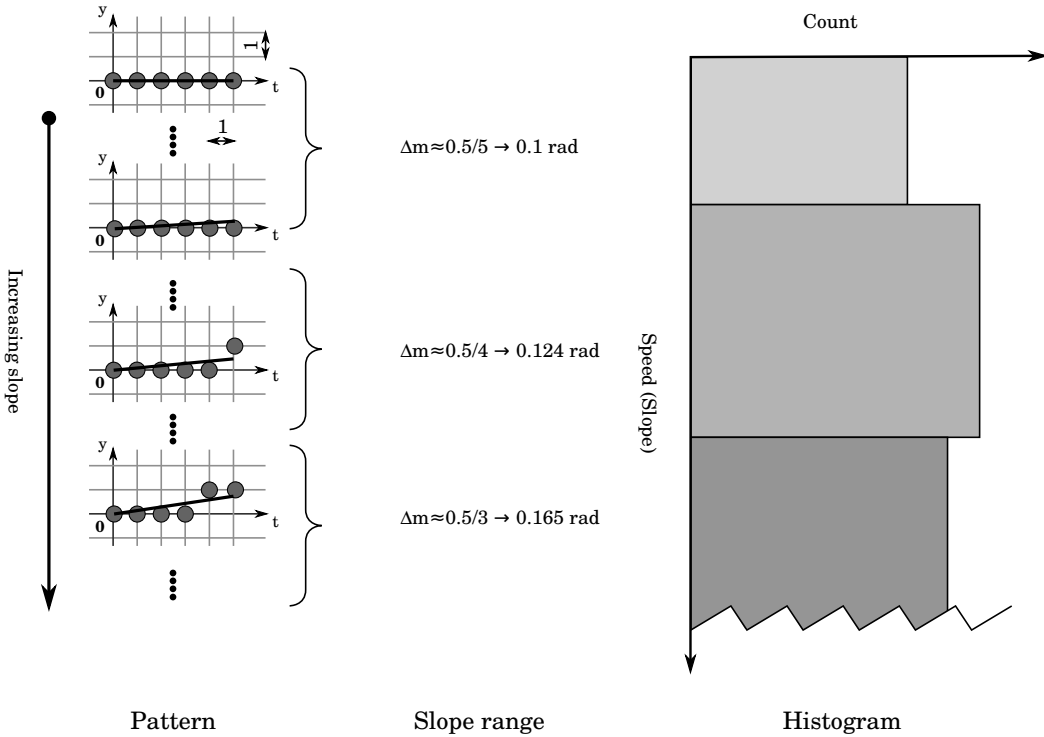


Figure 2.9: Sketch depicting the process used to determine the velocity intervals related to each sequence. Left: a slope is slowly increased and discretised to the points defined by the grey grid. Middle: when the pattern changes, a new interval Δm is created. Right: these intervals define the bins used to build a histogram.

Further increase of the slope gives a new change in the sequence when the second furthest point displaces 0.5 units, this new sequence will be reproduced for 0.124 rad ($\Delta y=0.5$, $t=4$). We assign, to this sequence, a different bin on the histogram. Following the same procedure, we see that a slightly different interval is associated to every sequence.

The sequences become more complex as we increase the angle and the number of considered points. Therefore, we calculate these intervals numerically through the following procedure:

Step 1 *Slopes*: we create an array of real numbers representing the increasing slopes covering from -0.5 to 1.5 in steps of 0.0001,¹

Step 2 *Discretisation*: the slopes are discretised in a sequence of 5 or 11 points,

Step 3 *Allocation*: all the slopes that give the same pattern are represented by the same interval (bin).

From this calculations, we get a set of intervals (bins) from which we build the histograms. Each bin has associated only one sequence. Our objective was to extract the velocity from the temporal sequence of the position of the contact line. To measure these velocities, we extract the sequences from the matrix of the contact line position (recall Figure 2.7). We took ensembles at the different temporal scales (5 and 11) and compare them with the ones obtained from calculations (step 2). When the two sequences coincide (the experimentally measured and the numerically computed), we assign to the corresponding position in the matrix, the mean value of the associated bin (obtained from step 3). As mentioned previously, zero velocities were not considered in the analysis.

Also, we do not consider those cases where distance between consecutive points is larger than one unit. This events occur very rarely or near a receding event (see Figure 2.8), therefore, this restriction is not statistically relevant. This calculation does not take into account sequences that do not correspond to a straight line in the time interval considered. Two of these particular cases are sketched in Figure 2.10. Here, each point sequence present two characteristic velocities at shorter timescales (t_s) than the one considered (t_l).

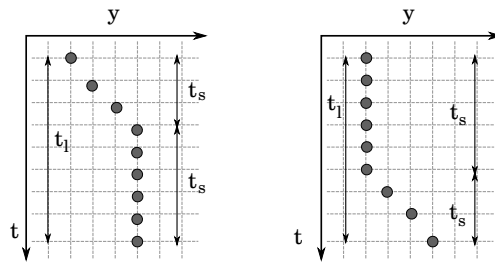


Figure 2.10: Two sequences for extreme situations not considered by the calculation velocities. These are situation where the velocity is not constant in the time scale considered.

In this way, the use of different number of points to calculate the velocity of the contact line leads not only to choose a particular time scale but, also, a specific set of bins for the statistical representation (number and size distribution). If short temporal scales are considered (5 points ~ 50 s, Figure 2.11(a)), we find that the velocities group in a small number of bins. This makes difficult to distinguish the characteristics of the distribution. For larger time scales (11 points ~ 100 s, Figure 2.11(b)), the general distribution is similar but, we observe an increased in the detail of its internal structure.

The probability density function plots showed that the measures present a significant noise that makes difficult to clearly identify characteristic velocities directly from these histograms. Therefore, we computed the probability distribution to reduce the effect of the noise. In figure 2.12(a), we show the probability distribution for 5 point sequences (empty circles). Only one function (black line) can be fitted reasonably due to the few points available. When larger temporal scales were taken (figure 2.12(b)) the distribution require the sum of three Gaussian distribution functions (plotted in red, green and blue) to obtain a proper fit (black line). These fittings were performed in R statistical computing language.

¹The restriction to a variation of distance between consecutive points of unity or zero (a.u.) means that the slopes will be restricted to the interval $[0,1]$ ($[0^\circ, 45^\circ]$). The extended interval that we use is to be certain to guarantee all possible configurations.

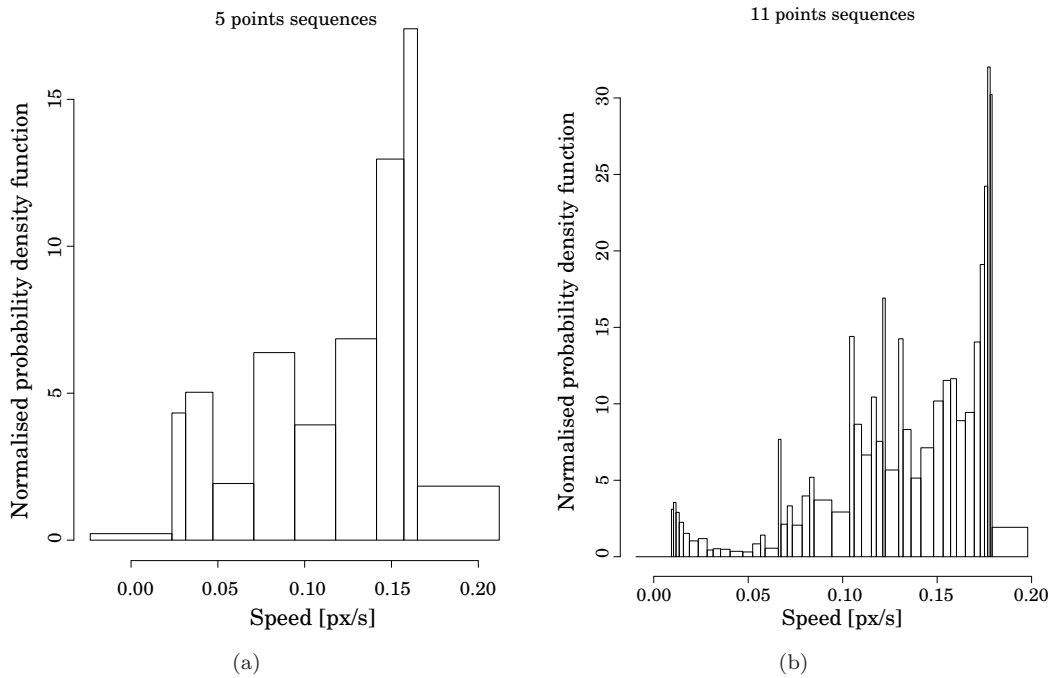


Figure 2.11: Histograms of velocities obtained with sequence of 5 (a) and 11 (b) consecutive points

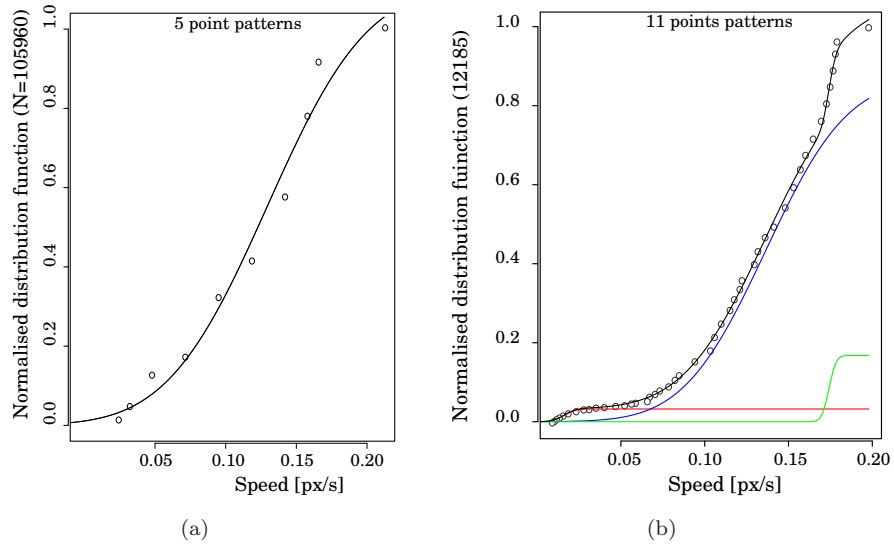


Figure 2.12: Cumulative histograms of velocities obtained with sequences of 5 (a) and 11 (b) consecutive points. Global fit with Gaussian distributions functions are shown, Left: one Gaussian fit; Right: one fitting function (black) composed by the sum of three individual Gaussian functions (shown in colour).

From this analysis, we choose to continue using 11 point sequences for further studies since they provides a large internal detail and still recovers the main characteristics of the shorter timescales distribution.

We also tried a traditional approach using equispaced bins but, we found results that depended

strongly on the size of the bin used. The shape of the distribution changed with the number of bins, making impossible to perform a correct analysis. This occurred because we created bins where no velocity were measured. The absence of those velocities was due to the discretisation of the data and not a physical reality of the system. Thus, we needed to calculate the bins (mean value and width) to be able to properly construct and interpret the histograms.

We attempt to overcome the problem of discretisation by a sub-pixel determination of the contact line position. For this, we fitted a Gaussian function to the maximum detected as in Figure 2.5 and calculate the centroid of the fitted function. Nevertheless, the discretisation remained and there was not any qualitative improvement on the histograms, which still needed to be treated as described before (Figure 2.12).

Summarising, for each Gaussian distribution that is fitted we designate a characteristic velocity. The mean of the fitted distribution is the velocity reported value, and the error of the fitting is the reported error. The dispersion of the Gaussian distribution represents the degree of influence of the different random phenomena (thermal and humidity fluctuations, substrate heterogeneity and presence of impurities) on the corresponding characteristic velocity.

2.2. Evolution of velocities

Recall the matrix where we stored the data extracted from the images of the contact line (Figure 2.7). From it, we extracted the different velocities but, also, we store the time and position at which those velocities were measured. Thus, we further extended the study of the velocities through the analysis of their evolution. For this, we took the mean value of all non-zero velocities as the velocity at a particular time. The error was taken to be one standard deviation. In Figure 2.13 we show the typical behaviour observed at low concentration (0.1 %).

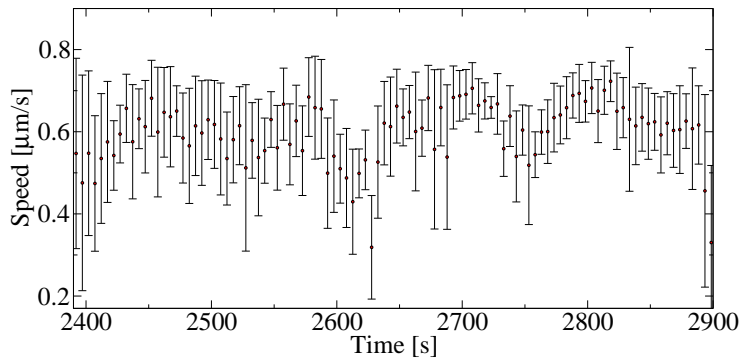


Figure 2.13: Typical temporal evolution for a 0.1% concentration experiment. While characteristic distributions show one maximum, the temporal evolution shows that there are different mean speeds with very similar values.

It is necessary to draw a distinction between the characteristic velocities and the velocity used here in the temporal evolution. We used the same raw data in both cases but, the number of velocities available to calculate each point for the evolution graphs are much smaller than the ones for the characteristic velocities (on the order of 100 and 100000, respectively). Therefore, the effect of the fluctuations is more evident and is not possible to carry out the former analysis for

each specific time. Thus, we chose to represent this data as the mean value and their dispersion. In this way, a large error indicates that the fluctuation were more relevant at that time. Also, is important to remark that we are considering velocities located on different position of the contact line. Hence, at a particular time, a part of the contact line can be affected by a fluctuation (e.g. a defect on the substrate) while other region can remain almost unperturbed. In chapter 4 we will explain in more detail the considerations that need to be taken in order to correctly interpret these evolution plots.

2.3. Scaling factors

Finally, we obtained the velocities in physical units. For this, we compared images taken after drying (in a standard optical microscope) with *in-situ* images taken after the fluid phase had completely evaporated. We used the diameter of the particles as reference to calculate the scaling parameter (from px to μm). The procedure of comparison is sketched in Figure 2.14. A composition of 50X optical images is scaled until its main central features overlaps to the ones on the *in-situ* image (Figure 2.14 a and b). Then, we average the distance between several points of this rescaled 50X image and the same image at the original scale. This gives a first scaling parameter from *in-situ* scale to the 50X one (Figure 2.14 a or b, to c). Similarly, average distance between points on common areas at different magnifications gives a factor of scale for 50X to 100X (Figure 2.14 c to d) and 100X to 400X (Figure 2.14 d to e). Finally, in 400X images we measure the distance between spheres and compare it to its diameter ($1.3 \mu\text{m}$). The successive multiplication of these factors gave the final scaling parameter from the *in-situ* to the real length scales (in μm per px). To ease the location of the area observed *in-situ*, when working with the optical microscope, we marked the external face of the front substrate (shown in green in Figure 2.14).

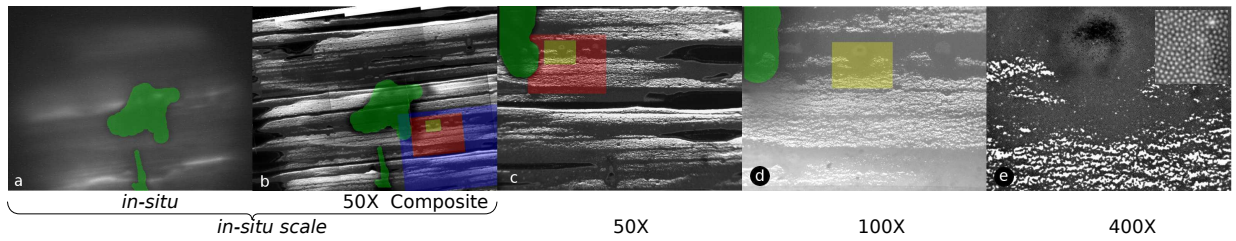


Figure 2.14: Calculation of scaling factors for *in-situ* images. **a:** *in-situ* image with the reference mark (green); **b:** 50X composite scaled to match *in-situ* scale (reference mark in green); **c:** 50X image at original scale (correspond to blue square in **b**); **d:** 100X image of the red area highlighted in **b** and **c**; **e:** 400X image of yellow area in **b**, **c** and **d**. At 400X scale individual particles are clearly identified (see inset in **e**)

In table 2.1, the scaling factor for each experiment is presented. Only the factor between the *in-situ* (50X rescaled) and the 50X (original scale) images changes from experiment to experiment. The other images used for the scaling (50X, 100X and 400X) are always taken with the same optical arrangement (established by the microscope) and, therefore, related by the same scaling factors.

Measure	Scaling parameter $\mu\text{m}/\text{px}$
0V - 0.1%	8.7 ± 0.4
0.2V - 0.1%	10.0 ± 0.4
0.4V - 0.1%	8.8 ± 0.3
0V - 0.3%	5.5 ± 0.2
0.2V - 0.3%	8.9 ± 0.5
0.4V - 0.3%	9.4 ± 0.4
0.6V - 0.3%	10.8 ± 0.4
0V - 0.5%	8.4 ± 0.3
0.2V - 0.5%	7.0 ± 0.2
0.4V - 0.5%	8.5 ± 0.4
0.6V - 0.5%	6.6 ± 0.1
Dimensionless scaling factors (common to all measures)	
50X-100X	3.97 ± 0.02
100X-400X	2.50 ± 0.01
400X- μm	0.32 ± 0.02

Table 2.1: Scaling factors for each experiment calculated by multiplication of the three common factor to all measures (100X-400X, 50X-100X and 400X- μm) and the final scaling from 50X to the *in-situ* images scale. Common factors arose from scaling between objective on the microscope images.

Chapter 3

Results

We focused the vertical deposition experiments to explore the effects of two parameters: the concentration of the suspension, and the applied electric field. We varied the concentration between 0.1% and 0.5% w/w. This range, despite is small, gives rise to a great variety of structures, ranging from sparse submonolayer to multilayer deposits. In all the results reported here, we restrict to the findings on the front substrate where the positive electrode is connected. Hydrolysis of the suspension limited the magnitude of the electric fields to values from 0 to 0.6 V/mm. Fields of $1.2 \sim 1.5$ V/mm produced strong flows that distort the deposition process near the meniscus [92]. This is consistent with the electrolysis of water molecules that take place at around 1.23 V [97].

First, we will describe the different structures observed and their abundance in relation to the initial concentration of the suspension. Later, we will present the results regarding the characteristic velocities of the contact line. Finally, we will show the evolution of this velocity and macroscopic flows that appeared in the bulk of the suspension.

3.1. Deposited structures

The structure deposited over the substrates is highly heterogeneous. We observed from very sparse submonolayer to multilayer deposits. In this work, we will group the structures in four different categories. This classification implicitly takes into account the relationship between the movement of the contact line and the presence of particles in its neighbourhood. This relation, and its role in the formation of these structures, will be explained in detail in the next chapter.

- *Non-compact deposit (NC)*. This is a submonolayer structure characterised by a very sparse distribution of particles. They arranged mainly in short chains (a few particle diameters length) oriented parallel to the contact line (Figure 3.1(a)).
- *Non-compact dense deposit (NCD)*. Also a submonolayer structure, the particles arranged in closed packed bands one monolayer thick and a few particle diameters wide. They are interconnected through small vertical clusters or chains (highlighted in Figure 3.1(b)). The bands are mainly oriented parallel to the contact line.
- *Compact monolayer (CM)*. This is a mostly close packed structure one layer thick, and, at least, several tens of particle diameters wide (see Figure 3.1(c)). Domains are small

(typically they expand less than 10 particle diameters on each direction). We did not observe any preferred orientation on the domains. A typical Fourier transform of these structures showed an homogeneous ring intensity pattern (inset in Figure 3.1(c)). The upper and lower boundaries of a **CM** region were, typically, parallel to the contact line.

- **Multilayer (ML).** Regions more than one layer thick appear as dark areas in the bright field optical microscope (see Figure 3.1(d) left). We do not have the instrumentation to measure the thickness of the structure, but using an in-line microscope setup we estimate that should be on the order of ten layers. Using this setup we can also estimate the structure of this multilayer that is typically very heterogeneous (see Figure 3.1(d) right). Multilayer arranged parallel to the contact line. Typically a structure with square symmetry precedes the transition from a monolayer to a multilayer as observed in similar experiments [98].

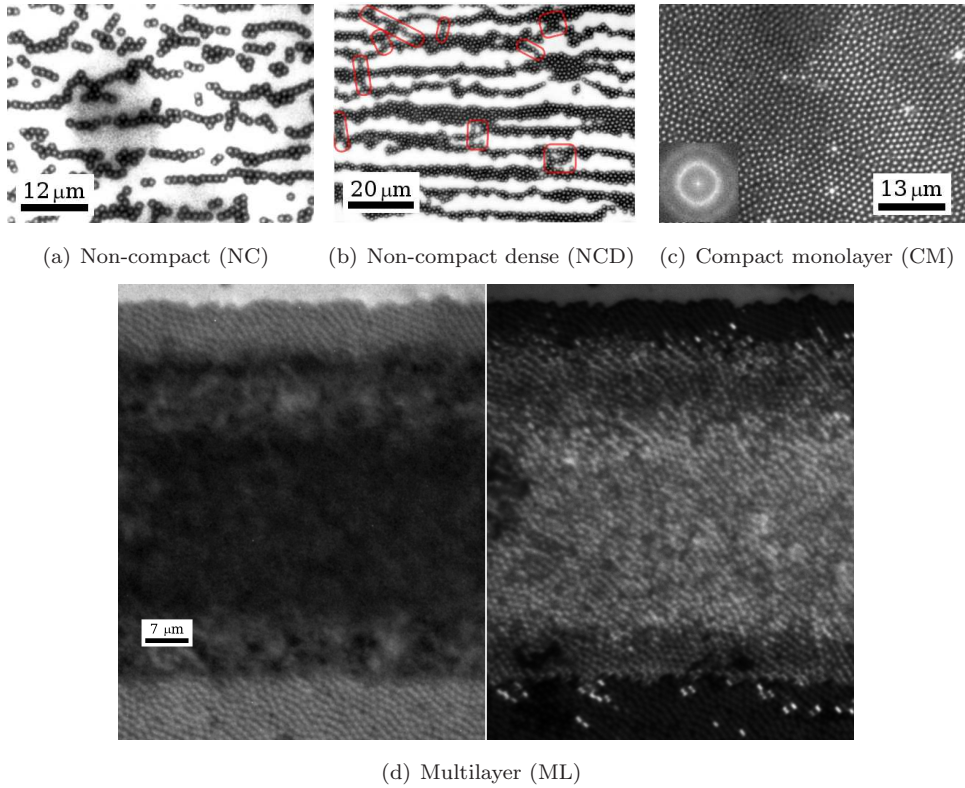


Figure 3.1: Microphotographs of the different structures observed over the substrate. (a) The less dense structure characterised by unconnected chain-like groups of particles. (b) Slightly denser structure of close-packed bands interconnected by vertical chains or small clusters (circled in red). (c) A close packed monolayer that expands over the substrate for several tens of particle diameters. Typical Fourier transform of these areas presented as a homogeneous ring (inset). (d) Multilayer structures appear as dark regions in a bright field microscope (left). With an in-line illumination setup the dark region reveals to be particles forming a heterogeneous structure (right).

In Figure 3.1(d) right, the multilayer area shows several regions with different intensities. Through focusing at different points we confirmed that this patches correspond to groups of particles at different heights. Thus, despite we do not have precise access to the three-dimensional

structure we estimate that the multilayer does not present a flat homogeneous thickness but a rough and heterogeneous top surface.

In certain situations, these structures formed a macroscopic columnar arrangement. Figure 3.2 shows two examples occurring at different concentrations (0.1 and 0.3%, respectively). In all our samples, these columns tend to widen (in the plane of the substrate) as the contact line moves. While the multilayer columns tend to finish abruptly (Figure 3.2(b)), the submonolayer columns (Figure 3.2(a)) reduce gradually until they disappear. Additionally, the columnar structure showed a striped pattern, parallel to the contact line. These stripes corresponded, in general, to transitions between different structures.

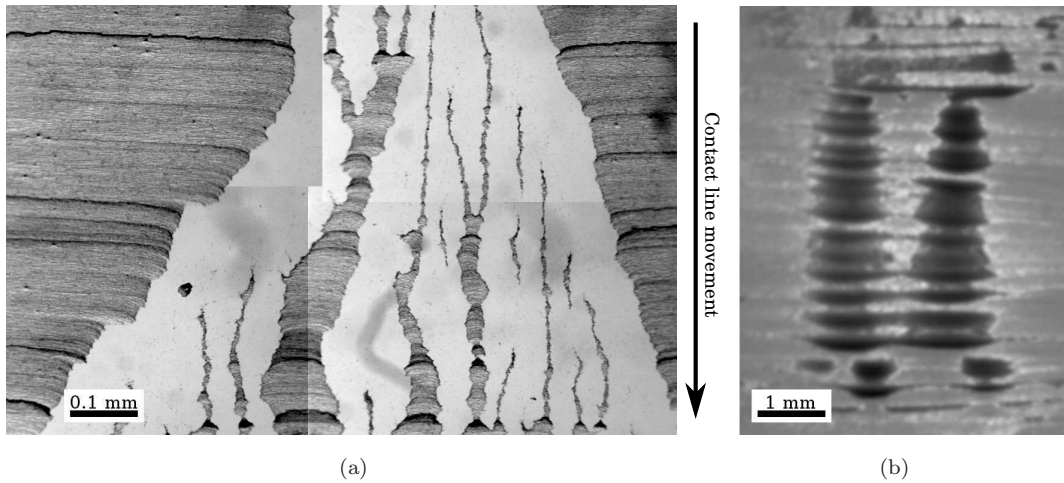


Figure 3.2: Columnar arrangement of structures. (a) At low concentration (0.1%) the **NC** structure brakes into several columns separated by areas without deposition. As the empty region widens, new branches of deposits are created. This image is a composite of 4 photographs, thus the different intensities observed. (b) A similar situation occurs at larger concentration where **ML** structure starts to grow in localised points from which columns develop.

We observed that, in the range of concentrations used, some structures were more common than others. At low concentration (0.1%), **NC** structures covered most of the surface. They were only interrupted by some thin monolayer bands or a columnar breaking, like the ones in Figure 3.2(a). This breaking turns less frequent as the electric fields increase, while the number of monolayer bands appears to increment. At 0.3%, we obtained a mixture of all the defined structures. Nevertheless, in most of the substrate we encountered the **NCD** type. The second most common structure was **ML**, the proportion of which, with respect to **NCD**, increased with the electric field. At 0.5%, we observed all types of structures, although **ML** appears as the dominant one. The increase in concentration and voltages, was accompanied with an increase in the heterogeneity of the structure deposited. While, at low concentration, the substrate appears to be covered mostly by the same structure, the larger the concentration and voltage are, the more heterogeneous the structure becomes. In Figure 3.3 we present a series of images of the central region of the substrates analysed, the images are arranged such that the applied voltage increased from left to right. The first row corresponds to 0.3% experiments. The second row are experiments made at 0.5%.

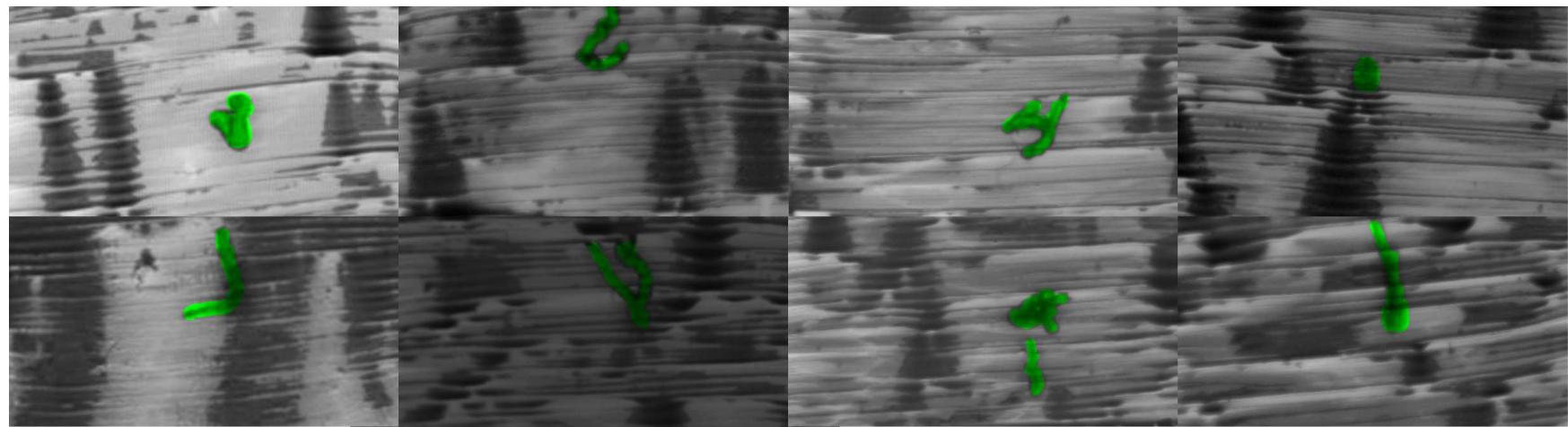


Figure 3.3: Sequence of macroscopic images of deposits encountered at increasing voltages. Top row 0.3%. Bottom row 0.5%. Columns are 0 , 0.2, 0.4 and 0.6 V/mm, from left to right. Highlighted in green are the reference marks made for localisation of the areas visualised during the experiment. The width of each image is of 11 mm.

A particularly interesting arrangement was found when the **NC** or **NCD** structure was deposited in the presence of constant electric fields. This structure is characterised for thin bands arranged parallel one to each other, and separated for an approximately constant distance. On figure 3.4(a), we show two regions that presented this structure. Each image, it is accompanied by a portion of its Fourier transform that clearly shows maxima associated to the banding. The left image correspond to a field of 0.2 V/mm and an initial concentration of 0.5%, in the right image the field was of 0.2 V/mm and the concentration was 0.3%. From the images is clear that the larger concentration case has a less dense structure. This is due to that the structure, deposited in a particular area, depends on the local concentration near the meniscus instead of on the initial one. This pattern of alternating stripes is similar to some situations observed in dip-coating experiments [99]. Also, we observed that this banding disappears for further increase of the field strength as it is shown in Figure 3.4(b).

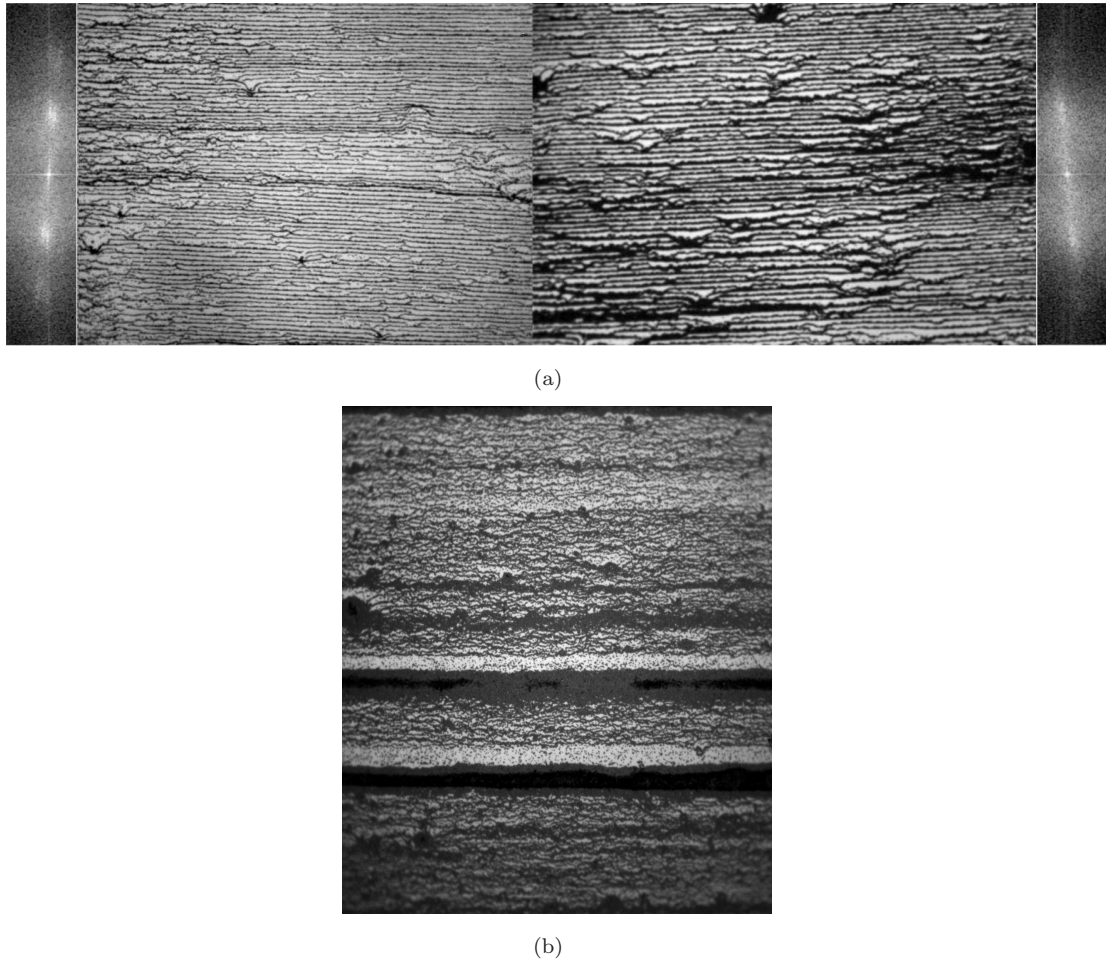


Figure 3.4: (a) Banding observed in some **NC** or **NCD** structures on experiments carried out at moderated electric fields. The Fourier transforms show that the distance between bands is roughly constant. These images corresponds to two experiments made at 0.2 V, the initial concentration of the suspension was 0.5% (left), and 0.3% (right). (b) Further increase of the electric field is accompanied with the disappearance of the banding. Image corresponds to an experiment at 0.6 V/mm and 0.3% of initial concentration.

3.2. Characteristic velocities

We already discussed in chapter 2 the issues that arose from having discretised measures. Now, we will introduce the characteristic velocities obtained at the different experimental conditions.

The first aspect we observed was that, when increasing the initial concentration, more than one characteristic velocity emerged. At the lowest concentration, the probability distributions typically were well fitted by one Gaussian distribution function which we associated to one characteristic velocity. At 0.3 and 0.5%, we measured two velocities. In Figure 3.5, we show an example of these two cases. On the left, the probability distribution for a typical 0.1% experiment (empty circles) is correctly fit with one Gaussian distribution function (red curve). On the right, we show a similar histogram when we used a larger initial concentration, here, two functions (red and blue) were needed to fit the experimental data (empty circles). The parameters of the fit for each Gaussian are colour coded in the top left of each plot.

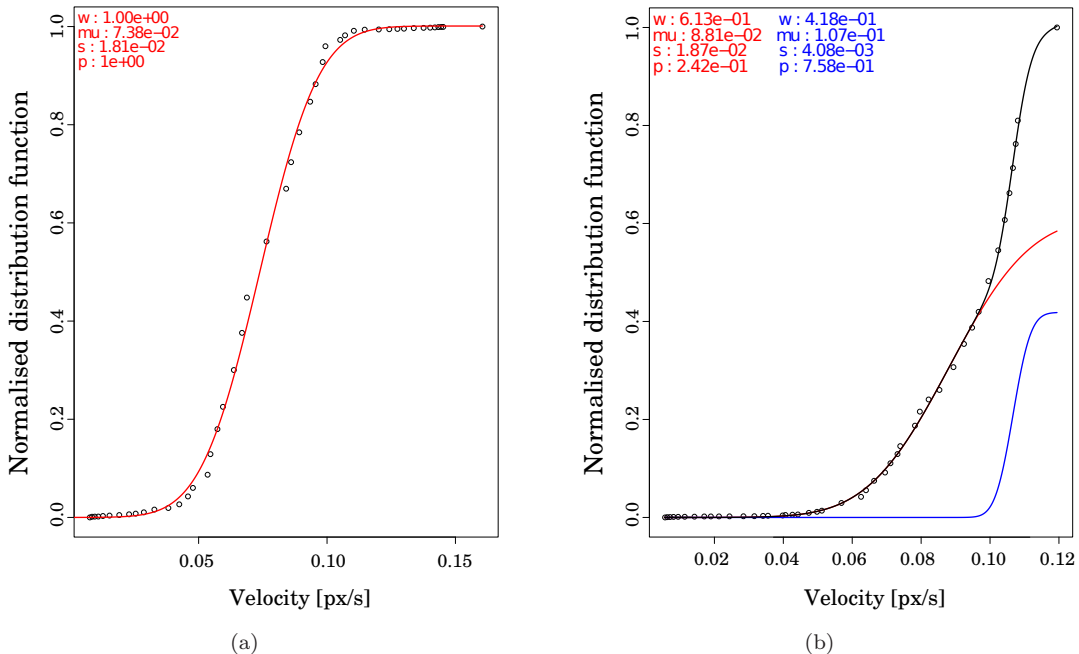


Figure 3.5: Typical probability distribution (empty circles) for the characteristic velocity determination. (a) Low concentration situation at which one well defined peak is fitted using a single Gaussian distribution function (red line). (b) At higher concentration experiments, we repeatedly observed a bimodal distribution, which was well fitted by the sum of two Gaussian distribution functions. We show in colour each individual function and in black the sum of them. At the top left of each plot we show, colour coded, the parameters for each fitted function: w - relative weight of the characteristic velocity, mu - characteristic velocity (mean of the Gaussian function), s - standard deviation, p - relative height of the probability density function.

Electric fields did not modify the number of characteristic velocities observed. Nevertheless, they did displace the position of the peaks, i.e. the mean velocities. In Figure 3.6, we summarised the results for each experimental condition. We used the same scale for the axis in all the graphs to ease comparison. A first interesting aspect of these results lay on the effect of the voltage,

with respect to the initial concentration, it seems to differ on each case. Indeed, in the figure we observe that, at low initial concentration, mean velocities do not show a significant change¹. On the contrary, at 0.3%, a low electric field strength (0.2 V/mm) shows an increase on both characteristic velocities. Larger applied fields appear ineffective. At 0.5%, the field affects different both velocities, the large one decrease while the small velocity increases slightly. For the extreme conditions of 0.5% and 0.6 V the low velocity peak showed a very extended distribution and its maximum coincide with the well defined high velocity peak.

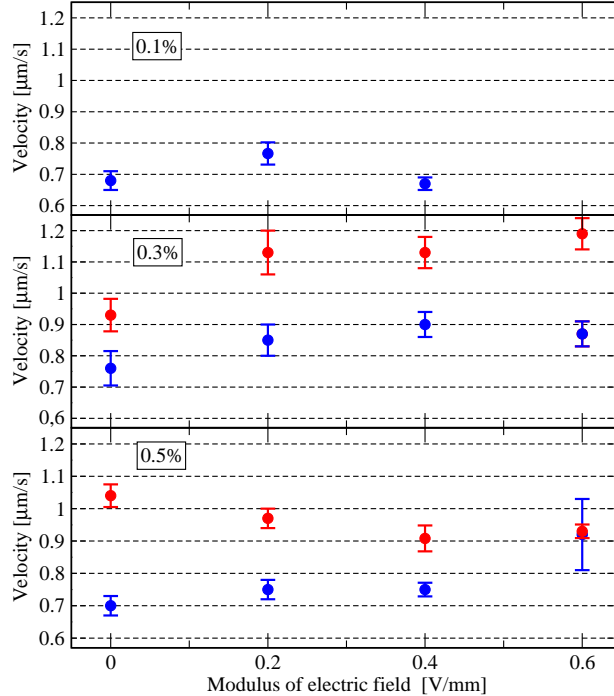


Figure 3.6: Characteristic velocities. The evolution of these velocities as a function of voltage and concentration can be appreciated. All axes have a common scale to ease comparison.

3.3. Evolution of the velocity of the contact line

We pursued a more detailed analysis of the velocities considering its temporal evolution. Throughout our image analysis, we store the position and velocity of the contact line for each point in the image. To study the evolution, we summarised the measured velocities, at a same time, through their mean and standard deviation. These are taken as the central value and the associated error, respectively. As done previously, we only consider the non-zero velocities. In Figure 3.7 we show the typical results for each concentration, without electric fields. The lowest concentration case, particularly differs from the other two. In this situation, the error bars are of the same order of magnitude than the displacement of the mean velocity (see Figure 3.7(a)). This is consistent with the single peak observed in the histograms plotted in Figure 3.5(a). At higher concentration, the error bars are considerable smaller than the mean velocity displacement. In

¹For the point at 0.2 V/mm, the program did not detect the contact line on much of the area of the substrate, thus the statistic is poorer than in the other cases. Typically, there were around 10^5 points identified per experiment.

Figure 3.7(b) and 3.7(c), we observe clear transitions in the mean velocity. If we compare to the histograms in Figure 3.6, we can see that the two peaks identified in the histograms correspond well to the situation of the contact line preferably visiting two different states. In the next chapter we will relate this temporal evolution to the structures that were deposited on the substrate.

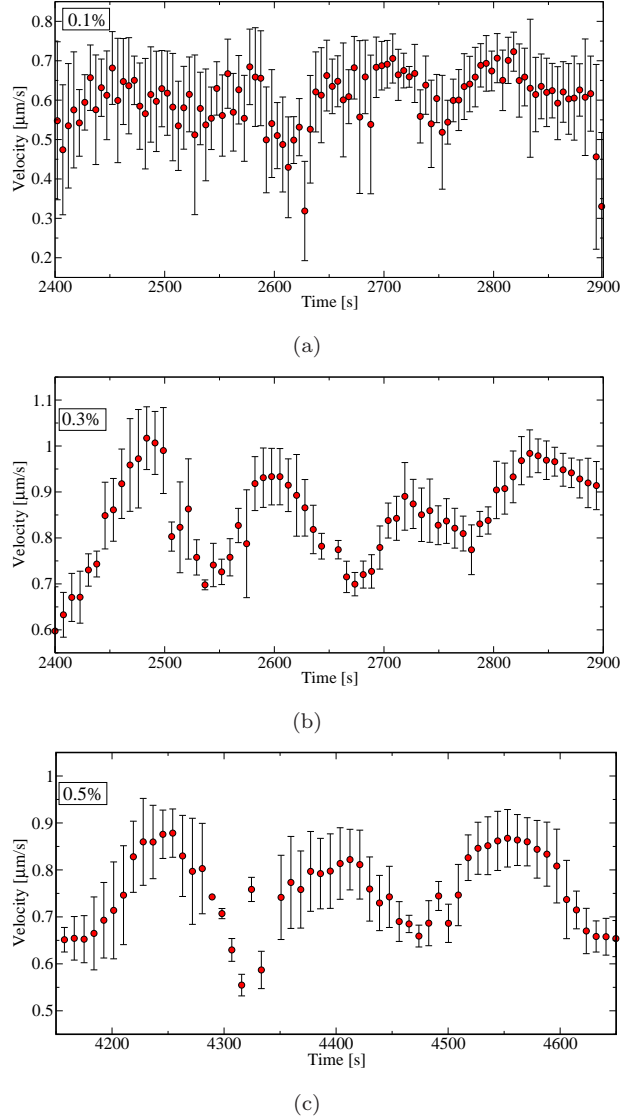


Figure 3.7: Temporal evolution for the non-zero velocity of the contact line. We plot the mean velocity and its standard deviation, which represent the central value and the error, respectively. Each graph correspond to a different initial concentration: (a) 0.1%, (b) 0.3%, (c) 0.5%

3.4. Bulk flows

Another point to address refers to a macroscopic flow observed in the bulk suspension. This flow, in contrast to the one that carries the particles towards the substrate, is observed at a macroscopic lengthscale. It resembles a convective flow that could be result of the cooling of the

fluid as it evaporates at the free surface. We had the best visualisation of this flow using a laser as light source. In Figure 3.8 we show a snapshot of an experiment where these flows were clearly observed (0.8 V/mm , 0.3%). We overlaid arrows that indicate the direction of the flow, and two curved lines that highlight where the transition between flow direction occurs (downward, light area in the centre, and upward, dark areas on the laterals). These flows were stronger at low concentration and high field experiments. Also, they were generally asymmetric with a larger curvature in one side of the cell than in the other. We did not observe a preference respect on which side the asymmetry appeared. To visualise these flows we needed to increase the intensity of the light. In this way, the contact line region was oversaturated and it was not possible to study, simultaneously, the velocity and this macroscopic flows. We concentrated our work on the contact line dynamics and qualitatively record the presence of these flows for future consideration.

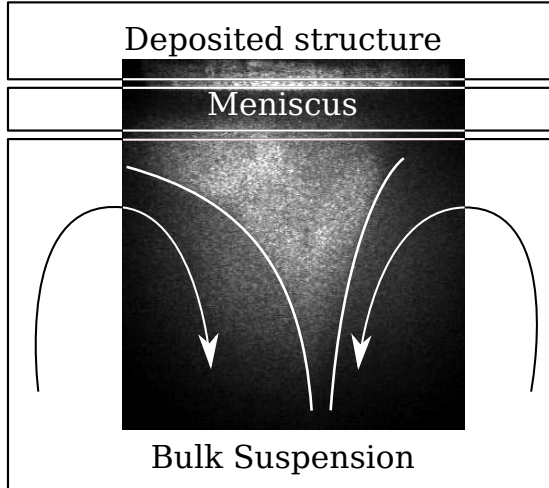


Figure 3.8: Sketch of the macroscopic flows observed during experiments. The laser light source used for this observation gives a speckle pattern that, in turn, results on a granular aspect of the image. Typically, these flows were stronger in experiments with low concentration and high field strength.

Chapter 4

Discussion

In chapter 3 we presented the results with respect to the velocities and to the structures that were observed on the system. In this chapter, we will discuss on how these two aspects interact together to give rise to the observed complex dynamics.

Typical parameters in our experiments were:

$$\begin{aligned}\rho &\approx \rho_{water} = 1 \text{ g/cm}^3 = 10^3 \text{ Kg/m}^3 \\ \mu &\approx \mathcal{O}(\mu_{water}) \approx 1 \text{ cP} = 10^{-3} \text{ Kg/(m s)} \\ \sigma &\approx 1 \times 10^{-1} \text{ N/m} \\ Re &= \frac{\rho V L}{\mu} \approx 10^{-6} \\ Ca &= \frac{\mu V}{\gamma} \approx 10^{-8}\end{aligned}$$

Density ρ was determined by weighting a known volume of suspension. We were not able to measure the viscosity but, due to the low concentration of our suspensions, we expect that it should be of the order of magnitude of the one of water [100]. We estimated the surface tension by the pendant drop method.

From the magnitude of the dimensionless numbers we infer that the particles approximately follow the fluid flows (small Reynolds number), and that the flows in the porous medium are dominated by capillary forces (small Capillary number).

First, we will go back to the temporal evolution introduced in section 3.3 (Figure 3.7). From the data retrieved in our experiment we have the position of the contact line at each time (recall Figure 2.5 or 2.8). This position is the y -coordinate on the *in-situ* images. Therefore we can locate at each time, the position of the contact line and the structure that was deposited. Although the *in-situ* images provide limited information of the structure deposited (due to their low resolution), in the scaling procedure (Figure 2.14 b) we were able to obtain high resolution images of the deposited structure. Recall that we associate the growth velocity of the structure to the velocity of the contact line. Thus, we can compare the velocity of growth with the type of deposited structure. Some care has to be taken to do this comparison. In general, the deposits are very heterogeneous. Thus, in many situations different structures have been form, simultaneously, at different positions of the meniscus. For the determination of the evolution of the velocities we considered all the velocities at a particular time as only one, through its mean and standard

deviation. Thus, when multiple structures have been formed simultaneously, at different velocities, the contact line will tend to deform until it breaks. This is conceptually similar to the movement of the contact line on a non ideal substrate [101]. This process is complex, and it is difficult to analyse the contribution of the different regions to the global movement of the contact line. Therefore, we restricted to regions where the structure deposited was similar along the contact line. Also, we will not consider positions where we detected a retreat of the contact line.

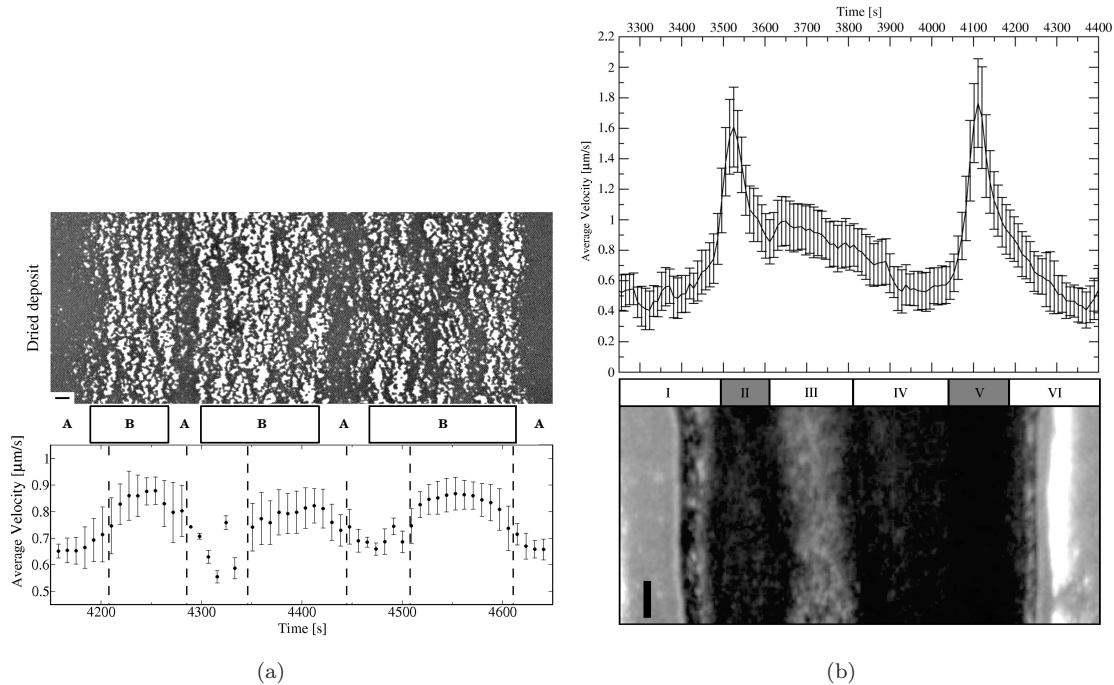


Figure 4.1: Comparison of the temporal evolution (calculated as detailed in section 2.2) with the deposited structure. Both sequences come from an experiment made at 0.5% and without electric field. (a) Top: alternating sequence of the **NCD** and **CM** structures deposited on the substrate. Bottom: the corresponding velocity evolution that illustrates a series of transition between two states. A and B bands indicate approximately the corresponding structures and velocities. Scale bar represents 13 μm (b) Top: velocity evolution which illustrates a complex sequence of velocity transitions. Bottom: the corresponding deposited structure. The different regions correspond to different structures built at different rates: slow-monolayer (I), fast-multilayer (II), slow-monolayer (III), slow-multilayer (IV), fast-multilayer (V) and slow-monolayer and empty space (VI). Scale bar represents 50 μm

In Figure 4.1, we show two regions for an experiment made at 0.5% and without electric field together with the measured evolution. Here, we labelled regions that have different structures. In Figure 4.1(a), **A** areas are compact monolayer deposits, while **B** areas are non-compact dense structures. These areas are closely correlated with the transition from a low to high velocity in the evolution plot. In Figure 4.1(b) we show an example of the complex dynamics that can be observed¹. In this case, several transitions took place between compact monolayer and multilayer regions. We observe that multilayer could present high velocity peaks (**II** and **V**) and, in occasions,

¹Note that in this example the time scale is larger than in Figure 4.1(a)

low velocity plateaus (like in region **IV**). In general, we observed that **NC** and **CM** structures were associated to low velocities, while **NCD** were built at higher velocities. We observed that multilayer deposits could be form at high or low velocities.

To understand the origin of these observations, let us consider the set of snapshots presented in Figure 4.2. Here, we see the process of formation of a **NCD** deposit at large magnification. The dark area at the top of these images is a **CM** deposit, the highlighted stripes are few particle diameters wide. On these images, we observe that the structure starts to form over the substrate (regions highlighted by the rectangles) but, at some point, part of the structure breaks. If we concentrate on the transition from images 1 to 2 (in the red rectangle) we see that the band that was deposited on 1 broke creating an arc above it. Similarly, it occurs between images 3 and 4 (in both rectangles), where structure that was deposited breaks into a new configuration. This sequence illustrates the process of formation of these **NCD** structures: flow of fluid drags the particles from the bulk towards the substrate. The particles reach a stable point where the interaction between them and the substrate locks the particle in an equilibrium position. Here, the particles accumulate forming a highly horizontal band. As the fluid that wets this structure evaporates, the capillary force increases. Then, some particles detach and move towards the upper structure following the stream lines. These released particles rapidly redeposit without forming a compact structure (see Figure 4.2 red square in snapshot 2).

The main forces acting on the process of formation are the capillary immersion forces and the interaction particle-substrate (mainly due to the disjoining pressure). Now, we will detail how each of the different structures that we observed (classified as in chapter 3) gives a different scheme for capillary forces and evaporation rates. In Figure 4.3, we show a sketch for each situation:

- *Figure 4.3(a) - Non-compact deposit (**NC**)*. In this case, we found, almost exclusively, chains oriented parallel to the contact line. This indicates that capillary forces are effective only in the direction parallel to the contact line. The forces attract the particles to form a chain but they are not effective at bringing consecutive chains together. This is probably due to the low concentration of particles near the meniscus. A low concentration implies a small number of particles dragged to the surface by the flows. Hence, when particles are close to a deposited structure the capillary forces had decreased. Then, the structure deposited does not affect greatly the following structure.
- *Figure 4.3(b) - Non-compact dense deposit (**NCD**)*. Particles form a porous structure with large areas of fluid exposed. As the fluid evaporates, the contact angle between the fluid and the particles increases. While the particles are fixed to the substrate the increase of capillary forces increase the flows that bring more particles towards the deposited structure.
- *Figure 4.3(c) - Compact monolayer (**CM**)*. In this close-packed deposit, the fluid exposed through the pores of the structure is at its minimum. Here the evaporation is minimised thus, the flows responsible of the drag of particles to the structure are smaller than in **NCD** structures. The temporal evolution of the low concentration suspension showed two very close velocities (recall Figure 3.7(a)). At this concentration, we only observed **NC** and **CM** structure, thus this two velocities can be associated to this two structures (compare Figures 4.3(a) and (c)).
- *Figure 4.3(d) - Multilayer (**ML**)*. Although we do not have access to the internal structure it

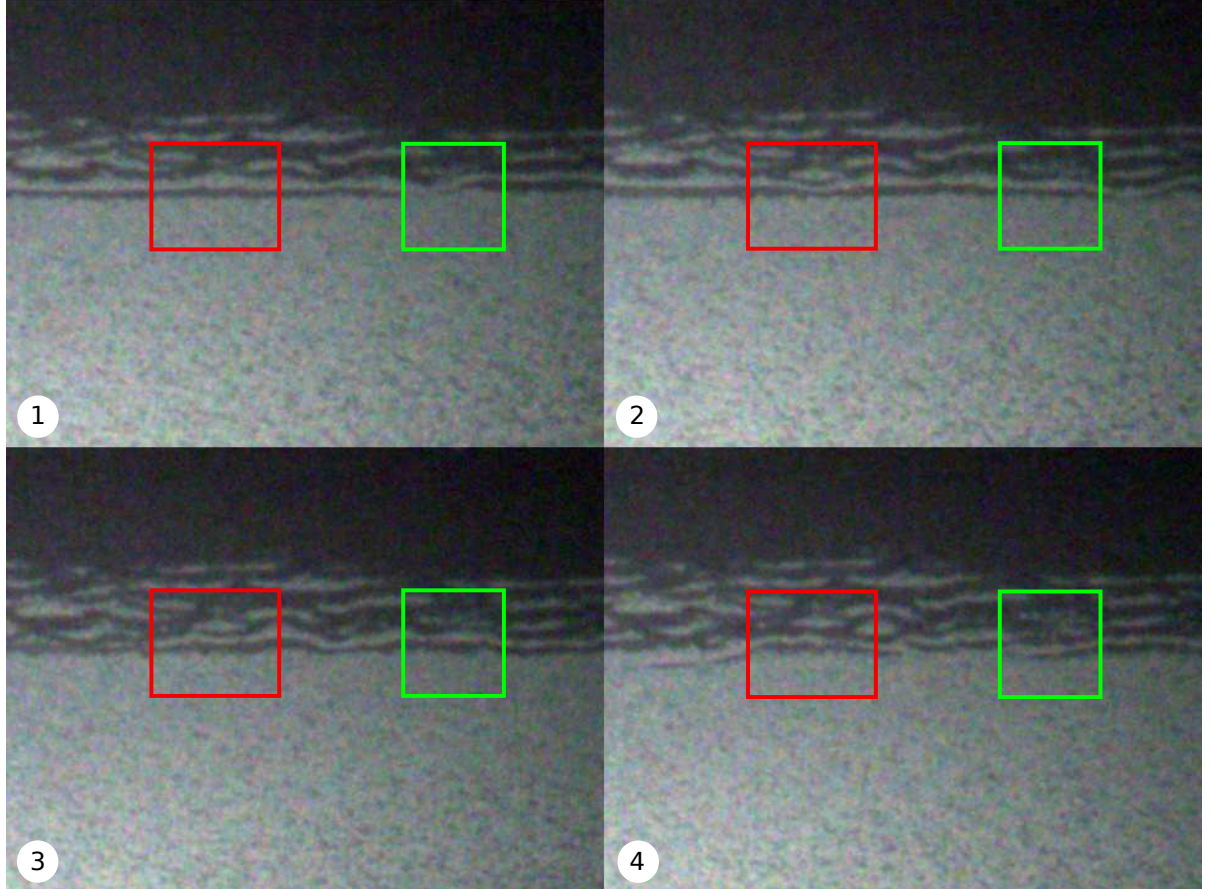


Figure 4.2: Consecutive snapshots of the process of formation of a non-compact dense deposit. The upper region, of each image, is a deposited **CM** structure; the bottom region correspond to the bulk. The rectangles mark areas where is evident the formation process:the structure is initially formed at certain distance from the previous structure (green rectangle, frame 1 to 2); as evaporation evolves the increasing capillary forces break the structure (red rectangle, frame 1 to 2, and green rectangle, frame 3 to 4). Time between frames is 0.5 s

could present two states: either a three-dimensional close-packed or a heterogeneous porous structure. In the first case, it would behave similarly to the **CM** situation where evaporation in the structure is small. In the latter, it would behave more similar to the **NCD** since defects in the structure provide surface that increase effective evaporation rate (see lateral view on Figure 4.3(b) and (d)). Additionally, a wet thick structure has a larger volume of fluid incorporated into the structure.

In summary, due to the presence of the structures, the particles in the bulk will be dragged with different intensity towards the contact line. The different compactness gives distinct exposed surfaces. Thus, one having larger evaporation rates than others. Continuity equation [8] oblige flows to be larger in **NCD** structures than in **NC** or **CM**, therefore growing faster. That the **ML** grows either at high or low rates could be result from multilayers with different compactness. The different situations are sketched on Figure 4.4(a) where the velocity at which a structure

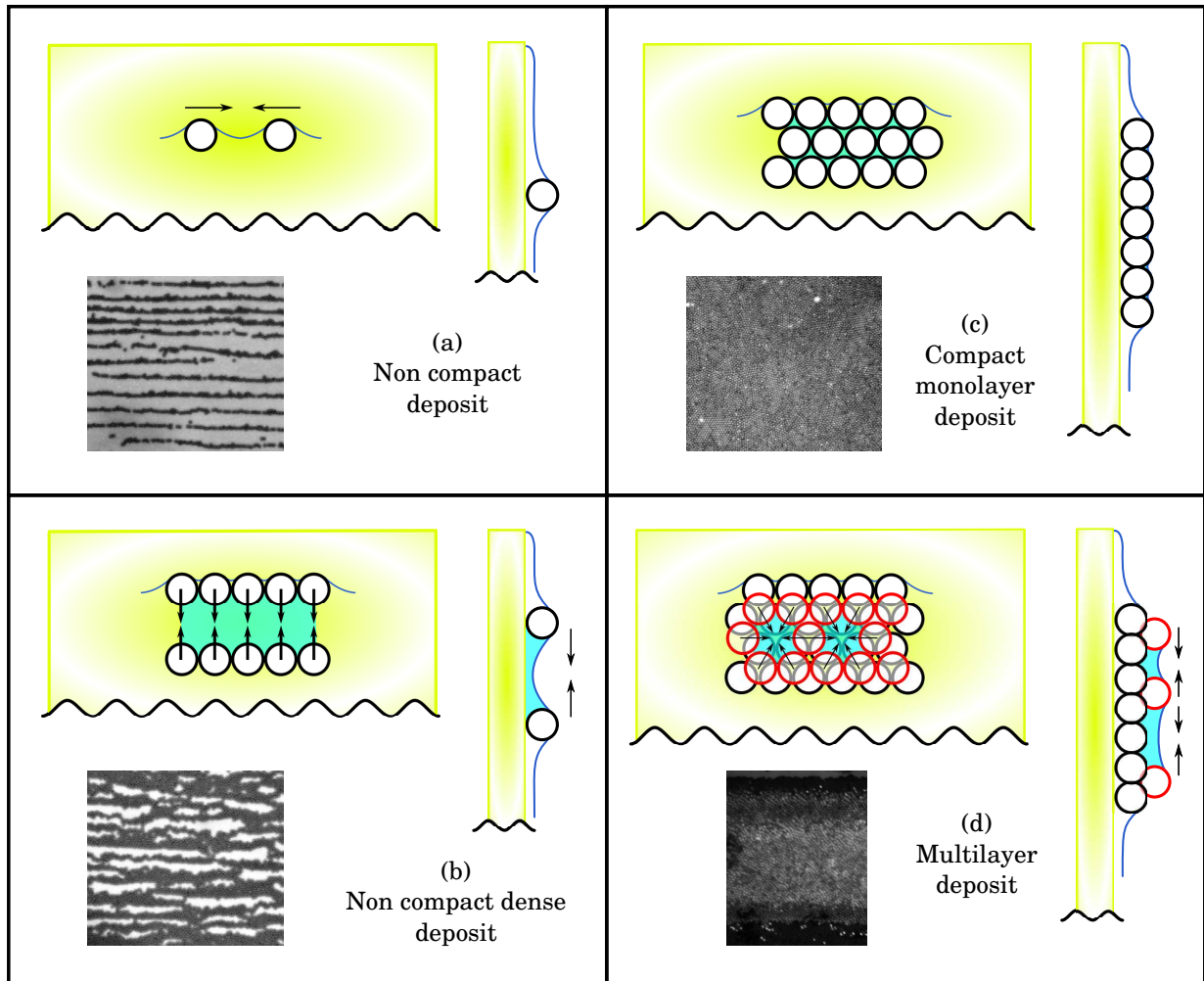


Figure 4.3: Schematic representation of each deposit and the capillary forces that the fluid exert on the particles (marked by the black arrows). (a) In the case of very low concentration, most common interaction is between particles trapped in the contact line where the capillary forces bring them together to form lines (like the ones showed on the picture). (b) At slightly larger concentrations the particles also interact in the plane of the substrate packing in dense bands as in Figure 4.2. (c) Larger concentration gives a compact monolayer where the structure reached the minimum of capillary energy. (d) In most cases, multilayer structures present a heterogeneous thickness (recall comments on Figure 3.1(d)). This give rise to sites where evaporation could be comparable to the **NCD** structures.

tend to grow is represented by the number of arrows in the meniscus.

Similarly, this effect of the structure on the flows explains the columnar arrangement presented in chapter 3 (recall Figure 3.2). Since capillary flows are larger where the free surface has been perturbed the most, the **NC** or the **ML** (on Figure 3.2(a) and (b), respectively) generate larger flows than their neighbouring structures (bare substrate in the former case and **CM** or **NCD** in the latter [69, 70]). Thus, some kind of feedback mechanism is established where the particles accumulate around the areas with larger flows (hence, columns tend to widen) and the adjacent

areas form a less dense structure. Although the initial growth of a columnar structure probably depends on many factors (local heterogeneity in the wetting, presence of impurities, different local concentration), once the structure has been formed, the feedback mechanism maintains it and allows it to grow while particles are available.

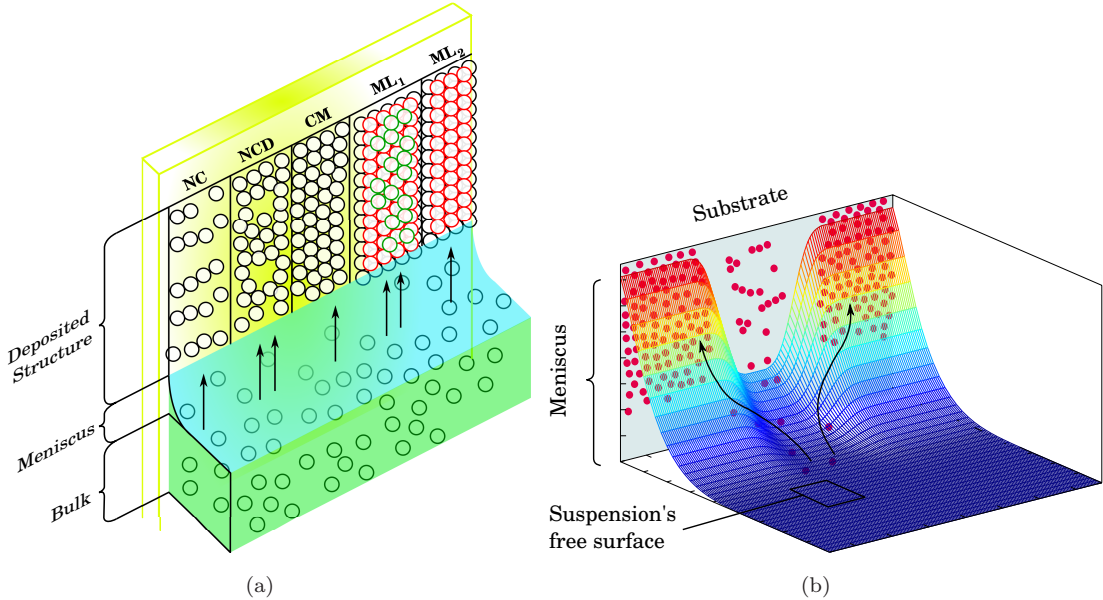


Figure 4.4: (a) Schematic figure representing the effect of the different deposit on the velocity at which the particles are dragged to the deposition zone. A situation of fast and slow growing multilayer are denoted as **ML**₁ and **ML**₂, respectively. (b) Scheme representing the deformation of the meniscus in the vicinity of a columnar arrangement. Here we represent two regions with large capillary energy that enclose a region with smaller energy. This unbalance of energies generates flows that tend to increase that difference even more until the structure finally breaks due to absence of particles in the deposition zone.

As a corollary, the deposited structure is determined by the flux of particles that arrive to the contact line. This flux depends on the flow induced by the evaporation and on the local concentration of particles near the contact line. The combination of these two elements is responsible of the complex dynamics that we observe (see Figure 4.1(b)) since they can be affected by several parameters. Additionally, the concentration will change due to the macroscopic flow (mentioned in section 3.4), the kind of structure deposited and the velocity at which it is constructed, and on the structure that has been formed in the neighbouring areas (recall columnar arrangements in Figure 4.4(b) and 3.2).

In [70] we denoted a region near the contact line from which particles are transported to substrate (similarly to the introduced by Shimmin *et al.* [45]). We named this region as Particle Pool Zone (PPZ) in order to simplify the discussion over the different parameters that affect the formation of structures. If the PPZ region is depleted, it will not be any particle available to form a structure. The depletion of this zone occurs when particles are deposited or when they are dragged to the bulk of the suspension by macroscopic flows (Figure 3.8). Nevertheless, this flows also can replenish the zone by carrying particles from the laterals of the cell (recall Figure

3.8). Thus, to obtain a homogeneous deposit, the PPZ should replenish at the same rate that it is depleted by the deposition. In the unforced system that we study, this condition is not satisfied. Hence, the structure have the rich dynamics observed in Figure 4.1(b).

Under this picture, what would be the effect of the electric fields? To answer this question, we will consider the effect of the different mechanisms introduced in section 1.2.1.

1. Electrophoresis. The electrophoretic effect of the fields can be taken into account considering equation 1.16 introduced on chapter 1:

$$\vec{u} = \frac{q\vec{E}}{6\pi\eta r} \quad (4.1)$$

typical values for our system are:

$$\begin{aligned} r &\approx 0.7 \times 10^{-6} m \\ Q &\approx 4.4 \times 10^{-13} C \\ \eta &\approx 1 cP = 10^{-3} Ns/m^2 \\ E &\approx 1V/mm = \times 10^3 V/m \end{aligned} \quad (4.2)$$

Here, Q is the charge in the surface of the sphere, while q is the effective charge of the surface of the particle (i.e. Q and the charge in the Stern layer). Thus, before estimating the electrophoretic effect we need to take into account the Stern double layer effect. The Stern layer will screen part of the surface charge. Thus, to estimate the electrophoretic limit velocity we will used the Smoluchowski approximation (valid for $\kappa r \gg 1$) that relates the electrophoretic mobility μ with the Zeta potential [51]:

$$\begin{aligned} \mu &= \frac{u}{E} = \frac{q}{6\pi\mu r} \\ \zeta &= \frac{Q}{4\pi\epsilon_m\epsilon_0 r(1 + \kappa r)} \\ \zeta &= \frac{\eta\mu}{\epsilon_m\epsilon_0} \text{ (Smoluchowski)} \\ u &= \frac{E\epsilon_m\epsilon_0\zeta}{\eta} \sim 10^{-5} m/s = 10 \mu\text{m/s} \end{aligned} \quad (4.3)$$

This estimation tells us that the electric field can induce a redistribution of the charges in the suspension (particles and possible electrolytes in solution) until a new equilibrium is established. The electrophoretic velocity of the particles is in the same direction than the applied fields. Thus, the particles are not able to travel more than 1 mm at this velocity, that is, the distance between electrodes. At a velocity of $10 \mu\text{m/s}$ the particles will cover this distance in 100 s. Hence, we expect that the electrophoretic will play a relevant role only during the firsts minutes after the suspension is loaded in the cell. It is clear that is not contributing directly to the velocity of the contact line since the velocity of the contact line is ten times smaller than this electrophoretic velocity. Nevertheless, the stationary situation established by the electrophoretic effect could be disrupted by the flows present in the bulk. Thus, electrophoretic phenomena can still be taking place at longer times.

2. Dielectrophoresis. The dielectrophoretic force depends on the spatial heterogeneity of the electric field. To estimate this parameter we consider the area between the electrodes as composed by two different materials separated by the contact line. Below we will have the suspension which, as is mostly composed by water, we will take to have a permittivity of the order of $10^2\epsilon_0$. In the upper part of the capacitor we have humid air: that has a permittivity of the order of ϵ_0 [102]. Since the difference in permittivities is so large we assume, as a first approximation, that the field in the region of the meniscus follows approximately the shape of the free surface. The symmetry of the meniscus imposes that the field can only vary on the yz plane (see Figure 4.5(a)). To estimate the order of magnitude of this effect, we approximate the ∇E_0^2 term as:

$$\begin{aligned}\nabla E_0^2 &\sim \frac{\Delta E_0^2}{\Delta l} \sim \frac{(E(\epsilon_0) - E(100\epsilon_0))^2}{\Delta l} \\ \nabla E_0^2 &\sim \frac{(\frac{\sigma}{2\epsilon_0} - \frac{\sigma}{200\epsilon_0})^2}{\Delta l} \\ \vec{F} = 2\pi\epsilon_m a^3 K \nabla E_0^2 &\sim 10^{-9} * 10^{-18} \nabla E_0^2 \sim 10^{-27} \nabla E_0^2\end{aligned}$$

to estimate the order of magnitude of this effect we assume a quadratic electric field with a minimum at the middle distance between the plates (see Figure 4.5(a)).

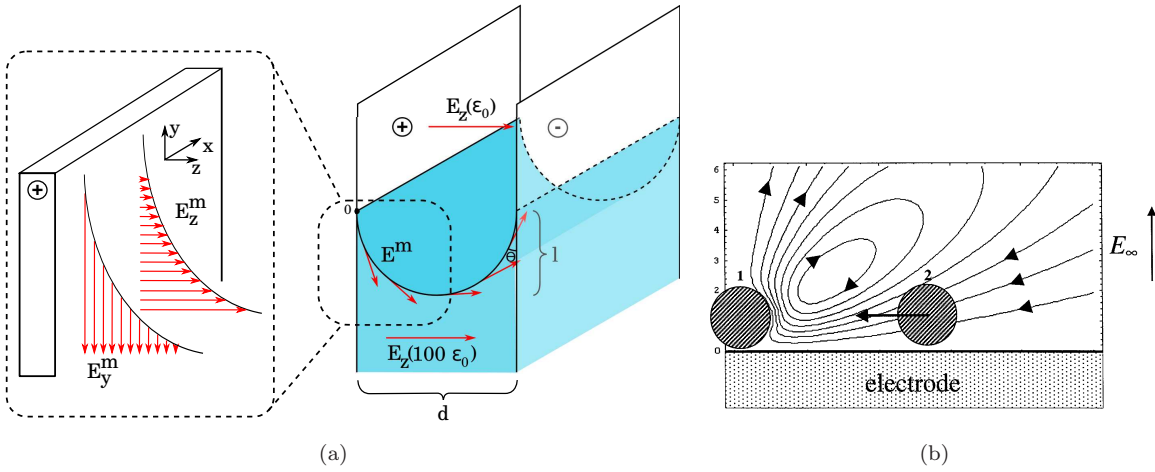


Figure 4.5: (a) Dielectrophoretic effect. Schematic representation of the electric field between the electrodes. The upper medium is considered as humid air ($E(\epsilon_0)$), the lower medium is the suspension ($E(100\epsilon_0)$). The field near the meniscus follow the free surface of the suspension ($\vec{E}^m = E_y^m \hat{y} + E_z^m \hat{z}$). Near the contact line the field is orientated with the contact angle (θ). We take the origin of the coordinate system at the contact line. (b) Electro-osmosis effect. Streamlines of the flows generated by electro-osmosis near an electrode. When two particles are close enough, these flows tend to bring them together. Image extracted from [53].

Hence, the field could be expressed as:

$$\begin{aligned} E_y^m &= E(\epsilon_0)(z - d/2)^2 \\ E_z^m &= E(\epsilon_0)(y - l)^2 \\ \nabla E_0^2 &= \nabla(E(\epsilon_0)^2(z - d/2)^4 + E(\epsilon_0)^2(y - l)^4) \\ &= E(\epsilon_0)^2(4(z - d/2)^3 + 4(y - l)^3) \sim 10^{-3} \\ |\vec{F}| &= 10^{-30} \text{ N} \end{aligned}$$

where, E_y^m and E_z^m are the vertical and horizontal component of the electric field magnitude E . All distances are taken to be in the order of millimetres, and we take the largest field to obtain an upper limit for the estimation. We compare this force with the electrophoretic force to establish its relative importance:

$$\begin{aligned} \vec{F}_{dielectric} &\sim 10^{-30} \text{ N} \\ \vec{F}_{el} &= q\vec{E} \sim 10^{-10} \text{ N} \end{aligned}$$

From this comparison we conclude that the dielectrophoretic contribution to the transport of particles can be neglected.

3. Electro-osmosis. This effect has been used to explain attraction and repulsion of particles near electrodes [53, 103]. The magnitude of its consequences depends on the concentration and type of electrolytes present in the suspension. We did not have access to this data. The experiments reported in [103] and [53] were carried out with larger particles ($4\text{-}10 \mu\text{m}$) and smaller fields ($10\text{-}100 \text{ V/m}$). In our case, the effect could be relevant, although a quantitative evaluation is necessary to confirm its contribution. Given that we are observing the positive electrode, the electro-osmotic flows will tend to bring the particles together [103]. Nevertheless, an ongoing collaborative research in similar conditions, but in a minimised evaporation setup, suggests that electro-osmosis effect can be neglected.

4. Streaming potential. In chapter 1, we introduced the effect of fluid flows in a capillary with charged walls. In our case, a similar situation takes place in the deposited structure. Here the charged surface (substrate) experiences the flows by the evaporation of water in the porous structure. From section 1.2.1 we know that the induced field between the upper and bottom part of the capillary is given by:

$$V_{str} = \frac{\epsilon_0 \epsilon \zeta \Delta p}{\eta K} \quad (1.19)$$

If we apply Bernoulli equation between the extremes of the capillary, we get that the pressure drop will be:

$$\begin{aligned} \frac{v_2^2 - v_1^2}{2} + g\Delta h + \frac{\Delta p}{\rho} &= 0 \\ \Delta p &\sim 10^3(10^{-12} + 10^{-5}) \sim 10^{-2} \text{ Pa} \end{aligned} \quad (4.4)$$

Here, assumed that the fluid velocity at the entrance of the capillary is on the order of $1 \mu\text{m/s}$, the velocity at the end of the capillary is zero, and that the length of the capillary is of the order of $1 \mu\text{m}$.

We can estimate the bulk conductivity from the current measured during the experiment. The current is on the order of $0.1 \mu\text{A}$, circulating in the space between the substrates. Thus, the conductivity can be estimated as:

$$\begin{aligned} K &= \frac{1}{\rho_e} = \frac{l}{RA} = \frac{lI}{VA} \\ &= \frac{10^{-3}10^{-7}}{10^{-4}} (\Omega \text{ m})^{-1} \\ &= 10^{-6} (\Omega \text{ m})^{-1} \end{aligned} \quad (4.5)$$

here, we took l as the distance between substrates (1 mm), $V=1 \text{ V}$ and $A=100 \text{ mm}^2$; ρ_e is the resistivity of the suspension and we used Ohm law: $IR = V$.

Then, substituting in equation 1.19 we obtain:

$$\begin{aligned} V_{str} &\sim 10^{-4} \text{ V} \\ E_{str} &\sim 10^{-4}/10^{-6} \text{ V/m} = 10^2 \text{ V/m} \end{aligned} \quad (4.6)$$

This electric field is directed parallel to the electrode surface and, since the surface is positively charged, it applies a force, opposite to the direction of flows, to the negatively charged particles. Its magnitude is of the same order of magnitude as the applied fields ($\sim 10^3 \text{ V/m}$). Here, we have neglected the effect of the diffuse layer of the particles that behaves oppositely. Therefore, we expect the effect of the streaming potential to be smaller than this estimation.

5. Sedimentation potential. As introduced in section 1.2.1 this potential is given by:

$$V_{sed} = -\frac{\epsilon_0 \epsilon \zeta \Delta \rho g \phi}{\eta K} \quad (1.20)$$

The difference in density between the polystyrene particles and water is of the order of 10^{-3} g/cm^3 (or 1 Kg/m^3). Thus, using the conductivity that we estimated in the previous paragraph, the potential is:

$$\begin{aligned} |V_{sed}| &\sim 10^{-2} \text{ V} \\ |E| &\sim 10^{-2}/10^{-6} \text{ V/m} = 1 \text{ V/m} \end{aligned} \quad (4.7)$$

We expect the effects of this field to be negligible provided that they are 3 orders of magnitude smaller than the applied one. Also, we observed macroscopic flows (section 3.4) that had components in the upward and downward direction. The speed of these flows is much larger than the sedimentation speed of the particles. Thus, the flows contribution to the potential dominates over the sedimentation fields. Nevertheless, as the flows have components in opposite directions, their fields will tend to cancel each other.

6. Electrowetting. The change of the contact angle due to the electrowetting effect can be estimated by the equilibrium condition for a parallel-capacitor [104] derived in the introduction equation 1.26. We rewrite this equation as a function of the voltage difference between electrodes V :

$$\cos(\theta) = \cos(\theta_0) + \frac{\epsilon V^2}{2\gamma_{12}d} \quad (4.8)$$

where θ and θ_0 are the equilibrium angles with and without fields, respectively, ϵ is the electric permittivity of the dielectric layer covering the electrode, γ_{12} is the surface tension between the fluids (suspension and air in our case), and d is the distance between plates. By studying the electrowetting effect with this equation, we are simplifying the highly heterogeneous real system to an idealised situation. In this simple approach, the deposited structure is taken as a dielectric layer through which the voltage interact with the contact angle, which we consider composed only by a pure fluid with the physical properties of the suspension. Although this calculation will not represent exactly the real situation it will establish an order of magnitude for the effect of the electric field over the contact angle. As a first approximation, we will consider ϵ to be between the polystyrene and the water permittivities [25,100] ϵ_0 . In this way, the change in the equilibrium contact angle induced by the fields will be:

$$\cos(\theta) - \cos(\theta_0) = \frac{\epsilon V^2}{2\gamma_{12}d} \approx \frac{[10, 10^3] \times 10^{-12} \frac{N}{V^2} \times 1V^2}{10^{-7} N} = [10^{-4} 10^{-2}] \quad (4.9)$$

For the different suspensions used, we established an equilibrium contact angle in the interval $[30^\circ, 50^\circ]$, without voltage. This implies a maximum change on the contact angle of about 1% (0.5° respect a $\theta_0 = 45^\circ$). Given this small effect, we consider that electrowetting plays a minor role in our experiment.

3. Electrostatics. We are not able to establish precisely the electrolyte nature and proportion in the suspension. This information is necessary to quantitatively compare the effects of the different applied voltages [71]. Nevertheless, as we concentrate on the positive electrode, we know that the interaction between the particles and the observed substrate will be purely attractive (recall Figure 1.7). Also, the increase of the electric field gives an increment of the attractive potential. Thus, the interaction particle-substrate is stronger as we increase the voltage.

In summary, we expect that the effect of electrowetting, dielectrophoresis, electro-osmosis, streaming and sedimentation potential is going to be small in our system, while the electrostatic and electrophoretic effects could be relevant.

The current registered during the experiment shows that, initially, there is a rearrangement of charges that gives a large contribution to the current (recall Figure 2.3). By the time the measures are done, the steady state of the current is achieved and its value is in good agreement with the conductivity of ultrapure water ($5.5 \cdot 10^{-6} \Omega^{-1} m^{-1}$). Therefore, we expect that most electrophoretic phenomena occur in the times previous to the *in-situ* measures. The electrophoretic effect is, then, to increase the concentration of particles near the positive electrode. This is in agreement with the higher density deposits observed on the substrates when higher voltages were applied.

The electrostatic effect will increase the interaction between the particles and the substrate. If this interaction is strong enough the capillary force does not drag the particles once they are in contact with the substrate. This mechanism can address for the periodic banding presented in Figure 3.4(a). To clarify, let us consider the series of snapshot in Figure 4.2; there we showed the process of formation of a **NCD** structure. We observed a two steps formation process: an

initial highly horizontal band is formed and, in a second step, is disrupted by capillary forces. If the particle-substrate interaction is large enough the initial horizontal bands would prevail during the drying process and thus could give origin to structures as the ones shown in Figure 3.4(a).

At higher voltages the bands disappear, as observed in Figure 3.4(b). This could result from the increase in the particle-substrate interaction, induced by the increase in voltage coupled with an increment the volume fraction of particles near the positive electrode (due to the electrophoretic effect). In this situation, is likely that particles will randomly attach to the substrate before the contact line arrives. When the contact line approaches to this adhered particles it will be distorted and the resultant deposit could be a highly heterogeneous structure as the ones observed in Figure 3.4(b).

The effect of voltages on the characteristic velocities (recall Figure 3.6) is a challenging point. There are many parameters involved that are difficult to evaluate. In what follows we discuss these issues under hypothesis that the electric field produces an increase of the local concentration near the contact line.

At low concentration (0.1%) the deposit is dominated by **NC** structures. Application of the electric field does not appear to modify this observation or the growth velocity of the deposit. This observations indicate that the increase of concentration, induced by the electrophoretic effect, is not enough to allow the formation of more compact structures that are associated to larger speeds (like **NCD**).

At 0.3% we found an increase of the velocity with the application of voltages (0.2 V) that remained approximately constant despite further increases (0.4-0.6 V). Additionally, both characteristic velocities behave in a similar manner. This indicates that structures with low growth velocity (**NC** and **CM** or slow **ML**) suffer a similar increment that structures with high growth velocity (**NCD** and fast **ML**). This can be the result of the increase of particle concentration in the positive electrode. With this larger availability of particles, a similar structure (that would produce similar convective flows despite the voltage) would grow faster since the flows will be carrying a larger amount of particles. Nevertheless, if this is the case it does not scale with the increase of the field strength since the velocity saturates rapidly. This could result from a screening effect originated by the large concentration of particles.

At even larger concentration (0.5%) we found an asymmetric result: high characteristic velocities decrease, and low characteristic velocities increase slightly. As before, electrophoretic effect should increase the concentration in the vicinity of the positive substrate. Nevertheless, we would expect that the velocity would be affected in a similar manner whether their were high or low. Additionally, in the 0.3% situation we reached what it appear to be a saturation limit. Thus, 0.5% could be in this limit or above it screening to a large extent the electrophoretic effect. A characteristic of the 0.5% deposits is the large amount of columnar **ML** structures (recall Figure 3.3). We established that this kind of deposits tend to perturb their surrounding (recall Figure 4.4(b)). The effect on the characteristic velocities could be given by interaction of these structures.

Nevertheless, regarding the effect of electric fields on the characteristic velocities it is necessary to pursue further studies. There are several effects that we have not considered and could play a relevant role (like the electrokinetic phenomena described above). In order to identify which, and at what degree, each of this processes is affecting the growth velocity of the structure more detailed studies are required. In particular, new experimental setups need to be considered that should allow to investigate these different parameters independently.

Part II

Spin-coating of rapidly dried colloidal suspensions

Chapter 5

Introduction

With respect to the vertical deposition, the spin-coating technique is, somehow, on the other extreme of the colloidal crystallisation framework. It is only very recently that it has been used to produce colloidal crystals, with long range correlation, in a solid form [33, 35, 40–42]. Its main advantage resides on the time that it takes to produce a relatively ordered structure: it ranges from less than a second to a few minutes depending on the experiments. This is a great improvement compared to the typical weeks or months of other methods.

Typical values for the dimensionless numbers introduced in Chapter 1 are: $\text{Re} \ll 1$, $\text{Ca} [10^{-4}, 10^{-3}]$ and $\text{Pe} > 1$.

The study of a fluid with a free surface in contact with a rotating disk had attracted the attention of the scientific community for many years. The case of a thin layer of a viscous fluid was first modelled by Emslie *et al.* in 1958 [9] for a simple non-volatile fluid. Later, the model was extended to non-Newtonian [73] volatile fluids and polymer solutions [10]. From these initially simple models several refinements were developed to consider different aspects that can affect the spin-coating process [74–79]. The main interest on spin-coating was due to its applicability on generating thin layers of polymers for microelectronics purposes [80] and, more recently, for microfluidic devices [81]. Despite the large interest on this subject, the spin-coating of colloidal suspensions was largely unexplored.

In particular, the study of the dynamics has been restricted mainly to pure fluids [82] and polymers [83]. To our best knowledge, the only previous work on the dynamics of spin-coated colloidal suspensions was performed by Rehg and Higgins in 1992 [77] through numerical simulations.

The formation of a colloidal crystal through spin-coating was firstly reported in 2004, by Jiang *et al.* [40]. In this work, they used silica particles suspended in a polymer solution and, after several minutes of spinning, found six bright coloured arms as the ones shown in Figure 5.1(a). They associated these arms to a hexagonal monocrystal structured over the substrate. Later studies found similar results using volatile suspension [33, 35, 41]. In this case, the experiments showed either 4- or 6-arms stars depending on the rotation rate and the kind of fluid used (see Figure 5.1(b) and 5.1(c) bottom). Arcos *et al.* [35] observed that the structure was not a unique well ordered crystal but an orientationally correlated polycrystal. They found that the structure was mostly orientated in the radial direction, rotating around the centre of rotation (see Figure 5.1(c) top).

The long range orientational order is a direct result of the existence of an axisymmetric ar-

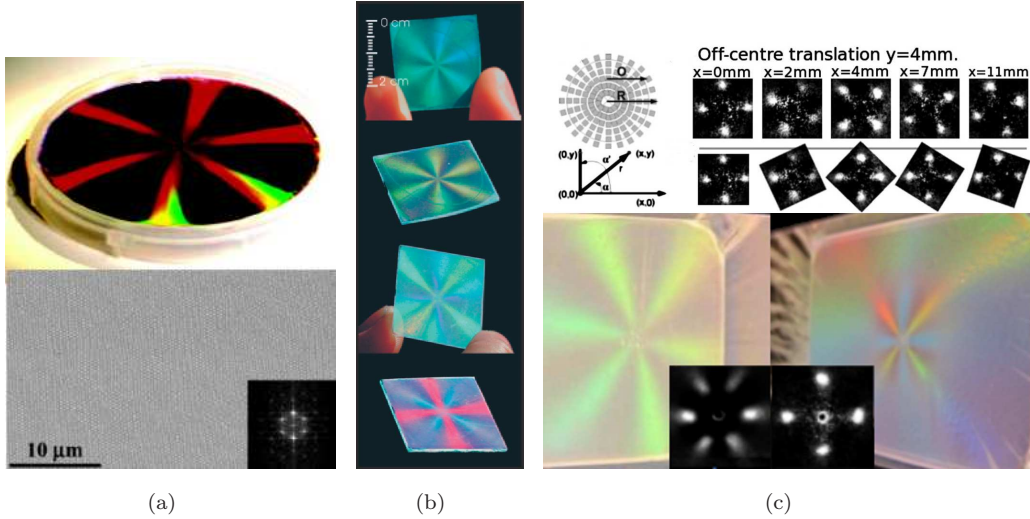


Figure 5.1: Colloidal crystals formed by spin-coating of colloidal suspensions. (a) First report on non-evaporative spin-coating, made with silica particles suspended on a polymers solution. (b) Crystals obtained with evaporative spin coating of polymeric particles suspended on mixtures of different solvents showing two distinct symmetries. (c) Top: Violet laser diffraction patterns that proved the orientational long range order responsible of the characteristics arms. Bottom, evaporative spin coating crystals obtained with silica spheres dispersed in acetone. Images reprinted from [40] (a), [33] (b) and [35] (c)

angement of the hexagonal or square structure. Since the structure has a symmetry (hexagonal or square) as it rotates around the rotation axis, the structure is repeated after certain angle (60° for hexagonal and 90° for square symmetry). In Figure 5.2, we schematised the two situation encountered.

5.1. Emslie model for spin-coating of a viscous fluid

The thinning of a fluid layer over a spinning disk was described in 1958 by Emslie *et al.* [9]. The model assumed a set of simplifications:

- 1 the disk has an infinite radius. Thus, the model would be valid far from the edges of the substrate.
- 2 the disk is perpendicular to the gravity at all times.
- 3 the fluid over the substrate is radially symmetric, and thin enough for the gravitational potential variation of its surface to be negligible (compared to the centrifugal force).
- 4 the fluid is Newtonian, with constant shear viscosity, and the flow is assumed incompressible.
- 5 the shear stress has only horizontal component.
- 6 the radial velocity is small enough in order to neglect Coriolis forces.

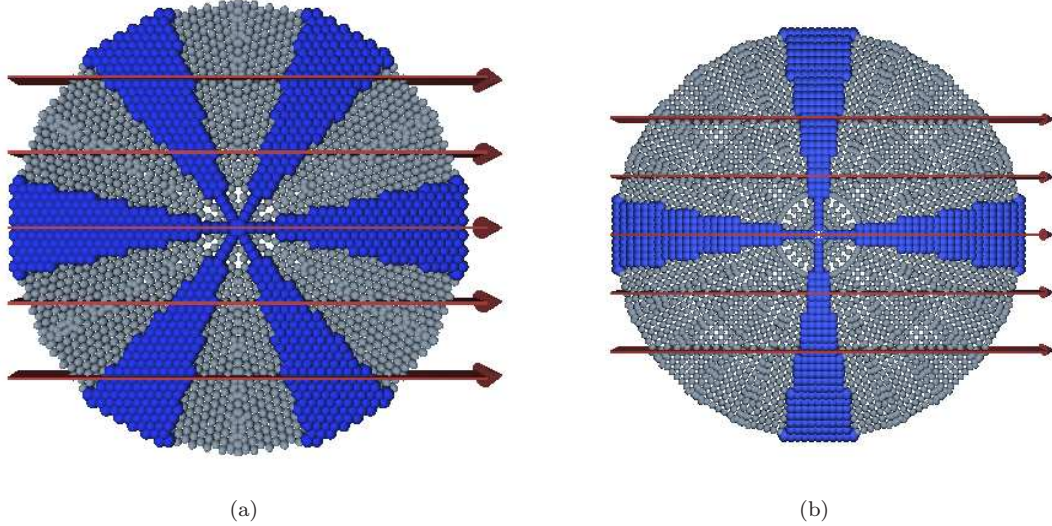


Figure 5.2: Schematised representation of the long range orientational order. (a) An hexagonal structure that rotates around the centre gives rise to six arms. (b) A square structure that rotates around the centre gives rise to four arms. The red arrows indicate the direction of the light that gives constructive interference in the highlighted regions (dark blue).

For the sake of completeness, we are going to reproduce the details in the calculations of Emslie model. We will group some parameters in a slight different manner for our convenience in the following chapters. The starting point of the calculation is the momentum Navier-Stokes equation in cylindrical polar coordinates. From assumption **3** the only relevant contribution to the dynamics would be given by the radial component and the magnitudes can be assumed to be independent of θ . From **4** we can assume that the physical properties are constants. Hence, we start with the radial component of the Navier-Stokes equation:

$$\rho \left(\frac{\partial u_r}{\partial t} + u_r \frac{\partial u_r}{\partial r} + u_z \frac{\partial u_r}{\partial z} \right) = - \frac{\partial p}{\partial r} + \mu \left\{ \frac{\partial}{\partial r} \left[\frac{1}{r} \frac{\partial(r u_r)}{\partial r} \right] + \frac{\partial^2 u_r}{\partial z^2} \right\} \quad (5.1)$$

Here, we can neglect several terms:

- $u_r \frac{\partial u_r}{\partial r}$, from assumption **6**.
- $u_z \frac{\partial u_r}{\partial z}$, then the equation represents a lubrication analysis (i.e. the flow is assumed fully developed instantly).
- $\frac{\partial p}{\partial r}$, from assumption **3**.
- $\frac{\partial}{\partial r} \left[\frac{1}{r} \frac{\partial(r u_r)}{\partial r} \right]$, from assumption **5**.

Hence, the Navier-Stokes equation is simplified to:

$$\rho \frac{\partial u_r}{\partial t} = \mu \frac{\partial^2 u_r}{\partial z^2}$$

Here, we can rewrite the acceleration in the radial direction $\partial u_r / \partial t$ in terms of the angular velocity:

$$\rho \frac{\partial u_r}{\partial t} = -\rho \omega^2 r$$

thus, equation 5.1 takes the simplified form used in [9]:

$$\mu \frac{\partial^2 u_r}{\partial z^2} = -\rho \omega^2 r \quad (5.2)$$

where μ and ρ are the dynamic viscosity and the density of the fluid; ω is the substrate rotation rate. This equation represents the situation where there is a balance between the frictional viscous force and the centrifugal force. The aim of the model is to analyse the thinning dynamics of the fluid. To incorporate the thickness h of the fluid layer they used the continuity equation which, in cylindrical polar coordinates, is:

$$-\frac{\partial \rho}{\partial t} + \frac{1}{r} \frac{\partial(r u_r)}{\partial r} + \frac{\partial u_z}{\partial z} = 0$$

the incompressibility of the fluid ($\frac{\partial \rho}{\partial t} = 0$) simplifies the equation to:

$$\frac{1}{r} \frac{\partial(r u_r)}{\partial r} + \frac{\partial u_z}{\partial z} = 0 \quad (5.3)$$

Integration of this equation with respect to z leads to:

$$\int_0^h \frac{1}{r} \frac{\partial(r u_r)}{\partial r} dz + u_z(h, r, t) - u_z(0, r, t) = 0$$

where $u_z(0, r, t) = 0$ since the substrate is impermeable, and $u_z(h, r, t)$ is the velocity of the free surface of the fluid in the vertical direction; that is, the thinning rate dh/dt :

$$\int_0^h \frac{1}{r} \frac{\partial(r u_r)}{\partial r} dz + \frac{dh}{dt} = 0 \quad (5.4)$$

Now we go back to equation 5.2, from it an expression for u_r can be extracted. First, we integrate respect to z :

$$\int -\mu \frac{\partial^2 u_r}{\partial z^2} dz = -\mu \frac{\partial u_r}{\partial z} + C_1(r, t) = \rho \omega^2 r z + C_1(r, t)$$

C_1 can be determined considering a no shearing condition at the upper surface ($\mu \frac{\partial u_r}{\partial z} |_{z=h} = 0$):

$$0 = \rho \omega^2 r h(r, t) + C_1(r, t) \Rightarrow C_1(r, t) = -\rho \omega^2 r h(r, t)$$

again, integrating with respect to z :

$$\begin{aligned} \int -\mu \frac{\partial u_r}{\partial z} dz &= \int \rho \omega^2 r (z - h(r, t)) dz = \rho \omega^2 r \left(\frac{z^2}{2} - h(r, t)z \right) + C_2(r, t) \\ &= -\mu u_r \end{aligned}$$

$$\rho \omega^2 r \left(\frac{z^2}{2} - h(r, t)z \right) + C_2(r, t) = -\mu u_r$$

here, imposing a no slip condition on the substrate surface ($u_r = 0, z = 0$) yields C_2 :

$$0 = -\mu u_r \Big|_{z=0} = \left(\rho \omega^2 r \left(\frac{z^2}{2} - h(r, t)z \right) + C_2 \right) \Big|_{z=0} = C_2$$

Therefore, the radial speed of an element of fluid can be written as:

$$u_r = -\frac{\rho \omega^2 r}{\mu} \left(\frac{z^2}{2} - h(r, t)z \right)$$

In the following, we will consider the simplified case of a thickness independent of the radius. This expression for u_r can be used on equation 5.4 and the thinning rate can be determined:

$$\begin{aligned} \frac{1}{r} \frac{\partial}{\partial r} \left\{ r \int_0^h \left[-\frac{\rho \omega^2 r}{\mu} \left(\frac{z^2}{2} - hz \right) \right] dz \right\} + \frac{dh}{dt} &= 0 \\ - \left[\frac{1}{r} \frac{\partial}{\partial r} r^2 \right] \left[\int_0^h \frac{\rho \omega^2}{\mu} \left(\frac{z^2}{2} - hz \right) dz \right] + \frac{dh}{dt} &= 0 \\ - \frac{1}{r} r \left[\int_0^h \frac{\rho \omega^2}{\mu} \left(z^2 - 2hz \right) dz \right] + \frac{dh}{dt} &= 0 \\ - \left[\frac{\rho \omega^2}{\mu} \left(\frac{z^3}{3} - hz^2 \right) \right] \Big|_{z=0}^h + \frac{dh}{dt} &= 0 \\ \frac{2\rho \omega^2 h^3}{3\mu} + \frac{dh}{dt} &= 0 \\ \frac{dh}{dt} &= -\frac{2\rho \omega^2 h^3}{3\mu} \\ \frac{\partial h}{\partial \tau} &= -\frac{2h^3}{3\tilde{\nu}} \end{aligned} \quad (5.5)$$

where $\tilde{\nu} = \mu/(\rho\omega)$ is the kinematic viscosity divided by the rotation rate and $\tau = \omega t$ is a dimensionless time. Additionally, it is separable in τ and h thus, solving it we obtain an explicit expression for $h(\tau)$:

$$\begin{aligned} \frac{dh}{h^3} &= -\frac{2}{3\tilde{\nu}} d\tau \\ \int \frac{dh}{h^3} &= - \int \frac{2}{3\tilde{\nu}} d\tau \\ \frac{h^{-2}}{-2} &= \frac{2}{3\tilde{\nu}} \tau + C_3 \\ \frac{1}{h^2} &= -\frac{4}{3\tilde{\nu}} \tau + C_3^\dagger \\ h &= \frac{1}{\left(\frac{4}{3\tilde{\nu}} \tau + C_3^\dagger \right)^{0.5}} \end{aligned} \quad (5.6)$$

where $C_3^\dagger = -2C_3$ can be determined with the absolute thickness at a specific dimensionless time.

In 1978, Meyerhofer expand Emslie model to volatile fluids by considering that the thickness could also change through evaporation. He considered that it was possible to take it into account in equation 5.5 by simply adding a constant evaporative term $\tilde{\epsilon}$:

$$\frac{\partial h}{\partial \tau} = -\frac{2h^3}{3\tilde{\nu}} + \tilde{\epsilon} \quad (5.7)$$

here, we wrote the evaporation rate as $\tilde{\epsilon} = \epsilon/(A\omega)$ to be consistent with the previous deduction, The evaporation area A is assumed to be constant. Meyerhofer also included the cases of two components fluids and modelled separately the solid and fluid phase. As a consequence of this added complexity, it is not possible to explicitly solve the model and it is necessary to search for a numerical solution for the set of equations.

In chapter 8 we will modify this analysis, by introducing the evaporation rate at a different point of the deduction. This will allow us to still have an exact result that is in very good agreement with our experiments.

5.2. Colloidal suspensions under shearing

Recently, Shereda *et al.* [84] studied the spin-coating of 1 μm diameter poly(methyl methacrylate) (PMMA) spheres suspended on a non-volatile solvent (dioctyl phthalate) ($\mu = 718 \text{ cP}$), at a large concentration $\sim 35\%$. In this highly viscous situation, they studied the effect of the shearing on the suspension crystalline quality. The shear stress τ_{rz} can be obtained from integration of the left term of equation 5.2:

$$\tau_{rz} = - \int_h^z \mu \frac{\partial^2 u_r}{\partial z^2} dz = \int_h^z \rho \omega^2 r dz = \rho \omega^2 r(h - z) \quad (5.8)$$

In Figure 5.3 (left), we show the change they obtained in the crystalline factor (degree of crystalline order) as a function of height ($h=0$ corresponds to the substrate) extracted from confocal images (inset, in Figure 5.3 left). On the right, a colour plot shows the Péclet number (calculated from equation 5.8):

$$Pe \sim \tau_{rz} a^3 / k_b T = \frac{6\pi \rho \omega^2 r (h - z) a^3}{k_b T} \quad (5.9)$$

They included the 6π factor to maintain consistency with the definition of Pe at the infinite dilution limit [50]. From this analysis, the authors observed that the transition from non-crystalline to crystalline order in the suspension corresponded well with a $Pe \sim 1$ (black solid line in the colour plot, Figure 5.3 right), as observed by Ackerson in shearing experiments [85].

It is known since 1980's that hard sphere systems present a phase diagram mainly described by four states as the volume fraction of the suspension increases (see Figure 5.4). At low concentration, the suspension is in a liquid state. As the concentration increases, the system starts to crystallise locally while coexisting with fluid regions. At a volume fraction of 0.545, the system crystallises mainly in a rhcp lattice, but between $\phi = 0.58-0.63$ the crystal goes to a glass state [15]. At larger concentration the crystal state is recovered.

The application of a shear to a hard sphere suspension modifies this phase diagram by the addition of three dynamical regimes depending on the strength of the shearing. Initially, it was studied with light diffraction [14, 17], and more recently with confocal microscopy [87]. The diagram is characterised by three basic states as the shearing rate increases (see Figure 5.5). At low shear rates, consecutive layers displace in a zig-zag movement respect to each other. As shear rate increases, the layers start to move linearly, and eventually, they get disordered in what is called shear-induced melting. The confocal observations [87] confirmed that this melting process is associated to an increase in the fluctuations of the particle position of the order of 12% of the

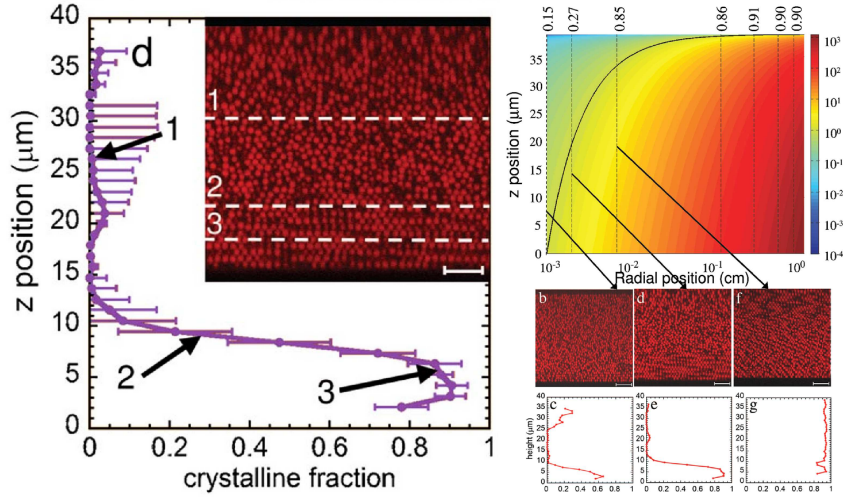


Figure 5.3: Left: Crystalline fraction at different heights on the rotating substrates, they were calculated from confocal images (inset). Numbers indicate three characteristic situation, 1- non-crystalline, 2- transition region, 3- highly crystalline. Right: Colour representation of Pe (equation 5.9) as a function of radial distance and height, colour scale for Pe is presented on the right. Examples for the crystalline fractions at three different radial distances are shown, where it is clearly observed the increase in crystalline fraction as the Pe number increase. The number above the colour representation indicate the mean crystalline fraction at the corresponding radii. Figures taken from Shereda *et al.* [84]

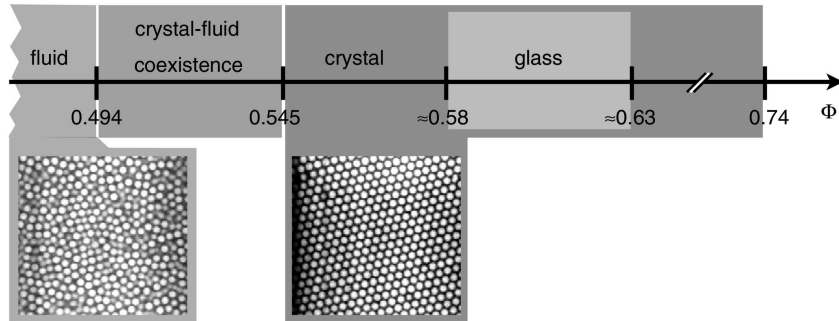


Figure 5.4: Phase diagram for a nearly hard sphere system. As the volume fraction of the suspension increases a series of transition through a liquid, liquid-crystal coexistence, crystal, glass and, again, crystal states. Reprinted from [86]

particle separation. This is in accordance with the Lindemann criterion for molecular crystals, already used by Ackerson to explain this shear-induce melting [14].

The Lindemann criterion establishes that the melting process of a solid starts when the averaged thermal vibration of the atoms or molecules, that compose the solid, are so large that they invade the space of the nearest neighbours [88–90]. As a quantitative measure, it is complex to assess. Lindemann proposed that the melting occurred when the amplitude of this vibrations was of the order of 10% of the nearest neighbour distance. Translated to a colloidal system under shearing, the thermal vibrations are replaced by shear induced fluctuations, thus the name of

shear-induced melting.

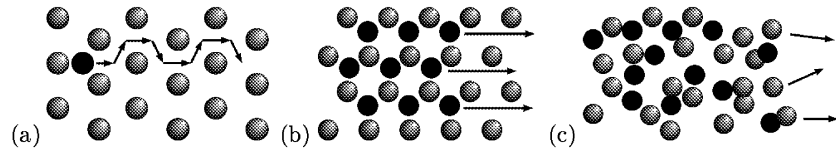


Figure 5.5: Phases in a sheared colloidal suspension. Symbols represent colloidal particle distribution on a plane parallel to the shearing plane, light symbols are the front layer, dark symbols are a consecutive layer, arrows indicate the movement of this second layer with respect to the empty symbols layer. (a) at low shear rates, the layers follow a zig-zag movement. (b) Higher shear rates produce sliding layers, where second layer particles displace along straight lines. (c) Even larger shear rates leads to a disordered phase, through a process known as shear-induced melting. Image reprinted from [91]

Chapter 6

Experimental Setup

We study the spin-coating of silica particles ($458 \text{ nm} \pm 2 \text{ nm}$) dispersed on highly volatile fluids. We used either acetone or methyl-ethyl ketone (MEK) as dispersive medium. Both fluids have similar physical properties except for the vapour pressure (see table 6.1).

	Acetone	Methyl-ethyl ketone (MEK)
Molecular formula	C_3H_6O	C_4H_8O
Density [g/cm ³]	0.79	0.805
Viscosity [cP] at 20°C	0.32	0.42
Boiling point [°C]	56.5	79.6
Vapour pressure [mmHg] at 25°C	230	100
Surface tension [mN/m]	25.2	26.4

Table 6.1: Physical characteristics of acetone and methyl-ethyl ketone

The particles were acquired in dried form (Angströmsphere™, commercially available in Fiber Optic Center inc.). They were dispersed following a previously established procedure [35, 96]. We first weighted the particles and dried them overnight at 150 °C, to eliminate adsorbed water during storage. Later, once the particles have thermalised outside the oven, we add the desired volume of the fluid (acetone or MEK) to reach the working concentration (we used volume fractions of 5, 10, 15 and 20%). The suspension is sonicated at controlled temperature (24-27 °C) for approximately 4 hours. Typically, during the last 2 hours opalescence colours were already observable in the meniscus. Finally, for the sake of reproducibility, we kept the dispersion outside the sonicator for 20 min before carrying out the experiment.

We worked at room temperature ($\approx 25 \text{ }^{\circ}\text{C}$) with a standard spin coater (Laurell technologies, WS-650SZ-6NPP/LITE/OND). The equipment was kept inside a fume hood for protection from the vapours of the solvents.

We used approximately square pieces of silicon wafer ($\sim 25 \text{ mm} \times 25 \text{ mm}$) as substrates, they were cut from standard disks (4 inch diameter). To proper fitting into the spin coater holder, we fixed the substrates into standard microscope slides using UV glue. The cleaning was done with successive rinsing with ethanol and distilled water. We eliminate the excess of water over the substrates by blowing N₂ gas, they were finally dried over a hot plate at 90 °C. To avoid contamination we kept them in a clean container until needed.

Each experiment consisted on pipetting 40 μL of suspension over the substrate already spinning at a constant rate. We finished the experiment by stopping the rotation after the fluid had completely evaporated. This typically occurred in less than 2 s since the pipetting.

We captured high-speed movies of the experiment (1000 frames per second, uncompressed avi format) with two different setups: the first one gives access the long range orientational ordering, the second one gives information on the thinning process (Figures 6.1 A and B, respectively). In both cases, we used a high intensity light source (300 W, incandescent tungsten lamp) but, localised at opposite angles (see Figure 6.1). In the first configuration, we capture the back scattering of the spinning suspension that provides images of bright coloured arms in the fluid and dried phase. This provides a large contrast of the bright arms with respect to the background. In the second configuration, we observe the specular reflection of the light source. This results in interference fringe patterns related to the change in thickness on the spinning fluid (similar to Newton rings). For a correct visualisation of these rings, it was necessary to introduce two additional elements in the optical setup: a diffuser, in front of the light source (to homogenise the illumination); and a band pass filter ($450 \text{ nm} \pm 50 \text{ nm}$), in the lens setup in order to fix the length scale related to the fringes spacing.

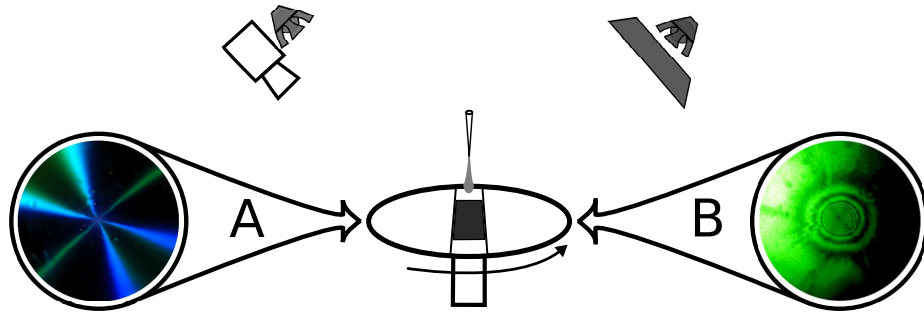


Figure 6.1: General experimental setup: The two lighting setups used allow observation of the two main variables that change in the fluid phase during the experiment, the long range ordering (configuration A) and thickness variations (configuration B).

6.1. Characterisation of the dynamics

We analysed the movies obtained in the experiment (using lighting configuration B) with a homemade software written in Octave®. We split each movie into frames and extract the radial distribution of the light intensity. For this, we defined a set of ring-like masks (four pixels thick in the radial direction) that goes from the centre of rotation up to 200 pixels in radius. On the substrates, this distance represents a circular area of 10 mm in radius. Each mask overlaps with its consecutive in two pixels as shown in Figure 6.2(a).

We mask every frame and decomposed it in consecutively increasing rings. The average grey intensity on each ring is taken to be the mean intensity at the corresponding radial distance. Movies processed in this way give spatiotemporal diagrams like the one shown in Figure 6.2(b). In this figure a banding parallel to the radial axis is observed during the whole experiment, even before the pouring of suspension, thus is a phenomena unrelated to the dynamics of the fluid.

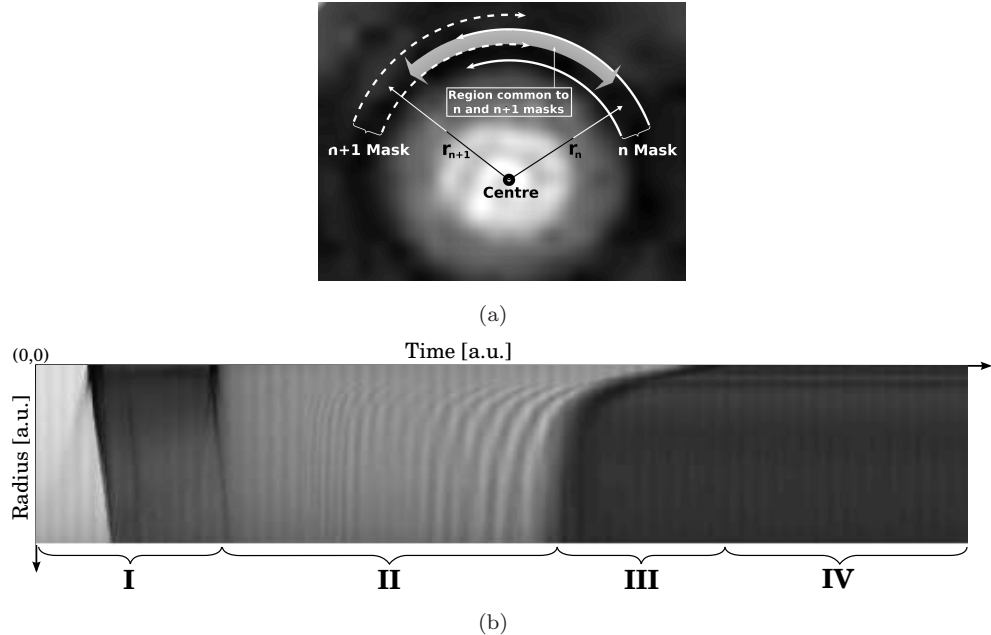


Figure 6.2: (a) Sketch of the overlapping of masks for calculation of radial grey level variation. Half of each mask overlaps with the previous one. (b) Spatio-temporal diagram of the radial grey level. Obtained from light configuration B. We define four stages: (I) pouring, (II) thinning, (III) drying front, (IV) dried structure. The constant periodicity observed in all stages is due to a slight misalignment of the optical setup and the plane of rotation, the frequency of the oscillation coincides with the rotation rate.

we believe that it originates from a slight misalignment of the light source and the plane of the rotating substrate. The spatiotemporal diagrams are characterised by four stages:

1. *Stage I*: Transient initial state. The bright area corresponds to rotation without fluid, while the darker is the suspension that is accelerated and spun away forming Ekman spirals.
2. *Stage II*: A nearly flat fluid film thins homogeneously. The alternating bands in the temporal direction correspond to the alternating bright and dark bands as the suspension thins.
3. *Stage III*: Structure starts to dry. Two areas become clearly distinguishable: dark (dried structure) and bright (wet suspension).
4. *Stage IV*: Completely dried structure rotates with the substrate.

We focus first on the position of the drying front as a function of time, that is the position of the transition from the bright region to the darker one in *Stage III*. In figure 6.3, we show some examples of the averaged grey profile at different times, this are obtaining of the spatiotemporal diagram in *Stage III*. As they change slowly, we were able to measure its relative displacement by convolution of two consecutive profiles.

The dynamics of the thinning process was studied through the fringe patterns in the *Stage II*. We first measured the thinning rate by establishing the frequency at which the rings were passing through a fixed radial position (see Figure 6.4(a)). We performed this measure at three radial

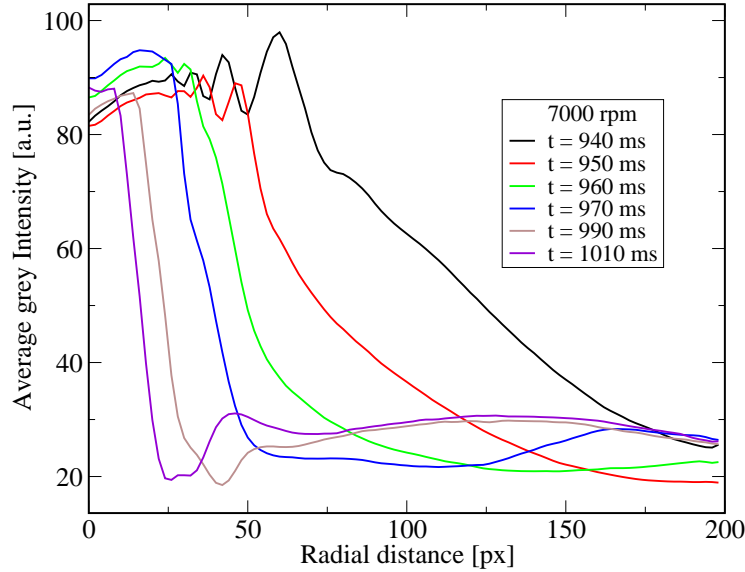


Figure 6.3: Radial profiles of average grey level. We show selected times extracted from the *Stage III* on the spatiotemporal diagram. For the determination of the displacement of the drying front we convolve profiles at t and $t+1$ ms.

distances between 1 and 5 millimetres from the centre. The second measure was made in order to recover the thickness profile for several times. For this, we measure the radial position of each ring (see Figure 6.4(b)) and then consider the thickness difference between them. Both measures are equivalent to move along the spatiotemporal diagram, either at a fixed radial position (first measure) or at fixed time (second measure). They differ essentially in that in the spatiotemporal diagram we performed the azimuthal average.

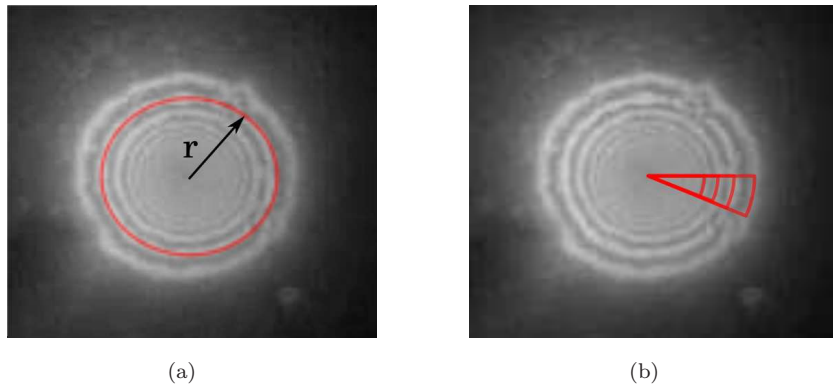


Figure 6.4: Dynamics of thinning. (a) at a fixed radial distance the time between consecutive rings gives the thinning rate. (b) At a fixed time, we measure the distance between consecutive rings obtaining the thickness profile of the fluid.

To calculate the thickness change between consecutive rings we assumed a Newton ring system composed, on one hand, by the top surface of the fluid and, on the other, by the reflective surface of the substrate. The band pass filter in the lens setup fixes the observable wavelength to 540 ± 40 nm,

which leads to a thickness variation (between consecutive bright and dark bands) of:

$$d = \frac{\lambda}{2\langle n_{\text{eff}} \rangle} = \frac{540 \pm 40 \text{ nm}}{2 \times 1.42 \pm 0.04} = 190 \pm 20 \text{ nm} \quad (6.1)$$

The refractive index is not constant since the proportion of components changes dynamically as evaporation occurs. Nevertheless, both components of the suspension had a similar refractive indexes, MEK: 1.38 and SiO₂: 1.46. Therefore, we assumed an effective refractive index of 1.42 with an error that included both limit cases (pure MEK and pure SiO₂).

6.2. Characterisation of the dried structures

The thickness of the deposits was characterised using Atomic Force Microscopy (AFM, Asylum Research MFP-3DTM). We measure the height of the upper surface of the structure, referenced to the substrate. For this, we created a radial reference by scratching off a line going through the centre of rotation or as close to it as possible (Figure 6.5(a)). We operate the probe on contact mode. The tip was lowered until the software register the top surface, then the parameters of the AFM were adjusted to obtain a maximum range of sensitivity. The system, then, measures the deflection of the tip as it scans capturing the topography of the structure. We scanned regions of 90 μm × 90 μm, every 100 μm near the centre where the thickness variations were considerable, and 500 μm far from the centre where the structure was typically flat. The scanning was done in such a way that approximately 10 μm of the 90 μm belong to the exposed surface. An order zero flattening was applied to compensate internal systematic error of the system. Data was analysed with the same IgorPro® software that controls the AFM system. The height from each scanned square area, shown as a grey level image on Figure 6.5(b), was summarised on a histogram. These plots showed typically a bimodal distribution (Figure 6.5(c)) where, each peak represents the height of a main area (substrate or top layer). We force the code to consider only points near the peaks and used those points to fit a Gaussian function on each peak. The thickness was taken as the difference between the means of the fitted Gaussian. Each scanned region had several heights. Therefore, we took as error the sum of the standard deviation for each fitted function. In this way, the thickness and error reported here encompass all the thicknesses present on the scanned areas. In general, both peaks where not perfect Gaussian functions and presented some asymmetry. This was due mainly to the scratch made on the structure used as reference. After the scratch was done, we carefully blow compressed air over the structure to remove as much loose particles as possible. Nevertheless, it was common to have particles or partial deposits on the exposed substrate that gave the second maximum (next to the blue fitted curve in Figure 6.5(c)). Similarly, the scratching process deposits some particles on top of the structure.

The microscopic structure was observed *via* Scanning Electron Microscopy (SEM). As reported previously [35], the top surface of these crystals presented, mainly, either hexagonal or square packing (Figures 6.6 a and b).

In section 8 we will present preliminary results on image processing of SEM images that has been done to quantitatively characterise the structure regarding their symmetry, orientation and domain size.

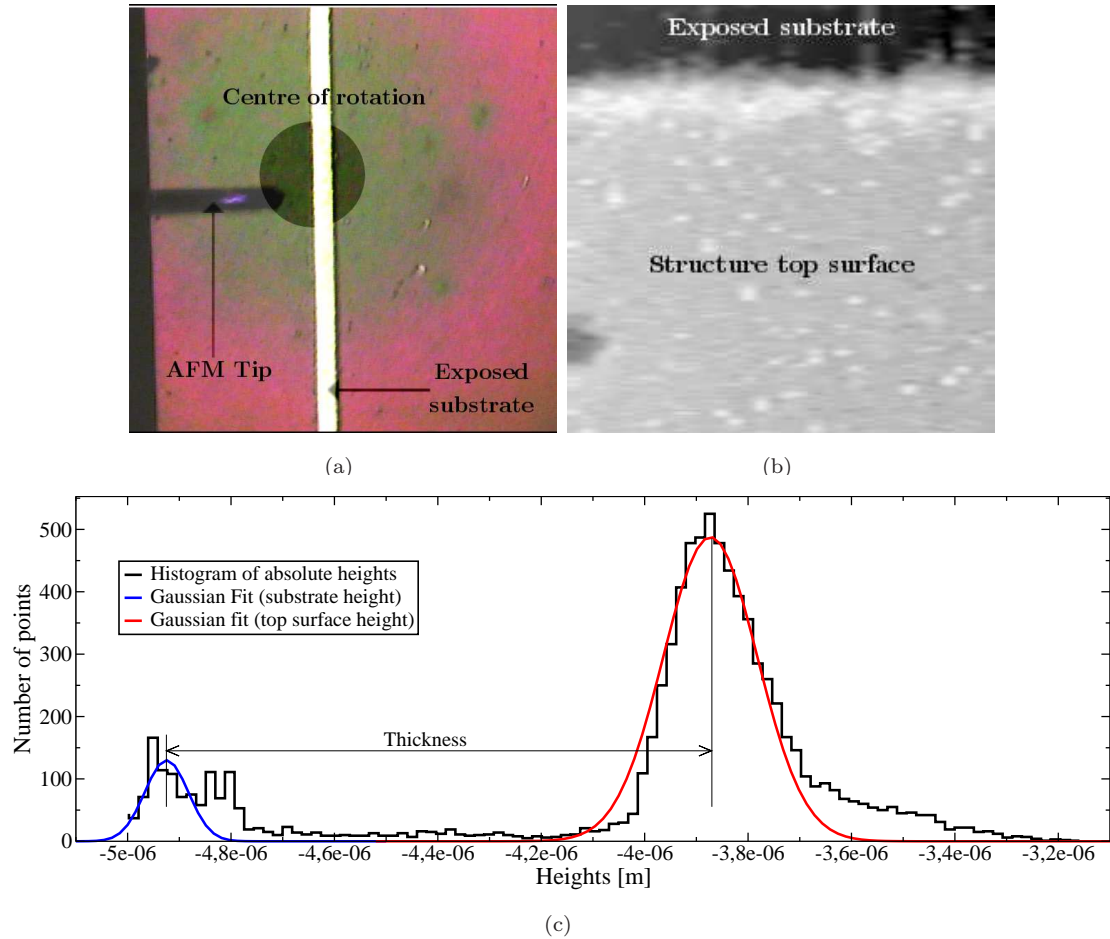


Figure 6.5: a) Optical image of the AFM tip and sample at the moment of measure the thickness near the centre of rotation. b) Grey level representation of a typical AFM scanning along the exposed substrate. c) Histogram of the measured heights and Gaussian fits used to obtain the thickness of the structure.

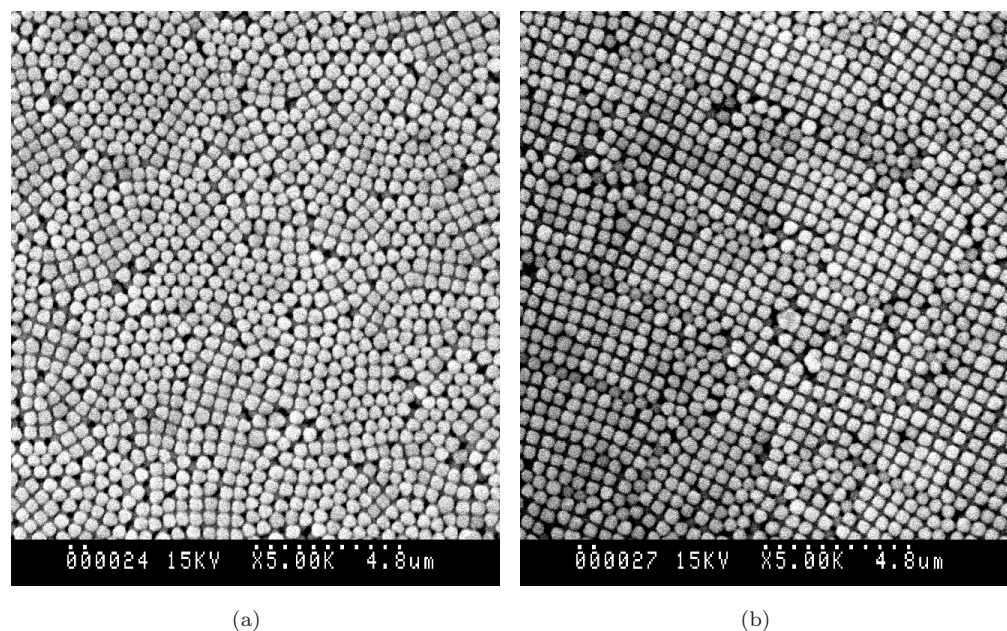


Figure 6.6: SEM images of the top surface of deposits. a) mixture of hexagonal and square arrangement observed on areas exhibiting diffused six arms, b) highly directed square arrangement found in concordance with four arms symmetry in the optical inspection.

Chapter 7

Results

The starting point in the spin-coating of rapidly drying suspensions was the presence of a long range orientational order in the dried structures. This orientational correlation gives rise to macroscopic bright coloured six or four arm stars (recall Figure 5.1). We will show, firstly, the results on thickness profiles for these dried polycrystals obtained at different experimental conditions. We varied the rotation rate of the substrate, the initial concentration of the suspension, the partial vapour pressure in the atmosphere surrounding the substrate, and the fluid used as dispersive medium (MEK or acetone). Then, we will focus on the dynamics of two, *a priori* independent, aspects: the thinning of the suspension and the long range order in the fluid phase. Also, we study the dynamics of the transition from the fluid suspension to the dried polycrystal. Finally, we will present a general description of the macroscopic quality of the arms.

When we mention time, we will refer, almost exclusively, to dimensionless time defined as:

$$\tau = \omega(t - t_{dry}), \quad (7.1)$$

where t_{dry} is the time at which the structure dries completely and ω is the rotation rate of the substrate. This definition established that the time scale is measured as the angle that the substrate had rotated with respect to the position at the moment of final dried t_{dry} . From equation 7.1 all the dynamical measures will take place for negative τ .

7.1. Thickness of the dried polycrystalline structures

We measured the thickness profiles as detailed in section 6. In general, all the profiles showed a similar bell-like shape with the maximum located in the centre of rotation. Outer areas were always flat and the centre itself presents a small plateau (see Figure 7.1(a)). The increase of the rotation rate was accompanied by a decrease of the average thickness. When acetone was used as solvent, the thickness profiles had a similar shape to the obtained with MEK, although they showed a larger average thickness, at the same rotation rate (see Figure 7.1(b)). If we reduce the initial concentration of the suspension, this general picture gets slightly modified. Experiments with 10% showed a displacement of the central maximum from the centre of rotation (see Figure 7.1(c)). Initial concentrations of 15% also appear to have the maximum slightly displaced from the centre of rotation, but the offset is much smaller and the measures are not conclusive. An increase of the partial vapour pressure of the suspension's fluid inside the spin coater had a similar

effect to a reduction of the concentration. In Figure 7.1(c), we see clearly that the saturation of the atmosphere with acetone results on a thickness profile equivalent to reduce the initial concentration from 20% to 15%.

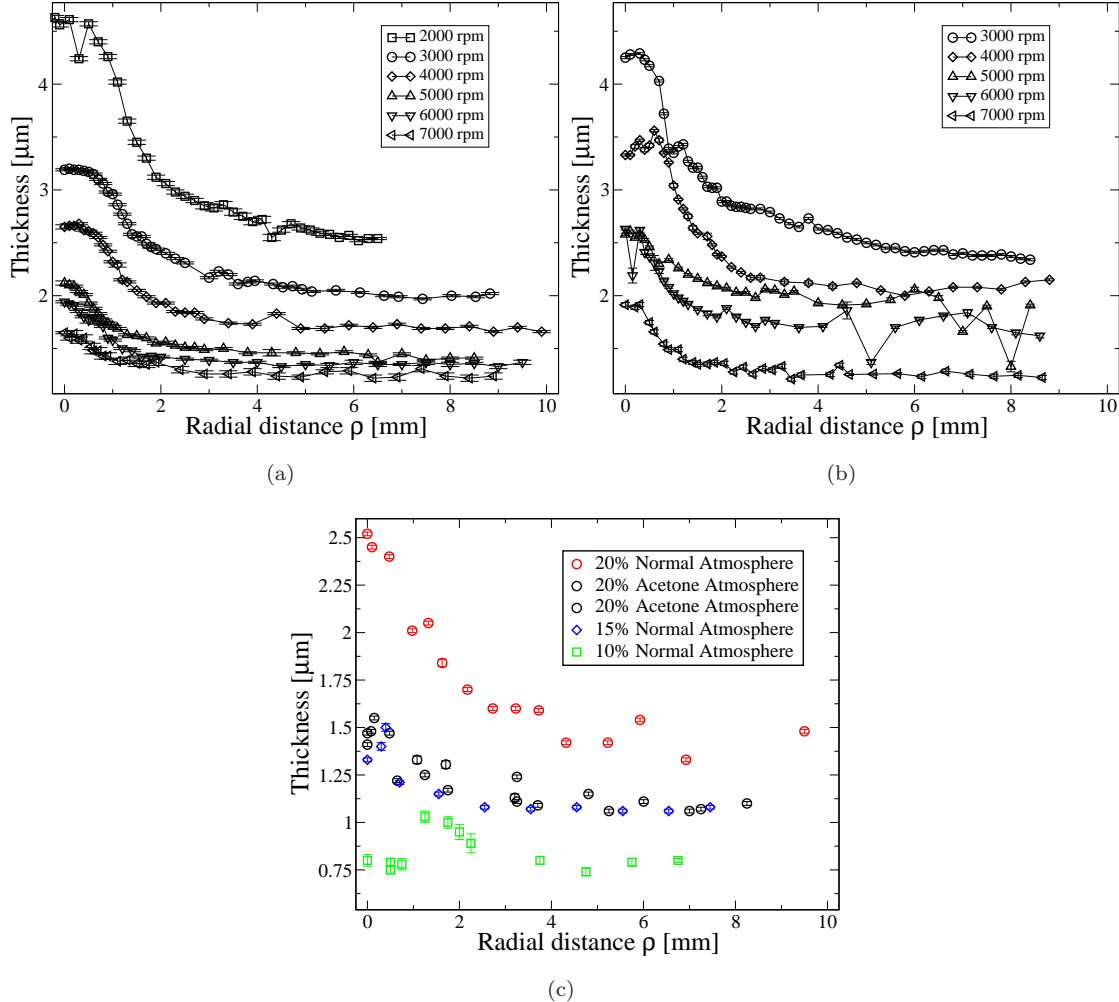


Figure 7.1: Dried thickness profiles. (a) Profiles at different rotation rates for 20% MEK suspensions. (b) Profiles at different rotation rates for 20% acetone suspensions. (c) Profiles for films obtained from acetone suspension at different initial concentration (colour) and at saturated acetone atmosphere (black).

7.2. Dynamics of thinning

The lighting configuration B (Figure 6.1, section 6) allowed us to visualise interference rings related to the thickness changes on the fluid surface (with respect to the substrate). Figure 7.2 shows a sequence of frames for a typical experiment. Initially, Ekman spirals formed while the suspension was pipetted over the rotating substrate and accelerated by it (see Figure 7.2, $t=0.07$ s). These heterogeneities rapidly disappeared, once pipetting ceased, and axisymmetric rings become visible ($t=0.21$ s and later, Figure 7.2).

A first remark to be made is that the distance between rings is shorter as we get closer to the centre, even at the early stages of the experiments ($t=0.14$ s in Figure 7.2). This imply that the thickness of the fluid film has a radial dependence. We calculated the thickness profiles of the fluid film by measuring the distance between consecutive rings at different times. Considering the Newton's rings scaling (equation 6.1, in section 6) we obtained the profiles for the spinning suspension (see Figure 7.3(a) and (b) for two experiments at 7000 and 4000 rpm). Interference pattern allows us to access the thickness profile but, we ignore the order of interference needed to determine the absolute thickness. Nevertheless, we could establish a limited region where the fluid data is compatible with the dried one. To do this, we considered a situation where the suspension was fluid in the centre (and presented interference rings) and dried in the outer region. In the outer area the thickness was the dried one measured with the AFM (plus symbol in Figure 7.3(a)). Thus, we create sets of data, matching the fluid points (with different offsets in the vertical direction) and the outer dried points (without an offset). An example of such ensemble is the curve with triangular symbols Δ at $\tau=-14$ rad in Figure 7.3(a). Then, we fitted the different sets with an heuristic bell-like function ($A + B/(1 + (C/\rho)^2)$) and selected the two limit cases where the fitting did not reproduce the data ensemble. This procedure gave an uncertainty of $\sim 1 \mu\text{m}$ in the absolute location of the fluid thickness profiles but still allows to reasonably locate the fluid profiles with respect to the dried ones.

We measured the thinning rate evolution by measuring the frequency at which the interference rings went through a fix radial distance. This is conceptually equivalent to laser-based measures commonly used in pure fluids and polymers [82, 83]. In our case, we accessed to the thinning rate in the whole surface of the substrate instead of one point. Again, the Newton's ring scaling gives the thinning rate from the frequency measures (d calculated from equation 6.1). For each experiment we measured the frequency on three points at different radial distances (from 1 to 5 mm) for as long as the rings were discernible. Scaling of the data to dimensionless times led to a collapse of all points (for every radial position, time and substrate rotation rate, as shown in figure 7.4).

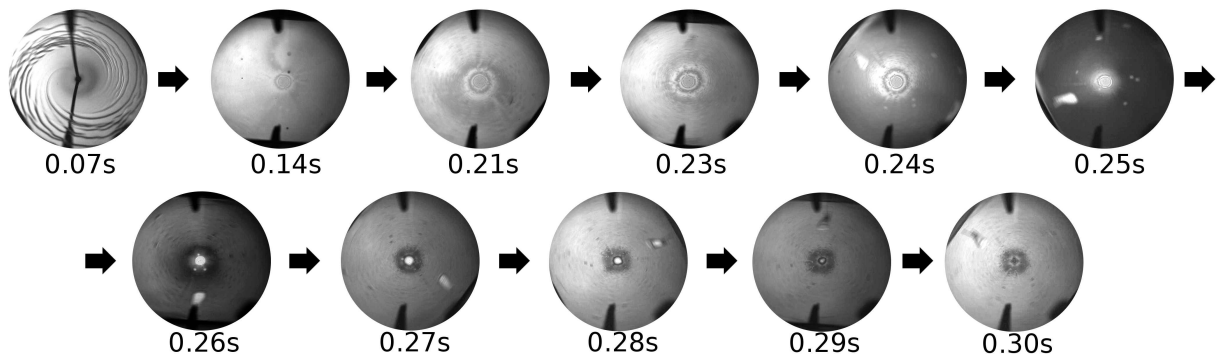


Figure 7.2: Typical sequence observed using lighting configuration B (Figure 6.1). In the first image we observe Ekman spirals that appear during pipetting. Milliseconds after pipetting ceased, heterogeneous alternating dark and bright bands became visible (0.14s frame, in the outer area). The bands took a concentric ring symmetry after a few milliseconds, when the initial heterogeneities dissipated, and they remain until the final drying of the suspension.

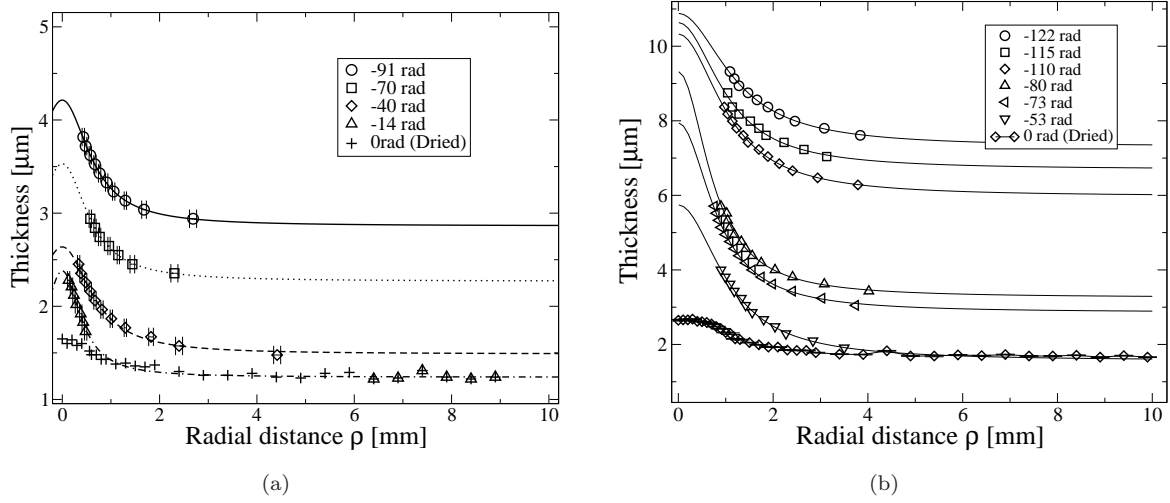


Figure 7.3: Thickness profiles in the fluid phase. (a) Profile at $\tau = -14$ rad (Δ set) is an ensemble of fluid points ($\rho < 1$ mm) and dried points ($\rho \sim 6$ to 9 mm). These kind of ensemble was used to properly locate the absolute thickness on the fluid stage (details in text). (b) Profile for 4000 rpm experiment. Lines, that correspond to fits to $A + B/(1 + (C/\rho)^2)$, are only for visual guidance.

We finally fitted the scaled thinning rate to the equation:

$$-dh/d\tau = \begin{cases} (0.5\alpha h_0)/(1 + \alpha(\tau - \tau_0))^{1.5} + \epsilon & \text{if } \tau < 0 \\ 0 & \text{if } \tau \geq 0 \end{cases} \quad (7.2)$$

This equation is originally inspired in the classical analysis made by Emslie *et al.* [9] for non-evaporative fluids and, later, extended by Meyerhofer [10] to volatile ones. In the next chapter, we will make a detailed deduction of this formula, its implications and differences with the standard approach.

7.3. Dynamics of long range orientational order

The bright arms, that were firstly observed in the dried polycrystals, were also found on the fluid phase. Using the lighting setup A (Figure 6.1, section 6) we observed the long range orientational order in either stage (dried or fluid). In Figure 7.5, we qualitatively show the typical sequence that was identified during the crystallisation process. We found five generic phases common to all experiments:

Phase I (pouring) Initial transient state, characterised by Ekman spirals while the suspension is pipetted onto the rotating substrate (Figure 7.5 a).

Phase II (six-fold) Six arms become clearly visible, initially broad and localised in the centre of rotation but within a few milliseconds they expand over the whole area of the substrate. Simultaneously, the arms became thinner and well defined (Figure 7.5 b).

Phase III (symmetry transition) The 6-fold symmetry goes to a 4-fold one. It starts in the centre and, in few milliseconds, the new symmetry expands over the substrate (Figure 7.5 c).

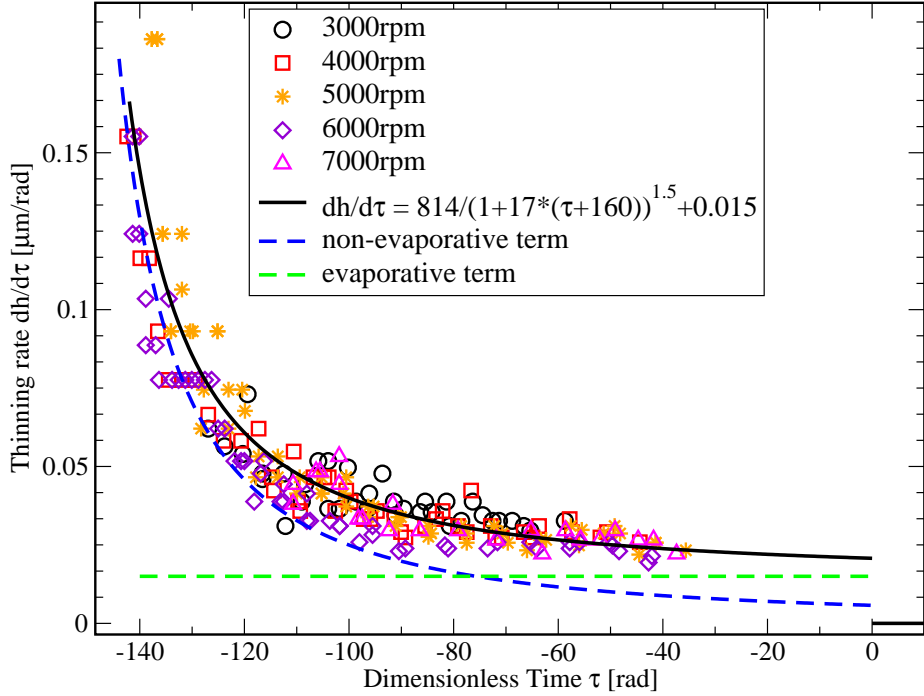


Figure 7.4: Scaled thinning rate, extracted from Newton's ring frequency, *vs.* dimensionless time. The red line comes from the fit of equation 7.2. Points correspond to different radial distances, rotation rates and time. Dashed lines are the two terms of this equation plotted separately. The non-evaporative term is the τ dependent element of the sum. The evaporative term is the constant $\epsilon=0.015 \mu\text{m}/\text{rad}$.

Phase IV (order disappearance) The arms disappear in the outer area of the substrate and the four-fold symmetry shrinks towards the centre where it was previously originated (Figure 7.5 d).

Phase V (drying) The outer area, where the order had been lost, starts to dry. This defines a circular perimeter which reduces as the remaining fluid evaporates. As the structure dries, arms appear again visible with a symmetry that depends on the experimental conditions (Figure 7.5 e, f).

While the phases that involved the fluid suspensions are common for all experiments, we observe that the dried structure can take one of two different states (Figure 7.5 f) characterised by the symmetry in the outer region. While in the centre is always 4-fold, in the outer region most of the experiments gave 4-arms symmetry but, as the films became thinner (either by increase of rotation rate or decreasing of initial concentration), the structure consistently changed to a 6-fold symmetry. As reported previously [35], these two symmetries were correlated with a microscopic arrangement of the top layer: square structures with 4-arms and hexagonal ones in 6-arms areas (confirmed *via* SEM imaging of the top surface).

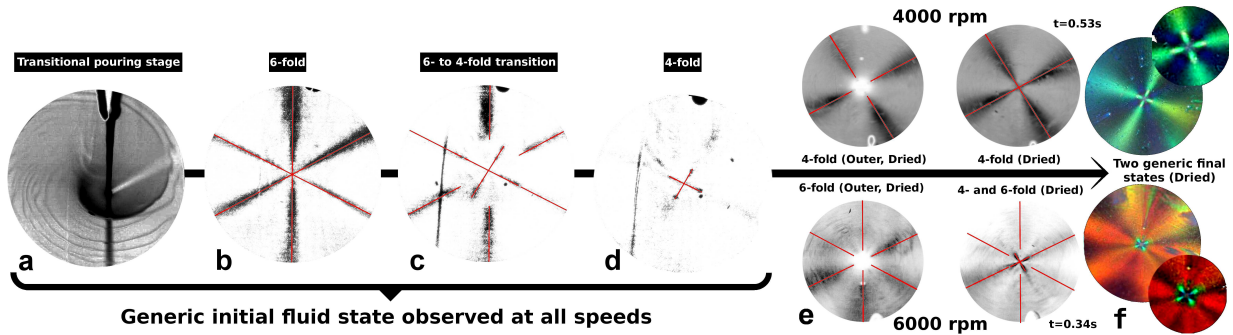


Figure 7.5: A sequence that illustrates the typical dynamics on the long range order. (a)-*Phase I*- The suspension is pipetted onto the rotating substrate, Ekman spirals appear as the fluid is accelerated. (b)-*Phase II*- As pipetting ceased the spirals disappeared, and 6-arms appear clearly contrasted against the background. They initially locate in the centre but rapidly expand over the surface. (c)-*Phase III*- The symmetry changes to a 4-fold structure, again starting in the centre but rapidly expanding over the substrate. (d)-*Phase IV*- This new structure is lost. Initially this occurs in the outer region but, it progressively grows toward the centre as the 4-arms shrink. (e)-*Phase V*- The drying starts on the periphery, evidenced by a large change in the contrast due to the exchange in the refraction index (from MEK or acetone to air). (f) As the structure dries bright arms appear again, which is the final permanent structure. While the dynamical fluid stages are qualitatively identical in all experiments, the dried structure can take one of two states distinguished by their external symmetry: 4-fold at low angular speeds or high concentration (top right, 20%, 4000rpm, MEK solvent) and 6-fold at high angular speeds or low concentration (bottom right, 20%, 6000rpm, MEK solvent). The red lines overlapped are guides for the eye. Snapshots were digitally enhanced to improve visualisation.

7.4. Dynamics of the drying front

The transition from the fluid suspension to the dried structure is clearly visualised through any lighting setup (see Figures 7.2 and 7.5). This is a consequence of the sudden change in the refractive index as the structure dries and the dispersive medium (acetone or MEK) is replaced by air. In all cases, the front presents a circular shape and it progresses from the outer edges, where it is firstly dried, towards the centre. The analysis was carried out as described in section 6 for images taken in configuration B (figure 6.1). In Figure 7.6(a) we show the position of the drying front as function of dimensionless time (scaled using equation 7.1). In all cases, two regimes are clearly identified where the velocity of the drying front is different. Far from the centre, the front moves rapidly with a dynamical behaviour that depends on the rotation rate, while, near the centre, the dynamics appears independent of the rotation rate. In Figure 7.6(c), we plot the asymptotic slopes of the curves in Figure 7.6(a), and we observe that the inner dynamics is largely independent from the rotation rate, while the outer one is not. We extrapolated these asymptotes, and defined the crossover between both lines as the coordinates at which the transitions occur (see Figure 7.6(d)). From this figure, we observe that an increase of rotation rate drives the transition closer to the centre and later in time.

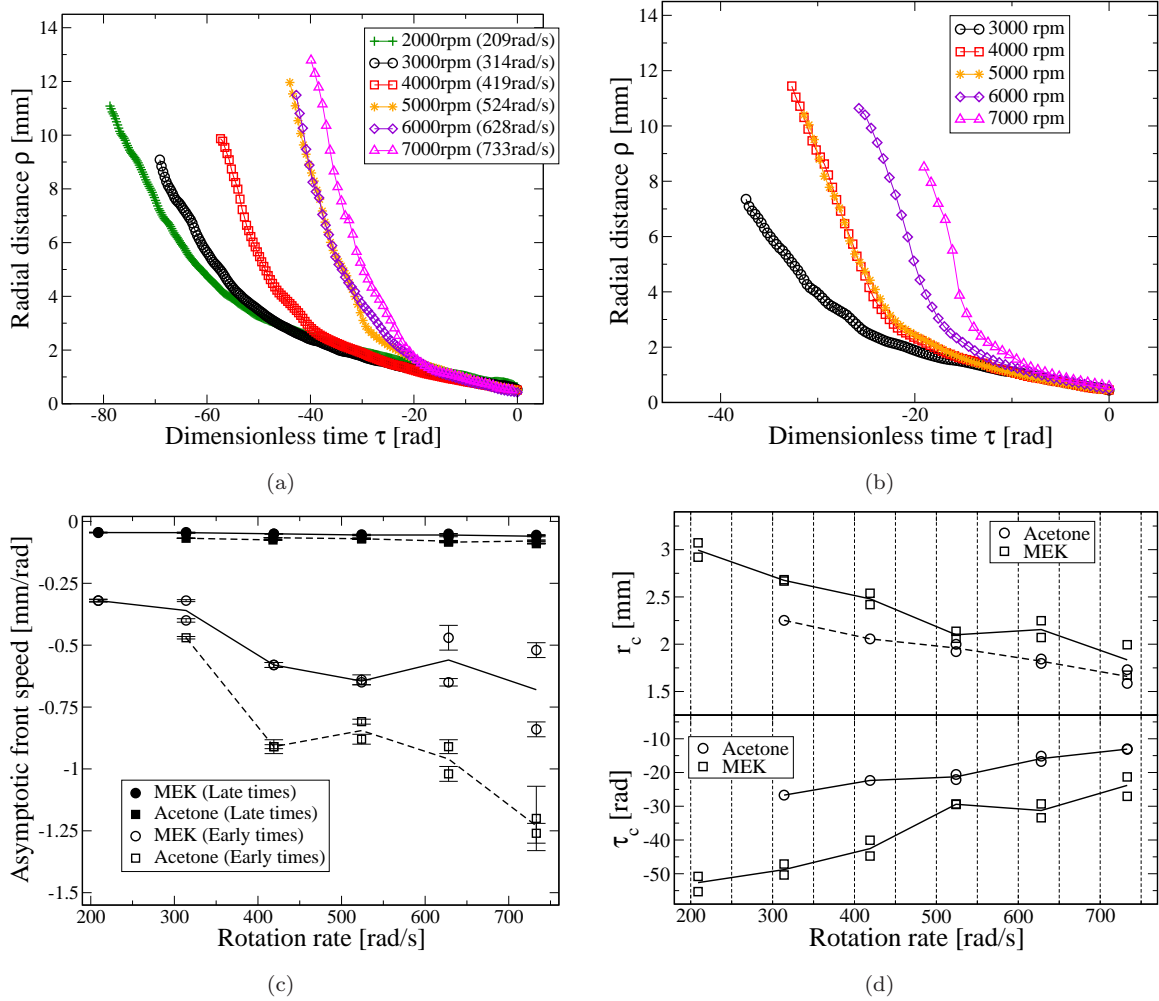


Figure 7.6: Drying front dynamics. (a) Position of the drying front *vs.* τ for MEK experiments. (b) Position of the drying front *vs.* τ for acetone experiments. (c) Asymptotic slopes calculated for early and late times. (d) Crossover of the asymptotic behaviour shows the evolution of the position of the transition as a function of the rotation rate.

7.5. Arms definition in the dried substrate

Figure 7.7(a) shows a typical sequence of samples obtained at different rotation rates. In this sequence, the rotation rate increases from the left to the right of the image. In addition to the number of arms in the sample, there is a difference in the morphology of the arms between the region near the centre and far from it (see Detail in Figure 7.7(b)). These series of transitions are limited by two extreme cases. The lower extreme was obtained with suspensions at very low concentration (5% volume fraction), where we did not find well defined arms. The upper extreme is obtained with low rotation rates and high concentration suspension (2000~3000 rpm and 20~40%). Here, we found a well defined four arms star (Figure 7.7(b)(I)) covering large areas of the substrate. In the intermediate cases we found a clear distinction between the inner and the outer arms. The radial position of the transition between the inner and outer regions reduces as the rotation rate increases, at a fix concentration, or as the concentration decreases,

at fix rotation rate (Figure 7.7(a) and 7.7(c)).

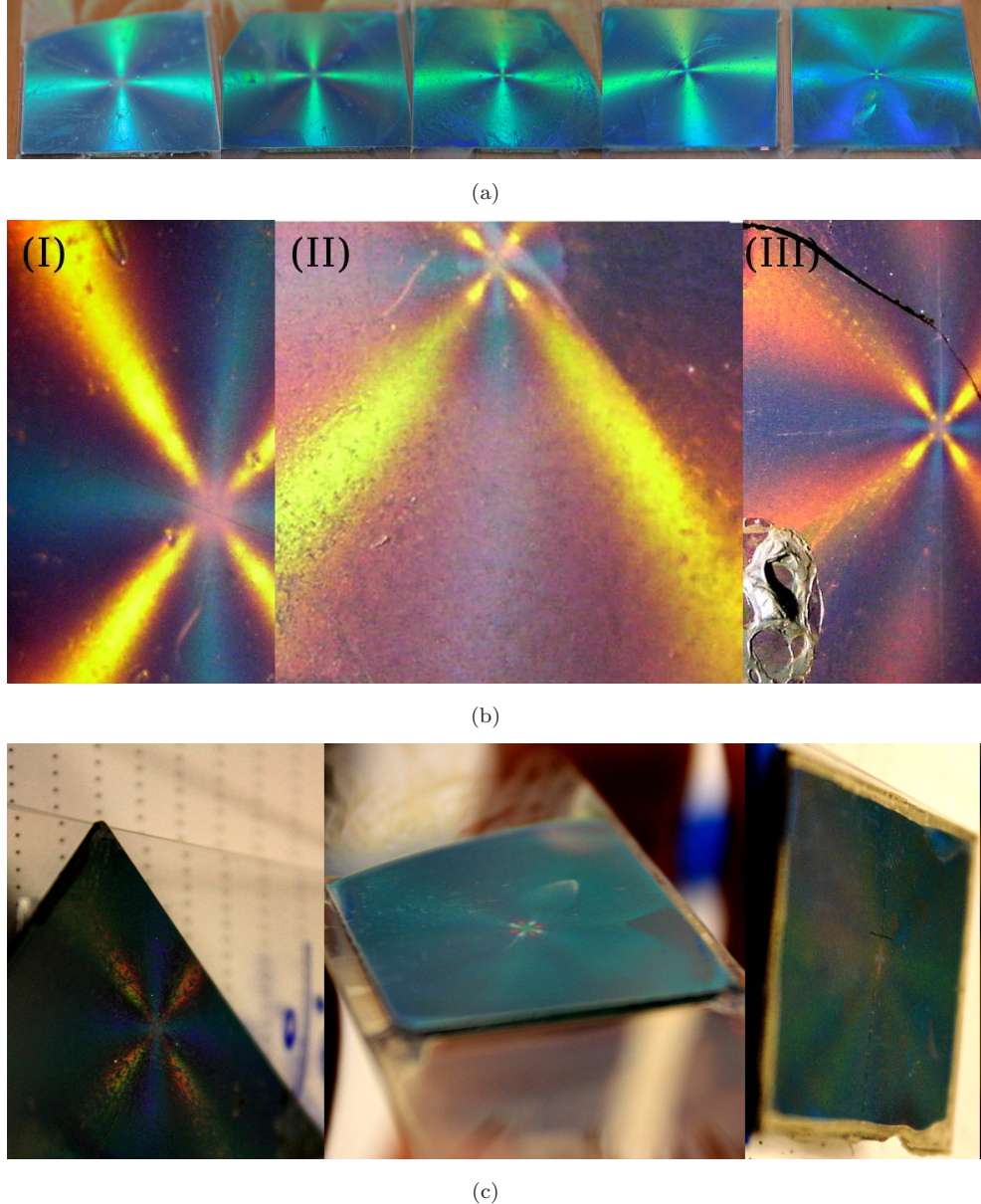


Figure 7.7: Colour images of the arms taken in a back scattering setup (light source is the built-in flash of the camera). (a) Typical stars found in evaporative spin-coating, samples are ordered from left to right as increasing rotation rate used (3000, 4000, 5000, 6000 and 7000 rpm). The rotation rate of the substrate was the only parameter varied on this sequence. (b) Detail of the distinct arms morphologies is evident from the images. All samples were made with 20% MEK suspensions. (I) 4-fold well defined arms that cover most of the surface of the substrate, observed at very low rotation rates. (II) inner and outer 4-fold from a 5000 rpm sample. (III) inner 4-fold, outer 6-fold obtained at 7000rpm. In the last two cases, the inner arms are bright and sharp while, the outer ones are diffuse. (c) Sequence of acetone samples at different initial concentration, from left to right: 20%, 15% and 10%, all images are at the same scale.

Chapter 8

Discussion

8.1. Model for spin-coating of evaporative fluids

In the introduction we presented a detailed deduction of Emslie *et al.* [9] equation for a viscous fluid thinning on a rotating disk. Also, we briefly introduce Meyerhofer modification for taking into account a volatile fluid in equation 5.7. In this approach, a constant is added to the thinning rate as a function of thickness. With this inclusion is not possible to recover an explicit expression for the thinning rate. We will show that Meyerhofer equation is an approximation for low volatile fluids and that it is possible to extend Emslie model to low and high volatile fluids while retaining an explicit expression for the thinning rate.

In the Meyerhofer equation, it is necessary to know the absolute thickness of the fluid at each time. This is generally unknown, since the standard approach to measure the thinning implies the use of laser interference for which the order of interference is unknown. In general, it is possible to estimate the absolute thickness, either by measuring the final thickness of the deposit or using it as a fitting parameter [42, 82]. Nevertheless, the actual measure is the temporal evolution of the thinning rate, that typically is seen as an oscillatory signal with a period which becomes longer as the fluid dries (see [82, 83] for some examples). In our case, the absolute fluid thickness profiles have a systematic error of the order of 1 μm . Therefore, we would like to avoid a fitting to Meyerhofer formula. Additionally, we obtained an excellent fit of the temporal evolution of the thinning rate (Figure 7.4). For the fitting we used the temporal evolution for a non-volatile fluid (obtained in [9]) plus a constant value that accounts for the evaporation contribution. Based on this experimental observation, we reconsider how to incorporate the effect of evaporation on the model. Now, we will derive a model that gives an exact expression for the thinning rate in evaporative fluids.

We start with Emslie temporal equation 5.6 for the thickness:

$$h^{n-e} = \frac{1}{\left(\frac{4}{3\nu}\tau + C_3^t\right)^{0.5}} \quad (8.1)$$

here, we rewrote the thickness as h^{n-e} to stress out that, in the model, there is only the contribution of non-evaporative thinning. In our measures we have both effects: evaporative and non-evaporative. We will assume that these two phenomena are decoupled and that the total

thickness, at a given time, can be expressed as:

$$h^e = h^{n-e} - \epsilon t/A \quad (8.2)$$

Here, h^e is the thickness that we actually measure in the experiment, h^{n-e} is the non-evaporative term (in our simple consideration it will be given by equation 8.1) and ϵ/A is the evaporative term (evaporation rate divided by the area of the free surface of the fluid). This last term is negative since positive evaporation rates produce a decrease on the thickness (negative evaporation rates will indicate vapour condensation on the surface [105]). Now, we can replace the h^{n-e} in equation 8.1 for its equivalent as a function of the measured thickness and the evaporation rate.

$$h^e + \tilde{\epsilon}\tau = \frac{1}{\left(\frac{4}{3\tilde{\nu}}\tau + C_3^\dagger\right)^{0.5}} \quad (8.3)$$

here, we multiplied the evaporative term by $\omega/\omega = 1$ to maintain coherence with the rest of the formula: $(\epsilon t/A)\omega/\omega = (t\omega)\epsilon/(A\omega) = \tilde{\epsilon}\tau$. Now, we can isolate h and derive with respect to τ , in order to obtain the thinning rate:

$$h^e = \frac{1}{\left(\frac{4}{3\tilde{\nu}}\tau + C_3^\dagger\right)^{0.5}} - \tilde{\epsilon}\tau \quad (8.4)$$

$$\frac{\partial h^e}{\partial \tau} = -\frac{\frac{-1}{2}\frac{4}{3\tilde{\nu}}}{\left(\frac{4}{3\tilde{\nu}}\tau + C_3^\dagger\right)^{1.5}} - \tilde{\epsilon} \quad (8.5)$$

$$\frac{\partial h^e}{\partial \tau} = -\frac{1}{\left(\left(\frac{3\tilde{\nu}}{2}\right)^{2/3}\frac{4}{3\tilde{\nu}}\tau + C_3^*\right)^{1.5}} - \tilde{\epsilon} \quad (8.6)$$

$$\frac{\partial h^e}{\partial \tau} = -\frac{1}{\left(\left(\frac{1.75}{\tilde{\nu}^{1/3}}\tau + C_3^*\right)^{1.5}\right)} - \tilde{\epsilon} \quad (8.7)$$

$$\frac{\partial h^e}{\partial \tau} = -\frac{1}{\left(\left(\frac{1.75}{\tilde{\nu}^{1/3}}(\tau + \tau_0) + C_3^*\right)^{1.5}\right)} - \tilde{\epsilon} \quad (8.8)$$

where $C_3^* = (3\tilde{\nu}/2)^{2/3}C_3^\dagger$. In the last expression (equation 8.8), we included a displacement τ_0 in the dimensionless time. This displacement is necessary to compare with the formula fitted since, in our measures of the thinning rate, the time was scaled to $\tau = \omega(t - t_0)$. Thus, this final expression is of the same form as the one used to fit the experimental thinning rate (equation 7.2, Figure 7.4):

$$\frac{\partial h^{ev}}{\partial \tau} = -\frac{1}{\left(0.19(\tau + 160) + 0.011\right)^{1.5}} - 0.015 \text{ } \mu\text{m} \quad (8.9)$$

Comparing the corresponding terms, we can determine the different estimates for the parameters:

$$\begin{aligned}\frac{\epsilon}{A\omega} &= \tilde{\epsilon} = 0.015 \text{ } \mu\text{m} \Rightarrow \epsilon = 7 \cdot 10^{-3} \omega \text{ } \mu\text{L} \\ \epsilon &\sim [1, 5] \text{ } \mu\text{L/s} \\ \frac{1.75}{\tilde{\nu}^{1/3}} &= 0.19 \text{ } \mu\text{m}^{-2/3} \Rightarrow \nu = 781 \cdot 10^{-12} \omega \text{ m}^2 \\ \nu &\sim [10^{-7}, 6 \cdot 10^{-7}] \text{ m}^2/\text{s} \\ C_3^* &= 0.011 \text{ } \mu\text{m}^{-2/3}\end{aligned}$$

Here, we used $A = \pi r^2$ and $r = 12.5$ mm. From this comparison we observe that the evaporation rate depends linearly with the rotation rate ω , and its value is of the order of $1 \text{ } \mu\text{L/s}$. The kinematic viscosity ν is of the same order of magnitude that the kinematic viscosity of pure MEK ($5 \cdot 10^{-7} \text{ m}^2/\text{s}$).

From this model we distinguish two regimes, one non-evaporative and one evaporative. The former is dominated by radial flows, while in the latter flows are mainly in the vertical direction. Also, while in the first regime the flows carry particles and fluid away from the rotating substrate, in the second regime is mainly fluid phase that is lost. Thus, the final dried thickness, that is determined by the solid phase (i.e. particles), is mostly determined by the time at which the evaporative regime starts to dominate the dynamics. This explains the thicker deposits observed for acetone. This fluid has a higher evaporation rate than MEK, while the other physical properties remain similar. Therefore, we expect that the non-evaporative dynamics that represents this process is the same than the one plotted in Figure 7.4 but with a larger evaporative term. Hence, the transition occurs at earlier times and the final thickness is larger than in MEK experiments.

If we consider the thickness for the case of the lower concentration suspensions, we expect that the dynamics will remain unchanged since the 20% experiment are represented by a fluid model, this also should occur in less concentrated suspensions. Nevertheless, as the concentration is smaller than in the previous cases we would expect a decrease in the thickness as is observed in Figure 7.1(c). This can be understood if we consider that the dynamics (from non-evaporative to evaporative) also produce a change in the flows geometry. As considered before, in the non-evaporative regime the flows are radially outward, thus fluid and solid phase is expelled. In the non-evaporative regime flows will tend to shift towards the vertical direction, thus there will be a decrease in the fluid phase but no in the solid one. The volume lost in the non-evaporative phase will remain constant despite the change in concentration, but the solid phase will decrease as a result of the lower concentration. We compare the relative change of volume of the dried structure in the different conditions. From Figure 7.1(c) we estimated that a reduction of 25 and 50% of the initial concentration results in a decrease of 31% and 50% of the mean thickness which is consistent with the flow geometries depicted before.

We presented radial thickness profiles for the dried substrate obtained in an atmosphere saturated with acetone (recall Figure 7.1(c)). There, we saw that the thickness profiles for increasing the vapour pressure of acetone gives a very similar result than for decreasing the initial concentration from 20% to 15%. The effect of increasing the vapour pressure of acetone is to reduce the effective evaporation rate of the suspension and, then, the non-evaporative regime extends to later times and the final thickness reduces.

8.2. Evaporation rate during final drying

When the suspension concentrates enough, it cannot be considered as a simple fluid. In this situation, evaporation takes place through the pores of the structure. Eventually, the structure dries and a drying front forms in the region of transition from the fluid suspension to the dried structure. At this point, the fluid is confined to smaller radii than the drying front position (see Figure 7.6), and it wets the previously deposited porous structure. Then, if we consider the fluid enclosed by the circular perimeter defined by the drying front, the volume of fluid can change due to two different mechanisms: evaporation that takes place on the upper surface or, capillary flows that carry fluid to the structure outside the perimeter. These two contributions have different radial behaviour. Evaporation depends on the exposed surface (A_e on Figure 8.1(a)). Thus, it behaves as ρ^2 . However, capillary flows depend on the compactness of the deposited structure and the wetting properties of the particles. Nevertheless, if we assume that these parameters remain constant, the capillary flows only depend on the area at which they circulate, i.e. A_{df} in Figure 8.1(a). From Figure 7.3, we see that $dh/d\rho$ has a maximum value of 10^{-3} , consequently, the change in volume in the fluid phase due to capillary forces should be proportional to ρ .

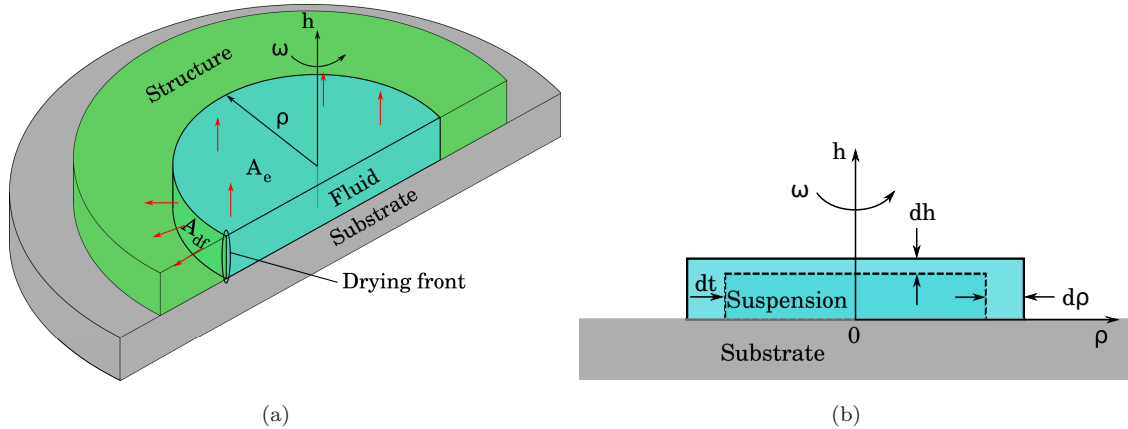


Figure 8.1: Schematic representation of the effect of drying over the dimensions of the idealised cylinder. A change of dt gives a change of dh and $d\rho$.

The small dh to $d\rho$ ratio indicates that a straight cylinder is a good approximation for the fluid shape. In Figure 8.1(b) we sketched such a cylinder that, in a time dt , shrinks a volume dV (represented by a change dh and $d\rho$). We can geometrically estimate the change in the volume as:

$$dV/dt = 2\pi\rho(d\rho/dt) h + \pi\rho^2(dh/dt) \quad (8.10)$$

In this expression, the overlapping volume $2\pi \times \rho \times dh \times d\rho$ will be counted twice but, it is small enough to be neglected at a first approximation level. The exact values of most of the quantities involved at the time of drying are inaccessible to our experimental setup. Nevertheless, we can give an approximate value for each term from our experimental data:

- $d\rho/dt$ from the asymptotes in the early and late times (Figure 7.6).
- h at the moment of drying, can be estimated from the dried thickness profiles in Figure 7.1.

- we estimate an upper limit for dh/dt from Figure 7.3 by considering the value of the fitting function at time $\tau = -40$ rad.

With these values in consideration we obtained the evaporation rate dV/dt as a function of the radial position of the drying front that is plotted on figure 8.8. On the left, we show the estimation for large radial distances overlapped with fittings to a linear and a quadratic function (red and green, respectively). On the right, we plotted the corresponding dV/dt for small radius (linear fit in red).

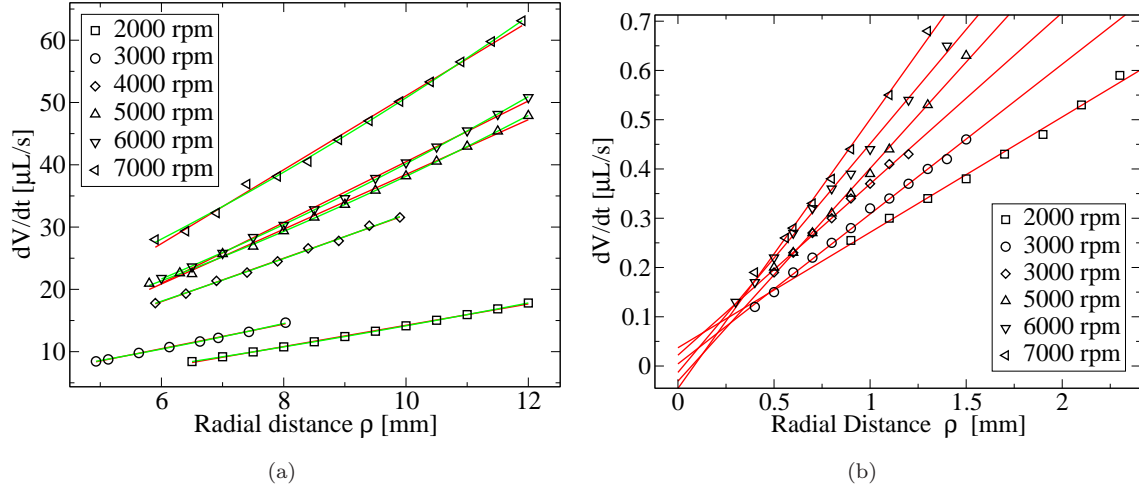


Figure 8.2: Evaporation rate during final drying. (a) Far from the centre. (b) Near the centre. Empty points were calculated from experimental data using equation 8.10, red and green curves are linear and quadratic fitting respectively.

The departure from linearity is too weak to prefer a quadratic fit to a linear one. However, it can be seen that this departure is higher at large rotation rates and at radial distances far from the centre (see Figure 8.2(a)). Also, it is for these high rotation rates experiments, that we observed a transition from 4 to 6 arms in the dried structure. This observation is in agreement with argument presented by Vermolen [41] that the transition to 6 arms occurs when the flows induced by evaporation become relevant with respect to capillary flows. This picture is also valid if we consider the thickness of the structure: a thicker structure has larger capillary flows (since A_{df} in Figure 8.1(a) is larger). The increase of the rotation rate reduces the thickness of the structure, hence, evaporation flows gain relevance with respect to capillary flows. Additionally, at higher rotation speeds, the evaporation rate increases (recall that, in the previous section, we found that $\epsilon \sim \omega$).

8.3. Order in the fluid phase

In the fluid phase, we observe a common dynamics for all experimental conditions. From Ackerson experiments with nearly hard sphere systems [14, 17], we know the existence of phase transitions, when such system is subjected to steady or oscillatory shearing, as a function of the shear rate and concentration. In our experiments, at early times (large negative dimensionless times), the spin-coating dynamics is governed by radial outgoing flows. This situation is similar

to Ackersons' shearing experiments, where he found always a fcc lattice parallel to the substrate plane. Thus, it is likely that the shear-induced flows are responsible of the six-fold order observed at the initial stages of the spin-coating process.

At later times, we observe a transition to a 4-fold structure. There is no equivalent arrangement reported in any of the hard sphere shearing experiments [106–109] or non-evaporative spin-coating crystallisation experiments [40]. The main difference in our experiment is the use of a highly volatile fluid. Hence, we expect that the new symmetry could be related to the presence of high evaporation rates.

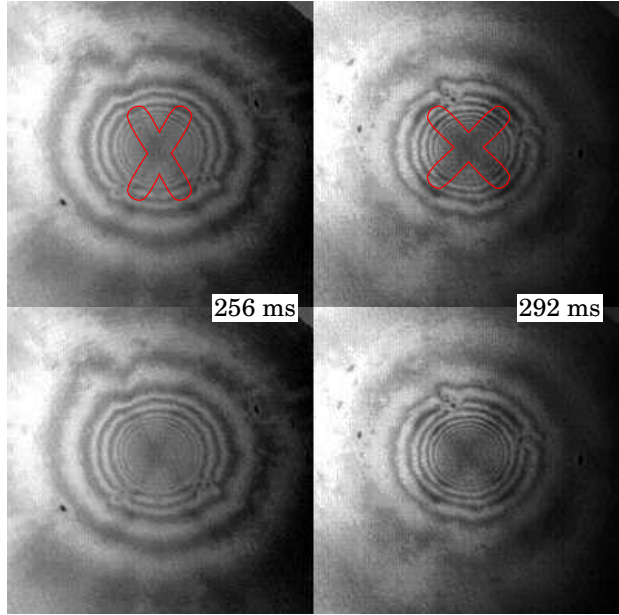


Figure 8.3: Two snapshots of the fluid thinning measures. Top and bottom are the same set of images, in the top set we highlight the arms observed on the bottom images. These correspond to an experiment at 4000 rpm and represent the transition from a fluid 6-arms to a 4-arms symmetry. Times shown are non scaled ones.

To test this hypothesis we observed again the videos captured on the lighting configuration B (Figure 6.1). In Figure 8.3 we show two snapshots for an experiment done at 4000 rpm, with 20% initial concentration and MEK as fluid phase. The top and bottom images are the same, in the top ones we highlighted the arms that are difficult to observe in the low contrast original images (bottom). This sequence illustrates the transition from the initial 6-fold phase to the 4-fold stage. We measured the time at which this transition occurs, for the different experiments. As the experiments were the same that we used to measure the thinning rate (recall Figure 7.3) we can compare this times with the time at which the non-evaporative and evaporative term cross (≈ -80 rad). This comparison is shown on Figure 8.4 for the scaled time.

The transition from a non-evaporative to an evaporative dynamics corresponds well with the transition from 6- to 4-fold in the fluid phase. This is a strong indication that the two phenomena are closely related. Additionally, towards the end of section 8.1 we observed that the two regimes could be associated with different flows geometries. This could indicate that the change in flow geometry is responsible of the transition from a 6-fold to a 4-fold symmetry.

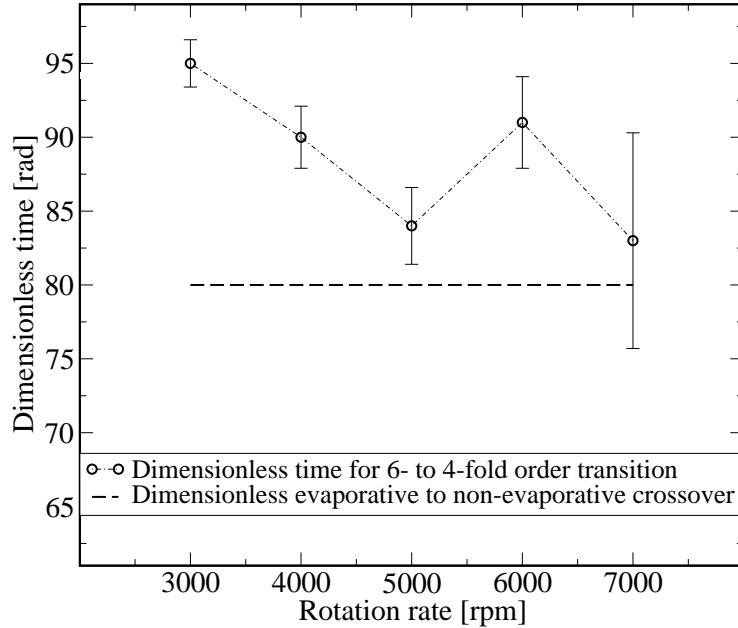


Figure 8.4: Fluid transition from 4- to 6- arms. Comparison of the scaled time of the fluid transition with the temporal crossover between non-evaporative and evaporative terms from equation 8.8.

Additionally, as the evaporation gains relevance, respect to the radial flows, the concentration of the suspension increases and, the inter-particle separation decreases. The process of shear induced melting has been thought to be related to fluctuations in the particle position (with respect to the particle inter-spacing) since early 1980s [14]. It was recently showed by Derk *et al.* [87], that the structure melts when the shear induced fluctuations are of the order of 12% of the inter-particle separation. In our case, the shear stress is changing as the concentration increases as well as the particle separation decreases. We could be in a situation where the system reaches the Lindemann criterion and melts before the structure starts to dry. This can explain the disappearance of the arms observed in Phase IV (Figure 7.5).

8.4. Order in the dried structure

Finally, we compared the position of the crossover in the drying front dynamics with the optical transition on the arms definition (Figures 7.6(d) and 7.7) and we found that the ratio between these two length scales is 2 ± 1 . The origin of the different morphology is not clear, it could be that the lower speed of the drying front gives more time to the particles to accommodate in the equilibrium well ordered structure (recall the phase diagram on section 5.2). While as the speed of the drying front increases, the local order of the structure decreases and, thus, the arm is more diffuse. This correspondence has a large uncertainty and need to be studied further to be clarified. A way to determine this would be to measure the local crystalline quality on the surface of the structure (via analysis of the SEM images). It is necessary to determine whether the broadening of the arms is due to a more disordered or to a more correlated structure. Both situation could contribute to the disappearance of the arms through the loss of the orientational correlation. In

the former case, it will be replaced by randomly correlated structures. In the latter, by large number of domains orientated in the same direction that results on a homogeneously coloured surface (hence, decreasing the arms definition).

A first consideration on this aspect can be done by estimating the capillary number Ca at the different regions. Consider the asymptotic front speed from Figure 7.6(c), here the speed of the drying front is around two orders of magnitude higher in early times than in later ones. We will take the viscosity and the surface tension to be 1 cP and 25 mN/m, respectively, and consider the velocity of the drying front 1 and 0.05 mm/rad at early and late times, respectively. Then, Ca will vary from around 10^{-3} to 10^{-4} . Even though, in both limits the viscous forces are important, the capillary forces will have a stronger effect at the lower limit. Therefore, we can establish that, when capillary forces are more relevant we encounter better defined arms. Additionally, a decrease in the role of the capillary forces, relative to viscous ones, is accompanied with a decrease in the definition of the arms.

In order to determine if the proportion of each symmetry (hexagonal and rectangular) is a determining factor to the appearance of the arms, we are developing a code to analyse the SEM images. The concept behind the procedure is to perform the complex demodulation of a signal [110]. In this case the signal is the SEM image of the structure. With the complex demodulation analysis we intend to recover the areas of the SEM image that contribute to a same region of the Fourier space. In one of our typical SEM image, there are many domains orientated in different directions thus the 2D-Fourier transform produces a ring of high intensity. The radius of the ring corresponds to the mean spatial frequency in the image, i.e. the mean distance between particles. In Figure 8.5 left we show a typical SEM image and, on the right, we present the Fourier transform of that image. The attempt of the program is, by performing the complex demodulation, recover the areas of the real space that are associated to a particular angle of the ring in the Fourier space. In figure 8.5 we highlight red areas in both images to exemplify our aim.

If we now displace the red circle following the ring, highlighted areas (red in Figure 8.5) will be turned off and new areas will be highlighted. This is represented in Figure 8.6 where we present a series of reconstructed images by filtering different angles of the ring (represented by the white number on each image). To obtain this images we have filtered a circular region in the Fourier space, centred on the ring. Then, we displaced this filtered region to the centre of the image and compute the inverse Fourier transform that provide a complex matrix with the information in the real space. Each image represent the modulus of the corresponding complex matrix. In this sequence, it is clear that some pairs of images are very similar: 10-100, 20-110, 30-120. The angle difference between these pairs is 90° which tell us that the structure corresponds well with a square symmetry. Additionally, that the angle difference between one image and the other is 10° (10-20-30) tells us that those domains are differently orientated, and that difference is 10° .

In the code, these frames are reconstructed every 2 degrees (not 10 as in the Figure 8.6), thus there is a smooth transition between one frame and the next. Then, the evolution of the grey intensity at each pixel of the reconstructed image has a series of peaks when the orientation of the filtered region coincide with one of the main directions of the structure in the image. An example of these plots is shown in Figure 8.7 for a situation with a square arrangement, since the peaks are separated by 90° degree.

We construct a similar plot for each pixel position and extract the position of the maxima. From the distance between maxima we assign the symmetry to the pixel (square if close to 90°

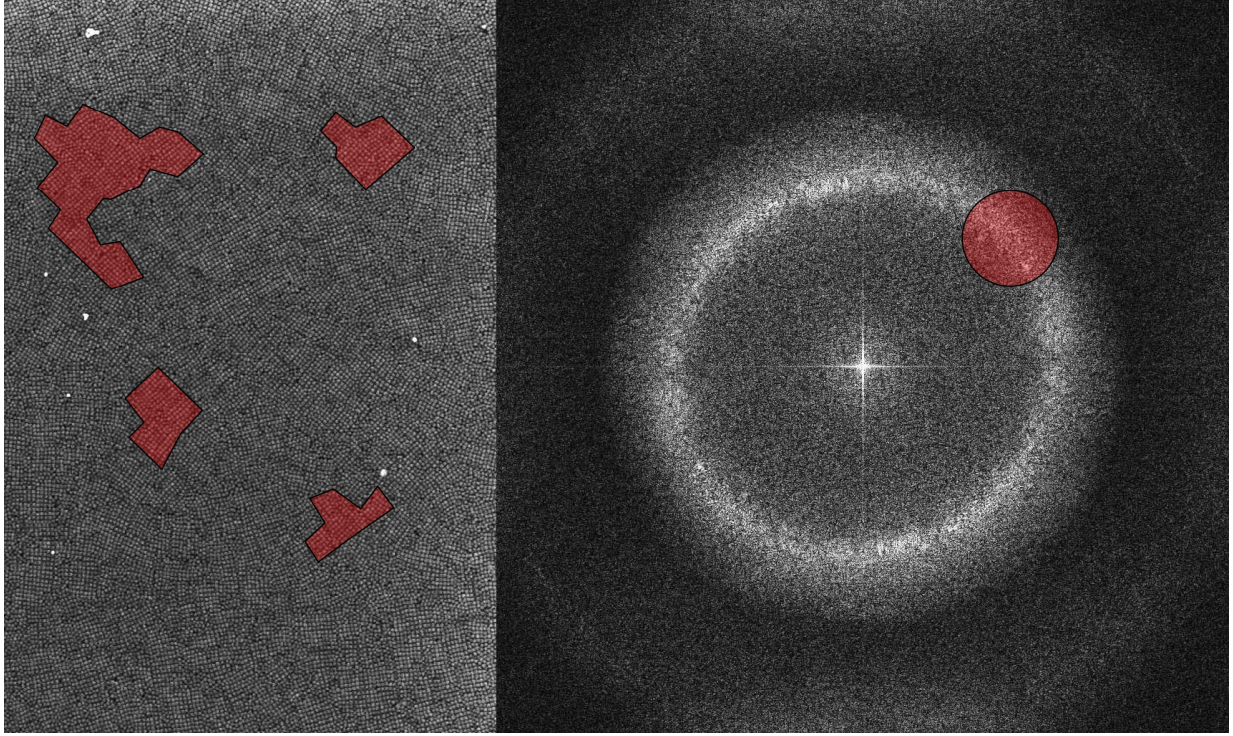


Figure 8.5: Left: typical low resolution SEM image of the deposits top layer. Right: Fourier transform of the image on the left. The red areas on the left image contribute largely to the red area in the Fourier image, since it coincides with one of the principal directions of the 2D order in the real space. Other areas of the real image might contribute to that region of the Fourier space but their contribution will be smaller since it will not coincide with the main direction of its local order.

and hexagonal if close to 60°).

If we now consider a series of SEM images taken at progressively larger distances from the centre of rotation we can evaluate the change on the symmetry with this distance. This is shown in Figure 8.8. In Figure 8.8(a) we present a 3D representation of the histogram for the square structure as a function of the radial distance. Here, we observe that the structure near the centre is not preferably orientated along any direction, we see this from the fact that the count of the histogram is roughly constant between -20° and 60° . as we move farther from the centre the count on the histogram increases around a particular angle decreasing in the surroundings. From Figure 8.8(b) we see that the maximum is not always at the same angle it start at small negative angle and as we go farther from the centre it shift towards a zero angle. This is an expected result since a zero angle indicates the radial direction. These results correspond to a highly concentrated suspension ($> 20\%$) at relative low rotation rate (3000 rpm). In this case, we observe bright well defined arms over the whole surface, except in the centre of rotation. Thus, this results appear to indicate that the definition of the arm is not related to the correlation of the orientation of the different crystals in the surface of the deposit at the scale considered in this analysis. Nevertheless, improvements of the analysis need to be done. At this point, the code does not identify properly the hexagonal arrangements. Thus, the parameters need to be adjusted to allow to distinguish

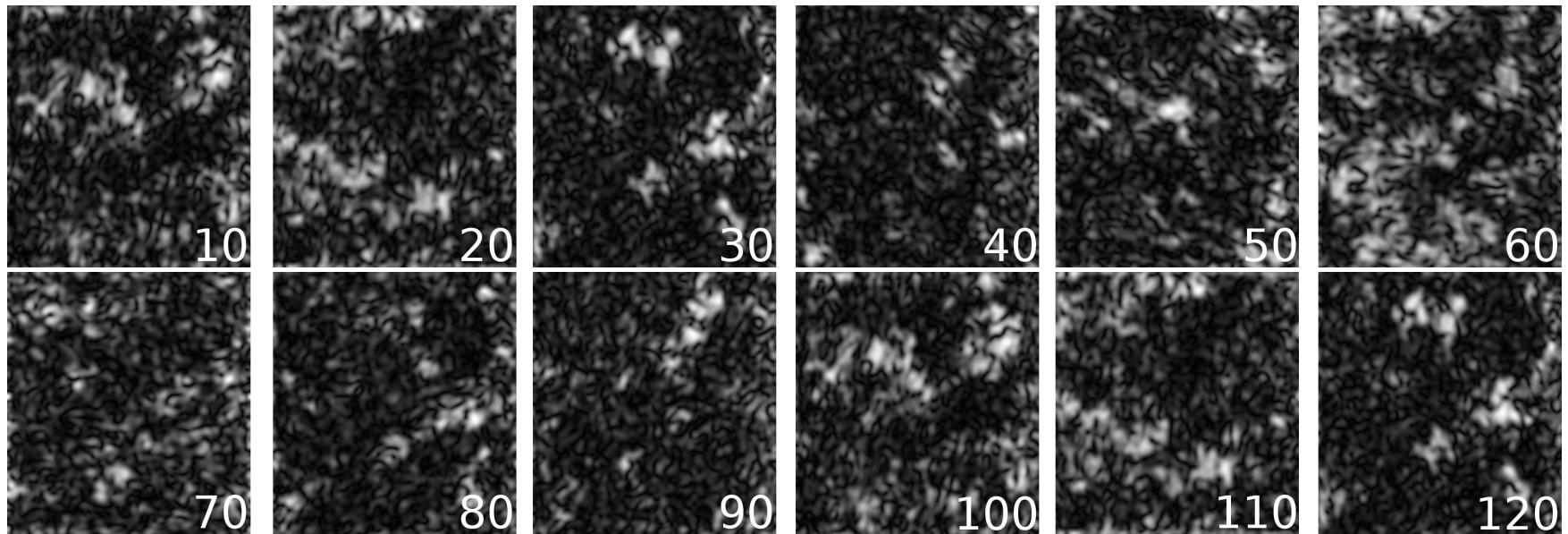


Figure 8.6: Amplitude images from the complex demodulation made at different angles (numbers overlaid in white on each image). A circular region is filtered from the Fourier space ring and translated to the centre of the image. Then the inverse Fourier transform is applied. The modulus of the resulting matrix is what we represented on these images.

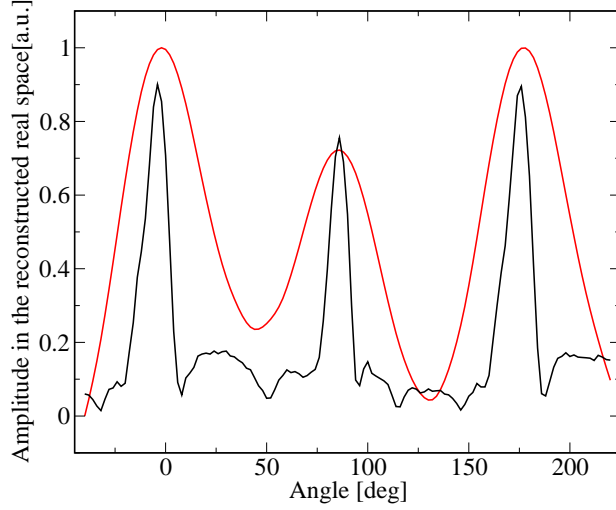


Figure 8.7: Plot of the evolution of the amplitude of the inverse Fourier transform for a single pixel. The data was scaled to allow comparison. This representation is equivalent to the image sequence like the one presented in Figure 8.6 considering a single pixel. We obtain a series of peaks corresponding to coincidence of the angle of the mask and one of the main orientation of the crystal around the pixel in consideration. Black: raw pixel evolution, Red: pixel evolution after convolution with a hamming window to smooth the curve.

between hexagonal and square symmetries to asses whether it is the proportion between these two structures that decides between defined and diffuse arms.

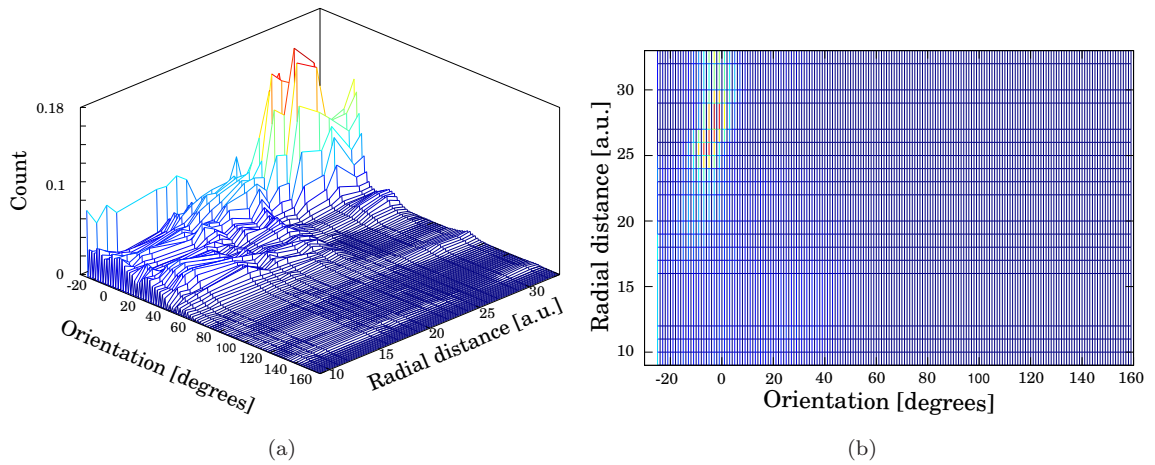


Figure 8.8: Preliminary results of the domain analysis for SEM images extracted from a large concentrated suspension ($> 20\%$) that presents four well defined arms over most of the surface on the substrate. The centre of the structure does not evidence arms. Colour coded is the normalised histogram of the number of pixels associated to a particular orientation (blue low count, red large count). Several images at different radii give the radial evolution of the general orientation of the domains. (a) 3D histogram shows that near the centre the domains are orientated rather homogeneously over a many angles (from -20° to 60°). (b) Projection over the Radii-Orientation plane, shows that the global orientation of the domains homogenises as the radial distance is increased and, simultaneously, it approaches to zero. With the reference taken in the calculation the Orientation=0 implies a domain radially orientated.

Conclusions and Outlook

Conclusions

In this work, we have investigated the formation of colloidal crystal in two different setups: vertical deposition and spin-coating. Despite the many differences between the two systems, we have shown that in both configurations different structures have associated a different growing velocity. In the case of vertical deposition the structure differ mostly in its density. In the spin-coating experiment they are distinguished by its thickness. Nevertheless, we also found other relevant parameters that play important roles in the formation of the structure.

Vertical deposition

In vertical deposition experiments, we have identified two characteristic velocities associated to different structures. We found that extreme structures of very sparse or close-compact deposits (**NC** and **CM**) are built at a lower rate than structures with intermediate surface density (**NCD**).

We found that structures with more than one layer can be built at low or high rate. We did not have direct access to the detailed structure of these **ML**, but this difference could be a result of different compactness of the 3D **ML** structures.

We also found that an increase of the concentration of the suspension favoured the formation of columnar arrangements of **ML** that can extend for several millimetres in the deposits. We found that, once these columns start to form, a feedback mechanism is established and the columns grow at the expenses of the particles in the surrounding areas.

We evaluated that the effect of the electric fields was restricted to: an electrophoretic attraction of the particles to the positive electrode; and an increase in the interaction between the electrode and the particles. The electrophoretic force drags particles towards the positive substrate locally increasing the effective concentration of the suspension. We determined that, the electrophoretic effect, is particularly important at the beginning of the experiment, although it can still be present at later times. The sudden initial increase of concentration has the drawback that the initial condition of the experiment can be largely affected by the increment of particles, thus a precise reproducibility of the experimental conditions is difficult to achieve.

We observed that an increase of the electrostatic contribution gives rise to band-like structures with well defined spacing. These bands disappeared when the electrostatic potential was increased to 0.6 V. We think that this is due to that a proportion of particles adhere to the surface before the flows in the contact line can drag them from the bulk of the suspension to the deposited structure.

Finally, we found that the alternation of structures with different characteristics (**NC**, **CM**, **NCD** or **ML**) are not only related to a stick-slip process of the contact line but, to a combination of growth velocity of a given structure and the availability of particles in the region near the contact line. Structures built at high rates tend to deplete this zone (that we named **PPZ**) thus forcing a transition to a less dense structure that in turn could tends to grow at low velocity. Thus, the concentration in the **PPZ** is allowed to increase. Later on, this gives rise to a larger density structure. We also observed macroscopic flows that could modified the **PPZ** and, consequently, the deposited structure.

In summary, in a simple vertical deposition system the structure deposited at a particular region of the substrate and its evolution depends on the following parameters:

1. type of structure deposited above and on the sides of the considered point,
2. local concentration of particles in the vicinity of the contact line (**PPZ**),
3. intensity of the particle-substrate interaction.

Spin-coating

Opposite to the vertical deposition system, in the spin coating experiment a large forcing is applied to the suspension, given the rapid rotation of the substrate. In this system, we found that the dynamics can be considered in two stages:

- The initial state is a purely fluid stage. Here the system is comparable to Ackerson's [14, 17, 85] and Jiang's [40] experiments.
- The final structure is formed during the final drying of the suspension. It is directed by the drying front that moves radially inwards. There are no previous studies on the crystallisation dynamics for this kind of systems.

We determined that the thinning dynamics of the fluid stage is perfectly reproduced by a simple volatile fluid model. The adjustment of the model to the experimental data gives a set of parameters that are in good agreement with the properties of the fluid.

We developed a new approach to incorporate the evaporation rate into Emslie's model for simple viscous fluids. We consider that this approach improves the previous model by Meyerhofer [10], where the evaporation rate is incorporated *ad hoc*. Our model does not allow to obtain a simple exact expression for the thinning rate as a function of the absolute thickness. However, it provides a simple exact expression for the thinning rate as a function of time. This an improvement since, in typical experiments, the direct measure is the thinning rate as a function of time. Typically, assumptions are necessary to estimate the absolute thickness [82, 83]. However, our approach eliminates this requirement, thus, comparison between model and experiment can be carried out to higher precision.

We found a collapse of the dimensionless thinning rates as a function of the dimensionless time. Considering the model developed, this collapse indicates that the kinematic viscosity and evaporation rate are proportional to the rotation rate.

In addition to the expected 6-fold symmetry of a sheared suspension, we observed a transition to a 4-fold symmetry. This transition is well correlated with the transition from a dynamics

dominated by radial flows to one dominated by evaporation flows. This is in agreement with the fact that the transition occurs initially in the centre of the substrate (where the strength of the radial flows is smaller).

This can be understood by considering that the crystallisation in a fcc crystal is driven by the shear stress applied to the suspension. From the observations of Ackerson *et al.* [14, 17, 85] and Shereda *et al.* [84] we expect that, when the shear stress is applied by the substrate, the structure shows 6 bright arms (fcc structure with (111) plane parallel to the substrate). This symmetry is observed in the first part of the fluid stage. We conclude that the transition to a 4-fold structure (fcc structure with (100) plane parallel to the substrate) is controlled by the transition to a dynamics dominated by evaporation. This transition implies that there is a change in the main direction of the flows from radially outwards (dominated by non-evaporative effects) to vertical flows (dominated by evaporation effects). Hence, we can summarise this observation as follows:

- flows parallel to the directing plane → 6-arms are observed in a plane parallel to the directing plane
- flows perpendicular to the directing plane → 4-arms are observed in a plane parallel to the directing plane

In the dried structure, we observed a transition between the morphology of the arms in the central and the outer region. At low rotation rates ($\omega \approx 2000$ rpm) the arms appeared well defined on most of the substrate. As ω increased, a region of well defined arms is restricted in the centre of the substrate, while in the outer area the arms are wide and diffuse. Further increase of the rotation rate induces a transition in the outer region of the substrate where a 6-fold symmetry appears (in all previous cases the symmetry was 4-fold). A 4-fold symmetry is still observable in a small region near the centre of rotation. Estimations of the capillary number, from the asymptotic behaviour of the drying front, show that the transition, from a broad diffuse arms to a bright well defined one, is related to the dynamic transition from a situation where viscous forces dominate to one where capillary forces are more important ($Ca=10^{-3}$ and $Ca=10^{-4}$, respectively).

As the rotation rate is increased, the outer region structure suffers a transition form a 4- to a 6-fold symmetry. This could be due to an increase in the effect of the evaporation, induced by a decrease in the thickness and an increase of the rotation rate. However, dV/dt estimations are not enough to discriminate between a stage dominated by capillary flows to one dominated by evaporative flows.

Outlook

It is clear that the dynamics in our vertical deposition experiments is complex and many parameters are involved in the determination of a particular structure. Thus, it is necessary to continue the research to reach a complete understanding of the system. Future experiments should concentrate in control the experimental conditions in order to minimise the number of effects influencing the formation process.

DC electric fields proved to have a measurable effect on the vertical deposition process, but their effect in the initial stages of the experiment makes the conditions to vary considerably from

experiment to experiment. It would be interesting to design experiments where the dynamics is affected by other type of electrokinetic phenomena with a more spatially localised nature.

Quantitative measures of the porosity of **ML** are necessary to be established in order to appropriately compare the different observed dynamics. This could be done by using laser confocal microscopy in structures build with fluorescent particles. The characterisation of the flows in the neighbourhood of the contact line would be a first step towards its control. The control of this flow would allow to control the deposited structure by means of the **PPZ**.

A separately study of the flows induced by each structure would be interesting since it will allow to compare experimental results with recently published simulations results [111].

In spin-coating experiments we were able to advance greatly respect to the previous state of the art. Nevertheless, although the developed model reproduces with a great accuracy the thinning dynamics, it fails when we attempt to extract the absolute thickness. Our observation indicates that the system does not behave as predicted by Emslie or Meyerhofer models, where the fluid should tend to planarise. This could be explained by considering a non-Newtonian model [73], although the derivation becomes much more complex. Additionally, the characterisation of the non-Newtonian behaviour is not a standard procedure since the suspension evaporates rapidly and can modify its properties during the characterisation of its rheology.

Although we give possible mechanisms for the selection of the different symmetries, they should be further confirmed. The change in the stress profile when the dynamics changes from a non-evaporative to an evaporative dominated system could reveal the underlying mechanisms.

Similarly, the question of why the final structure selects one symmetry over other, require more research. The estimated parameters need to be determined more precisely.

It would be interesting to investigate the changes in the dynamic as a function of the vapour pressure. As we already mentioned we expect that the non evaporative regime will extend to later times.

Finally, despite these films are highly reproducible, it would be interesting to develop an experimental technique in which the pouring stage is controlled. We encounter situations where a fast pouring of suspension produce inhomogeneous deposits, probably due to the generation of a skin at the initial stages of the experiment.

Bibliography

- [1] S. Kinoshita, S. Yoshioka, J. Miyazaki. *Physics of structural colors.* Rep. Prog. Phys. **71** (7), (2008), p. 076401.
- [2] G. A. Ozin, S. M. Yang. *The Race for the Photonic Chip: Colloidal Crystal Assembly in Silicon Wafers.* Adv. Funct. Mater. **11** (2), (2001), pp. 95–104.
- [3] R. Williams, R. Crandall. *The structure of crystallized suspensions of polystyrene spheres.* Phys. Lett. A **48** (3), (1974), pp. 225–226.
- [4] L. Rayleigh. *On the Remarkable Phenomenon of Crystalline Reflection described by Prof. Stokes.* Phil. Mag. **26** (160), (1888), pp. 256–265.
- [5] E. Yablonovitch. *Inhibited spontaneous emission in solid-state physics and electronics.* Phys. Rev. Lett. **58** (20), (1987), pp. 2059–2062.
- [6] I. Langmuir. *The mechanism of the surface phenomena of flotation.* Trans. Faraday Soc. **15** (1), (1919), pp. 62–74.
- [7] K. Blodgett. *Films built by depositing successive monomolecular layers on a solid surface.* J. Am. Chem. Soc. **57** (6), (1935), pp. 1007–1022.
- [8] E. Adachi, A. Dimitrov, K. Nagayama. *Stripe patterns formed on a glass surface during droplet evaporation.* Langmuir **11** (4), (1995), pp. 1057–1060.
- [9] A. Emslie, F. Bonner, L. Peck. *Flow of a viscous liquid on a rotating disk.* J. Appl. Phys. **29**, (1958), p. 858.
- [10] D. Meyerhofer. *Characteristics of resist films produced by spinning.* J. Appl. Phys. **49** (7), (1978), pp. 3993–3997.
- [11] B. J. Alder, T. E. Wainwright. *Phase Transition for a Hard Sphere System.* J. Chem. Phys. **27** (5), (1957), p. 1208.
- [12] B. J. Alder, T. E. Wainwright. *Phase transition in elastic disks.* Phys. Rev. **127** (2), (1962), pp. 359–361.
- [13] P. Pieranski. *Two-dimensional interfacial colloidal crystals.* Phys. Rev. Lett. **45** (7), (1980), pp. 569–572.
- [14] B. Ackerson, N. Clark. *Shear-induced melting.* Phys. Rev. Lett. **46** (2), (1981), pp. 123–126.

- [15] P. N. Pusey, W. Van Megen, P. Bartlett, B. J. Ackerson, J. G. Rarity, S. M. Underwood. *Structure of crystals of hard colloidal spheres.* Physical review letters **63** (25), (1989), pp. 2753–2756.
- [16] S. Ashdown, I. Markovic, R. H. Ottewill, P. Lindner, R. C. Oberthur, A. R. Rennie. *Small-Angle Neutron-Scattering Studies on Ordered Polymer Colloid Dispersions.* Langmuir **6**, (1990), pp. 303–307.
- [17] B. Ackerson. *Shear induced order of hard sphere suspensions.* J. Phys.: Condens. Matter **2** (July), (1990), pp. 389–392.
- [18] M. Schmidt, H. Löwen. *Freezing between two and three dimensions.* Phys. Rev. Lett. **76** (24), (1996), pp. 4552–4555.
- [19] C. Dux, H. Versmold. *Light diffraction from shear ordered colloidal dispersions.* Phys. Rev. Lett. **78** (9), (1997), pp. 1811–1814.
- [20] A. Yethiraj, A. Van Blaaderen. *A colloidal model system with an interaction tunable from hard sphere to soft and dipolar.* Nature **421** (6922), (2003), pp. 513–517.
- [21] W. Vos, M. Megens, C. van Kats, P. Böseckes. *X-ray diffraction of photonic colloidal single crystals.* Langmuir **13** (23), (1997), pp. 6004–6008.
- [22] S. H. Park, Y. Xia. *Assembly of Mesoscale particles over large areas and its application in fabricating tunable optical filters.* Langmuir **15** (1), (1999), pp. 266–276.
- [23] D. J. Norris, E. Arlinghaus, L. Meng, R. Heiny, L. Scriven. *Opaline photonic crystals: How does self-assembly work?* Adv. Mater. **16** (16), (2004), pp. 1393–1399.
- [24] P. Braun, S. Rinne, F. Garcia-Santamaria. *Introducing defects in 3D photonic crystals: State of the art.* Adv. Mater. pp. 1–14.
- [25] F. Meseguer. *Colloidal crystals as photonic crystals.* Colloids and Surfaces A: Physicochem. Eng. Aspects **270-271**, (2005), pp. 1–7.
- [26] P. Jiang, J. Bertone, K. Hwang, V. Colvin. *Single-crystal colloidal multilayers of controlled thickness.* Chem. Mater. **11** (8), (1999), pp. 2132–2140.
- [27] O. Vickreva, O. Kalinina, E. Kumacheva. *Colloid crystal growth under oscillatory shear.* Adv. Mater. **12** (2), (1999), pp. 110–112.
- [28] R. Hayward, D. Saville, I. Aksay. *Electrophoretic assembly of colloidal crystals with optically tunable micropatterns.* Nature **404**, (2000), pp. 56–59.
- [29] R. M. Amos, J. G. Rarity, P. R. Tapster, T. J. Shepherd, S. C. Kitson. *Fabrication of large-area face-centered-cubic hard-sphere colloidal crystals by shear alignment.* Phys. Rev. E **61** (3), (2000), pp. 2929–2935.
- [30] S. Melle, O. Calderón, M. Rubio, G. Fuller. *Rotational dynamics in dipolar colloidal suspensions: video microscopy experiments and simulations results.* J. Non-Newtonian Fluid Mech. **102** (2), (2002), pp. 135–148.

- [31] W. D. Ristenpart, I. A. Aksay, D. A. Saville. *Assembly of colloidal aggregates by electrohydrodynamic flow: Kinetic experiments and scaling analysis.* Phys. Rev. E **69** (2), (2004), p. 21405.
- [32] V. de Villeneuve, R. Dullens, D. Aarts, E. Groeneveld, J. Scherff, W. Kegel, H. Lekkerkerker. *Colloidal hard-sphere crystal growth frustrated by large spherical impurities.* Science **309** (5738), (2005), p. 1231.
- [33] A. Mihi, M. Ocaña, H. Miguez. *Oriented Colloidal-Crystal Thin Films by Spin-Coating Microspheres Dispersed in Volatile Media.* Adv. Mater. **18** (17), (2006), pp. 2244–2249.
- [34] M. Ishii, M. Harada, H. Nakamura. *In situ observations of the self-assembling process of colloidal crystalline arrays.* Soft Matter **3** (7), (2007), pp. 872–876.
- [35] C. Arcos, K. Kumar, W. González-Viñas, R. Sirera, K. M. Poduska, A. Yethiraj. *Orientationally correlated colloidal polycrystals without long-range positional order.* Phys. Rev. E **77** (5), (2008), p. 050402R.
- [36] M. Yoldi, C. Arcos, B.-R. Paulke, R. Sirera, W. González-Viñas, E. Görnitz. *On the parameters influencing the deposition of polystyrene colloidal crystals.* Materials Science and Engineering C **28** (7), (2008), pp. 1038–1043.
- [37] M. Oettel, S. Dietrich. *Colloidal Interactions at Fluid Interfaces.* Langmuir **24** (4), (2008), pp. 1425–1441.
- [38] N. J. Lorenz, H. J. Schöpe, H. Reiber, T. Palberg, P. Wette, I. Klassen, D. Holland-Moritz, D. Herlach, T. Okubo. *Phase behaviour of deionized binary mixtures of charged colloidal spheres.* J. of Phys.: Condens. Matter **21** (46), (2009), p. 464116.
- [39] Y. Imura, H. Nakazawa, E. Matsushita, C. Morita, T. Kondo, T. Kawai. *Characterization of colloidal crystal film of polystyrene particles at the air-suspension interface.* J Colloid Interface Sci. **336** (2), (2009), pp. 607–611.
- [40] P. Jiang, M. J. McFarland. *Large-scale fabrication of wafer-size colloidal crystals, macroporous polymers and nanocomposites by spin-coating.* J. Am. Chem. Soc. **126** (42), (2004), pp. 13778–13786.
- [41] E. Vermolen. *Manipulation of colloidal crystallization.* Ph.D. thesis, Utrecht University (2008).
- [42] M. Giuliani, W. González-Viñas, K. M. Poduska, A. Yethiraj. *Dynamics of Crystal Structure Formation in Spin-Coated Colloidal Films.* J. Phys. Chem. Lett. pp. 1481–1486.
- [43] R. Lenormand, E. Touboul, C. Zarcone. *Numerical models and experiments on immiscible displacements in porous media.* J. Fluid Mech. **189**, (1988), pp. 165–187.
- [44] A. Dimitrov, K. Nagayama. *Continuous convective assembling of fine particles into two-dimensional arrays on solid surfaces.* Langmuir **12** (5), (1996), pp. 1303–1311.
- [45] R. Shimmin, A. DiMauro, P. Braun. *Slow Vertical Deposition of Colloidal Crystals: A Langmuir-Blodgett Process?* Langmuir **22** (15), (2006), pp. 6507–6513.

- [46] G. Lozano, H. Miguez. *Growth dynamics of self-assembled colloidal crystal thin films*. Langmuir **23** (20), (2007), pp. 9933–9938.
- [47] R. Hunter. *Foundations of Colloid Science*. Oxford University Press (1989).
- [48] A. A. Kornyshev. *Double-layer in ionic liquids: paradigm change?* J Phys. Chem. B **111** (20), (2007), pp. 5545–5557.
- [49] B. J. Kirby, E. F. Hasselbrink. *Zeta potential of microfluidic substrates: 1. Theory, experimental techniques, and effects on separations*. Electrophoresis **25** (2), (2004), pp. 187–202.
- [50] W. B. Russel, D. A. Saville, W. R. Schowalter. *Colloidal Dispersions*. Cambridge University Press (1989).
- [51] T. Hao. *Electrorheological fluids: The non-aqueous suspensions*. Elsevier Science Ltd (2005).
- [52] J. Crocker, D. Grier. *Microscopic measurement of the pair interaction potential of charge-stabilized colloid*. Phys. Rev. Lett. **73** (2), (1994), pp. 352–355.
- [53] S. Guelcher. *Aggregation of pairs of particles on electrodes during electrophoretic deposition*. Powder Technology **110** (1-2), (2000), pp. 90–97.
- [54] J. Lyklema. *Fundamentals of interface and colloid science, Volume II: Solid-liquid interfaces*. Academic Press (2001).
- [55] T. Jones. *Electromechanics of particles*. Cambridge University Press (1995).
- [56] J. L. Anderson. *Colloid Transport by Interfacial Forces*. Annu. Rev. Fluid Mech. **21** (1), (1989), pp. 61–99.
- [57] H. Verheijen, M. Prins. *Reversible electrowetting and trapping of charge: model and experiments*. Langmuir **15** (20), (1999), pp. 6616–6620.
- [58] B. R. Horrocks, R. D. Armstrong. *Discreteness of Charge Effects on the Double Layer Structure at the Metal/Solid Electrolyte Interface*. J. Phys. Chem. B **103** (51), (1999), pp. 11332–11338.
- [59] V. Martelozzo, a. Schofield, W. Poon, P. Pusey. *Structural aging of crystals of hard-sphere colloids*. Phys. Rev. E **66** (2), (2002), pp. 1–14.
- [60] A. Yethiraj, J. H. J. Thijssen, A. Wouterse, A. van Blaaderen. *Large-Area Electric-Field-Induced Colloidal Single Crystals for Photonic Applications*. Adv. Mater. **(7)**, (2004), pp. 596–600.
- [61] O. Velev, K. Bhatt. *On-chip micromanipulation and assembly of colloidal particles by electric fields*. Soft Matter **2** (9), (2006), pp. 738–750.
- [62] A. Yethiraj. *Tunable colloids: control of colloidal phase transitions with tunable interactions*. Soft Matter **3** (9), (2007), p. 1099.
- [63] K.-Q. Zhang, X. Y. Liu. *Controlled formation of colloidal structures by an alternating electric field and its mechanisms*. J. Chem. Phys. **130** (18), (2009), p. 184901.

- [64] Y. A. Vlasov, X. Z. Bo, J. C. Sturm, D. J. Norris. *On-chip natural assembly of silicon photonic bandgap crystals.* Nature **414** (6861), (2001), pp. 289–293.
- [65] L. M. Goldenberg, J. Stumpe, B.-R. Paulke, E. Go. *Ordered Arrays of Large Latex Particles Organized by Vertical Deposition.* Langmuir **18** (5), (2002), pp. 3319–3323.
- [66] Z. Zhou, X. S. Zhao. *Flow-Controlled Vertical Deposition Method for the Fabrication of Photonic Crystals.* Langmuir **20** (18), (2004), pp. 1524–1526.
- [67] S. Kuai, X. Hu, A. Hache, V. Truong. *High-quality colloidal photonic crystals obtained by optimizing growth parameters in a vertical deposition technique.* J. Cryst. Growth **267**, (2004), pp. 317–324.
- [68] R. Deegan, O. Bakajin, T. Dupont, G. Huber, S. Nagel, T. Witten. *Capillary flow as the cause of ring stains from dried liquid drops.* Nature **389** (6653), (1997), pp. 827–828.
- [69] C. Fustin, G. Glasser, H. Spiess, U. Jonas. *Parameters influencing the templated growth of colloidal crystals on chemically patterned surfaces.* Langmuir **20** (21), (2004), pp. 9114–9123.
- [70] M. Giuliani, W. González-Viñas. *Contact-line speed and morphology in vertical deposition of diluted colloids.* Phys. Rev. E **79** (3), (2009), p. 032401.
- [71] P. Kralchevsky, K. Nagayama. *Particles at fluid interfaces and membranes*, vol. 10. Elsevier Science (2001).
- [72] P. G. de Gennes. *Wetting: statics and dynamics.* Rev. Mod. Phys. **57** (3), (1985), pp. 827–863.
- [73] A. Acrivos, M. Shah, E. Petersen. *On the flow of a non-Newtonian liquid on a rotating disk.* J. Appl. Phys. **31**, (1960), p. 963.
- [74] W. Flack, D. Soong, A. Bell, D. Hess. *A mathematical model for spin coating of polymer resists.* J. Appl. Phys. **56** (4), (1984), p. 1199.
- [75] D. Bornside, C. Macosko, L. Scriven. *Spin coating: one-dimensional model.* J. Appl. Phys. **66** (11), (1989), p. 5185.
- [76] T. Ohara, Y. Matsumoto, H. Ohashi. *The film formation dynamics in spin coating.* Phys. Fluids A **1** (12), (1989), p. 1949.
- [77] T. Rehg, G. Higgins. *Spin coating of colloidal suspensions.* AIChE Journal **38** (4), (1992), pp. 489–501.
- [78] M. Munekata, S. Kimura, H. Kurishima, J. Tanaka, S. Yamamoto, H. Yoshikawa, K. Matsuzaki, H. Ohba. *Effect of catch cup geometry on 3D boundary layer flow over the wafer surface in a spin coating.* J. Therm. Sci. **17** (1), (2008), pp. 56–60.
- [79] J. Koo, J. Lee, C. Jung. *Planarization during spray coating: numerical study.* J. Micromech. Microeng. **18** (3), (2008), p. 035018.

- [80] C. J. Lawrence. *The mechanics of spin coating of polymer films.* Phys. Fluids **31** (10), (1988), p. 2786.
- [81] R. Jackman, T. Floyd, R. Ghodssi, M. Schmidt, K. Jensen. *Microfluidic systems with on-line UV detection.* J. Micromech. Microeng. **11**, (2001), pp. 263–269.
- [82] D. P. Birnie, M. Manley. *Combined flow and evaporation of fluid on a spinning disk.* Phys. Fluids **9** (4), (1997), p. 870.
- [83] S. Y. Heriot, R. a. L. Jones. *An interfacial instability in a transient wetting layer leads to lateral phase separation in thin spin-cast polymer-blend films.* Nature Materials **4** (10), (2005), pp. 782–786.
- [84] L. Shereda, R. Larson, M. Solomon. *Local Stress Control of Spatiotemporal Ordering of Colloidal Crystals in Complex Flows.* Phys. Rev. Lett. **101** (3), (2008), p. 038301.
- [85] B. J. Ackerson, P. N. Pusey. *Shear-induced order in suspensions of hard spheres.* Phys. Rev. Lett. **61** (8), (1988), pp. 1033–1036.
- [86] U. Gasser. *Crystallization in three- and two-dimensional colloidal suspensions.* J. Phys.: Condens. Matter **21** (20), (2009), p. 203101.
- [87] D. Derkx, Y. L. Wu, A. van Blaaderen, A. Imhof. *Dynamics of colloidal crystals in shear flow.* Soft Matter **5** (5), (2009), p. 1060.
- [88] M. Ross. *Generalized Lindemann melting law.* Phys. Rev. **184** (1), (1969), pp. 233–242.
- [89] H. Löwen, T. Palberg, R. Simon. *Dynamical criterion for freezing of colloidal liquids.* Phys. Rev. Lett. **70** (10), (1993), pp. 1557–1560.
- [90] H. Löwen. *Dynamical criterion for two-dimensional freezing.* Phys. Rev. E **53** (1), (1996), pp. 29–32.
- [91] J. J. Gray, R. T. Bonnecaze. *Rheology and dynamics of sheared arrays of colloidal particles.* J. Rheol. **42** (5), (1998), p. 1121.
- [92] C. Arcos. *Preparación y caracterización de materiales mesoestructurados.* Ph.D. thesis, Universidad de Navarra (2008).
- [93] Y. Bertholet. *Measurement, optimization and multiscale modeling of silicon wafer bonding interface fracture resistance.* Ph.D. thesis, Université Catholique de Louvain (2006).
- [94] Y. Han, D. Mayer, A. Offenhausser, S. Ingebrandt. *Surface activation of thin silicon oxides by wet cleaning and silanization.* Thin Solid Films **510** (1-2), (2006), pp. 175–180.
- [95] A. Papra, N. Gadegaard, N. B. Larsen. *Characterization of Ultrathin Poly(ethylene glycol) Monolayers on Silicon Substrates.* Langmuir **17** (5), (2001), pp. 1457–1460.
- [96] K. Kumar. *Preparation and characterization of spin-coated colloidal templates and patterned electrodeposited cobalt.* MSc. thesis, Memorial University of Newfoundland (2008).

- [97] P. Atkins, J. De Paula. *Atkins Physical Chemistry*. Oxford University Press, 8th edn. (2006).
- [98] L. Meng, H. Wei, A. Nagel, B. J. Wiley, L. E. Scriven, D. J. Norris. *The role of thickness transitions in convective assembly*. *Nano Lett.* **6** (10), (2006), pp. 2249–2253.
- [99] M. Ghosh, F. Fan, K. J. Stebe. *Spontaneous pattern formation by dip coating of colloidal suspensions on homogeneous surfaces*. *Langmuir* **23** (4), (2007), pp. 2180–2183.
- [100] G. Broughton, C. S. Windebank. *Agglomeration and Viscosity in Dilute Suspensions*. *Ind. Eng. Chem.* **30** (4), (1938), pp. 407–409.
- [101] E. Raphaël, P. G. de Gennes. *Dynamics of wetting with nonideal surfaces. The single defect problem*. *J. Chem. Phys.* **90**.
- [102] Rosemount Digital Air Data Systems (DADS). Aircraft Engineering and Aerospace Technology **58** (12), (1986), pp. 16–17.
- [103] Y. Solomentsev, M. Bohmer, J. Anderson. *Particle clustering and pattern formation during electrophoretic deposition: A hydrodynamic model*. *Langmuir* **13** (23), (1997), pp. 6058–6068.
- [104] K. Kang. *How electrostatic fields change contact angle in electrowetting*. *Langmuir* **18** (26), (2002), pp. 10318–10322.
- [105] W. Chen. *An improved tension-plate system for measuring first-stage evaporation under straw mulch*. *Agric. For. Meteorol.* **85** (1-2), (1997), pp. 1–17.
- [106] P. Pusey, W. Van Megen. *Phase behavior of concentrated suspensions of nearly hard colloidal spheres*. *Nature* **320** (6060), (1986), pp. 340–342.
- [107] B. J. Ackerson. *Shear induced order in equilibrium colloidal liquids*. *Physica A* **174**, (1991), pp. 15–30.
- [108] I. Cohen, T. Mason, D. Weitz. *Shear-Induced Configurations of Confined Colloidal Suspensions*. *Phys. Rev. Lett.* **93** (4), (2004), p. 046001.
- [109] Y. L. Wu, D. Derkx, A. van Blaaderen, A. Imhof. *Melting and crystallization of colloidal hard-sphere suspensions under shear*. *PNAS* **106** (26), (2009), pp. 10564–10569.
- [110] P. Kolodner, H. Williams. *Complex demodulation techniques for experiments on travelling-wave convection*. Nonlinear evolution of Spatio-Temporal Structures in Dissipative Continuous Systems pp. 73–91.
- [111] D. D. Brewer, J. Allen, M. R. Miller, J. M. Santos, S. Kumar, D. J. Norris, M. Tsapatsis, L. E. Scriven. *Mechanistic principles of colloidal crystal growth by evaporation-induced convective steering*. *Langmuir* **24** (23), (2008), pp. 13683–13693.

Summary

In this experimental work, we present a study on the dynamics of the crystallisation of colloidal suspension. We studied two experimental setups: vertical deposition configuration and spin-coating. The vertical deposition setup permits to apply electric fields in a configuration similar to a parallel plate capacitor. We used polystyrene particles ($1.3\text{ }\mu\text{m}$ in diameter) suspended in ultrapure water at low volume fractions (0.1% to 0.5%). The experiments were carried out at controlled temperature $63\text{ }^{\circ}\text{C}$ and low humidity (below 2 %RH). We also applied weak electric fields (0.2 to 0.6 V/mm) to study their effect on the dynamics. We measured the velocity of growth of different structures at the different experimental conditions. We observed that, at low concentration 0.1%, there is only one characteristic velocity that we associate with two extreme structures, a very sparse deposit and a compact monolayer. For the higher concentration studied (0.3 % and 0.5 %) we found that a new characteristic velocity of larger magnitude appears. This velocity is associated with a sub-monolayer structure forming bands a few particles wide. We observed multilayer structures that can grow at high or low velocity. In the presence of electric fields, the characteristic velocities are little modified, although we identified interesting structuring of some deposits in parallel lines of highly periodic spacing. We concluded that the complex dynamics associated to this system is due to the different parameters that affect the deposition process: type of structure deposited above the contact line, local concentration near the contact line and intensity of the interaction between the particle and the substrate.

In the spin-coating setup, we used 458 nm diameter spheres dispersed on acetone or methyl ethyl ketone. The high volatility of the fluids and the thin layer induced by the rotation of the substrate gave a rapid dynamics (< 2 s). The concentration of the suspension mainly was 20 %. Some experiments at lower concentration were performed, but it was observed that static results were equivalent to increase the rotation rate of the substrate. The dynamics was recorded with a high speed camera. We characterised the thinning rate and the long range orientational order dynamics during the fluid stage, as well as the drying front dynamics. We also characterised the radial thickness profiles of the dried deposits and their symmetry. We extended the model of Emslie [9] to volatile fluids and found that gives an excellent fit to the experimental data of the thinning rate as a function of time. We also observed a transition from a 6- to a 4-fold symmetry in the fluid stage that correlates well with the transition from the non-evaporative to the evaporative stage extracted from the fit. We observe a transition in the morphology of the bright arms of the dried deposit. Near the centre they are generally well defined, while as the speed is increased, their definition decrease in the outer region. This transition correlates well with an increase in the relevance of capillary forces with respect to the viscous forces at the time of crystallisation. We conclude that the balance between radial and evaporative flows are responsible of the different observed symmetries.

Resumen

En este trabajo experimental presentamos un estudio de la dinámica durante la cristalización de suspensiones coloidales. Hemos estudiado dos sistemas distintos: deposición vertical y spin-coating. La configuración usada en deposición vertical reproduce un condensador de placas paralelas. Hemos usado partículas de poliestireno ($1,3\text{ }\mu\text{m}$ de diámetro) suspendidas en agua ultrapura a baja concentración (0,1 % a 0,5 % v/v). Los experimentos fueron realizados a temperatura controlada $63\text{ }^{\circ}\text{C}$ y baja humedad (<2 %RH). Se han aplicado campos eléctricos débiles (0,2 a 0,6 V/mm) para evaluar su efecto en la dinámica asociada. Hemos observado que, a bajas concentraciones (0,1 %) hay sólo una velocidad característica asociada a dos estructuras límites: un depósito muy disperso de partículas inconexas y un depósito de monocapa compacta. El aumento de la concentración (a 0,3 %, o 0,5 %) es acompañado con la aparición de una nueva velocidad de mayor magnitud que la anterior. Asociamos esta velocidad a una estructura intermedia a las anteriores. Esta nueva estructura se caracteriza por bandas de una pocas partículas de ancho. Se observaron estructuras con más de una capa construidas a velocidades bajas y altas. Los campos eléctricos modifican ligeramente la velocidad característica medida. Se observó una estructura particular en presencia de los campos eléctricos caracterizada por cadenas de partículas separadas por una distancia con un período bien definido. Concluimos que la dinámica compleja que se observa en este sistema es resultado de la interrelación de tres parámetros: tipo de estructura depositada por encima de la línea de contacto, concentración local de partículas en las cercanías de la línea de contacto, e intensidad de la interacción entre el substrato y las partículas.

En los experimentos realizados con spin-coating, hemos utilizado partículas esféricas de 458 nm diámetro dispersas en acetona o metiletilcetona. La alta volatilidad de los fluidos utilizados y la fina capa de suspensión inducida por la rotación del substrato, resultan en una dinámica rápida (<2 s). La concentración principal de la suspensión fué de 20 % v/v. Se realizaron experimentos con concentraciones inferiores pero el resultado de la estructura final era equivalente a incrementar la velocidad de rotación del substrato. La dinámica fué capturada con una cámara digital de alta velocidad. Con estas medidas caracterizamos la velocidad a la cual el espesor decrece y el orden orientacional a grandes distancias en la etapa fluída. También caracterizamos la velocidad del frente de secado. En la estructura seca, hemos caracterizado los perfiles de espesor en función de la coordenada radial y su simetría. Extendimos el modelo desarrollado en 1958 por Emslie [9] para fluidos volátiles. Encontramos que esta extensión está en excelente acuerdo con las medidas experimentales. Hemos identificado una transición de 4 a 6 brazos en etapa fluida. Asimismo, esta transición corresponde aproximadamente con la transición de una dinámica dominada por la rotación del substrato a una dominada por la evaporación. También, observamos, una transición en la calidad de los brazos entre la parte central del substrato y la parte exterior. Hemos relacionado esta transición a un aumento en la intensidad de las fuerzas capilares respecto de las viscosas. Finalmente, hemos concluido que las transiciones entre las diferentes simetrías se deben a un cambio en la dirección de los flujos como consecuencia de una dinámica de origen evaporativo o centrífugo.

